Dissertations, Master's Theses and Master's Reports

2016

INCREASING SOLAR ENERGY CONVERSION EFFICIENCY IN HYDROGENATED AMORPHOUS SILICON PHOTOVOLTAIC DEVICES WITH PLASMONIC PERFECT META – ABSORBERS

Jephias Gwamuri
Michigan Technological University, jgwamuri@mtu.edu

INCREASING SOLAR ENERGY CONVERSION EFFICIENCY IN
HYDROGENATED AMORPHOUS SILICON PHOTOVOLTAIC DEVICES WITH
PLASMONIC PERFECT META – ABSORBERS

By

Jephias Gwamuri

A DISSERTATION

Submitted in partial fulfillment of the requirements for the degree of

DOCTOR OF PHILOSOPHY

In Materials Science and Engineering

MICHIGAN TECHNOLOGICAL UNIVERSITY

2016

This dissertation has been approved in partial fulfillment of the requirements for the Degree of DOCTOR OF PHILOSOPHY in Materials Science and Engineering.

Department of Materials Science and Engineering

Dissertation Advisor: *Dr. Joshua A. Pearce*

Committee Member: *Dr. Miguel Levy*

Committee Member: *Dr. Durdu Guney*

Committee Member: *Dr. Paul Bergstrom*

Department Chair: *Dr. Stephen L. Kampe*

Table of Contents

List of Figures

List of Tables

Preface

This dissertation is composed of one published book chapter, three published and two submitted papers. The author's contributions are described hereafter.

Chapter two is published as chapter 10 in the book *Solar Cell Nanotechnology* [J. Gwamuri, D.Ö. Güney, J.M. Pearce: Advances in plasmonic light trapping in thin-film solar photovoltaic devices. In: Tiwari, A., Boukherroub, R., Sharon, M. (eds.) Solar cell nanotechnology, Wiley, Hoboken, pp. 243–270, Sept. 2013]. J. Gwamuri reviewed all the necessary literature, as well as working on analysis, figures and writing of the chapter. D. Guney contributed immensely on advising on plasmonics and metamaterials and editing. J. Pearce contributed on writing, editing and consultation.

Chapter three is published in the journal *Materials for Renewable and Sustainable Energy* [J. Gwamuri, A. Vora, R. R. Khanal, A. B. Phillips,M. J. Heben, D. O. Guney, P. Bergstrom, A. Kulkarni, and J. M. Pearce, "Limitations of ultra-thin transparent conducting oxides for integration into plasmonic-enhanced thin-film solar photovoltaic devices," *Mater. Renew. Sustain. Energy*, vol. 4, no. 3, pp. 1–11, Jul. 2015]. J. Gwamuri was responsible for the literature review, experimental design, fabrication, experimental data collection, results analysis, figures, tables and writing the paper. A. Vora and D. Guney contributed on the experimental design, simulation and editing. R. R. Khanal, A. B. Phillips and M. J. Heben contributed on fabrication, experimental data and editing. P. Bergstrom and A. Kulkarni contributed on experimental design and editing, whilst J. M. Pearce contributed on writing, experimental design, editing and consultation.

Chapter four is published in the journal *Solar energy Materials and Solar Cells* [J. Gwamuri, A. Vora, J. Mayandi, D. Ö. Güney, P. L. Bergstrom, J. M. Pearce, "A new method of preparing highly conductive ultra-thin indium tin oxide for plasmonic-enhanced thin film solar photovoltaic devices", *Solar Energy Materials and Solar Cells*, vol 149, pp. 250-257, Jan. 2016] The paper was written by J. Gwamuri and the following co-authored; A. Vora, J. Mayandi, D. Guney, P. Bergstrom and J. Pearce. J. Gwamuri's contribution in this paper were literature review, experimental design, fabrication, experimental data collection, results analysis, figures, tables and writing the paper. A. Vora and D. Guney contributed on device modelling, theory and editing. P. Bergstrom contributed on experimental design and editing. J. Mayandi's contribution was on experimental

design (etching process), data and editing whilst J. M. Pearce contributed on writing, experimental design, editing and consultation.

Chapter five is published in the journal *Materials* [J. Gwamuri, M. Marikkannan, J. Mayandi, P. K. Bowen, J. M. Pearce, "Influence of Oxygen Concentration on the Performance of Ultra-Thin RF Magnetron Sputter Deposited Indium Tin Oxide Films as a Top Electrode for Photovoltaic Devices" *Materials*, vol 9, no. 1 pp. 63, Jan 2016]. J. Gwamuri's contribution in this paper were literature review, experimental design, fabrication, experimental data collection, results analysis, figures, tables and writing the paper. M. Marikkannan and J. Mayandi's contribution was on XRD and Raman data analysis and editing. P. K. Bowen contributed on AFM analysis and editing whilst J. M. Pearce contributed on writing, experimental design, editing and consultation.

Chapter six is under review [J Gwamuri, R Venkatesan, J Mayandi, M Sadatdol, D Guney, and J M. Pearce "Ambient-dependent Agglomeration and Surface-Enhanced Raman Spectroscopy Response of Self-Assemble Silver Nano-particles for Plasmonic Photovoltaic Devices"]. J. Gwamuri's contribution in this paper were literature review, experimental design, fabrication, experimental data collection, data analysis, figures, tables and writing the paper. R. Venkatesan and J. Mayandi's contribution was on UV-vis and SERS data and editing. M. Sadatdol and D. Guney contributed on simulation and editing whilst J. M. Pearce contributed on writing, experimental design, editing and consultation.

Chapter seven is under review. [J Gwamuri, M Junda, M Sadatdol, J Mayandi, D Guney, N Podraza and J M. Pearce "Plasmonic enhanced a-Si:H PV using Multi-disperse Self-Assemble Silver Nanoparticles"]. The paper was written by J. Gwamuri's contribution in this paper were literature review, experimental design, fabrication, experimental data collection, data analysis, figures, tables and writing the paper. M. Junda and N. Podraza's contribution was on nip-a-Si:H device fabrication, data collection and editing. J. Mayandi's contribution was on experimental design and editing. M. Sadatdol and D. Guney contributed on device modelling and editing whilst J. M. Pearce contributed on writing, experimental design, editing and consultation.

Acknowledgements

Abstract

Solar photovoltaic (PV) devices are an established, technically-viable and sustainable solution to society's energy needs, however, in order to reach mass deployment at the terawatt scale, further decreases in the levelized cost of electricity from solar are needed. This can be accomplished with thin-film PV technologies by increasing the conversion efficiency using sophisticated light management methods. This ensures absorption of the entire solar spectrum, while reducing semiconductor absorber layer thicknesses, which reduces deposition time, material use, embodied energy and greenhouse gas emissions, and economic costs. Recent advances in optics, particularly in plasmonics and nanophotonics provide new theoretical methods to improve the optical enhancement in thin-film PV. The project involved designing and fabricating a plasmonic perfect meta-absorber integrated with hydrogenated amorphous silicon (a-Si:H) solar PV device to exhibit broadband, polarization-independent absorption and wide angle response simultaneously in the solar spectrum.

First, recent advances in the use of plasmonic nanostructures forming metamaterials to improve absorption of light in thin-film solar PV devices is reviewed. Both theoretical and experimental work on multiple nanoscale geometries of plasmonic absorbers and PV materials shows that metallic nanostructures have a strong interaction with light, which enables unprecedented control over the propagation and the trapping of light in the absorber layer of thin-film PV device. Based on this, the geometry with the best potential for the proposed device is identified and used for device modelling and, finally the plasmonic enhanced n-i-p a-Si:H solar cell with top surface silver (Ag) metallic structure is proposed. In order for the plasmonic enhanced PV device to be commercialized the means of nanoparticle deposition must also be economical and scalable. In addition, the method to fabricate silver nanoparticles (AgNPs) must be at lower temperatures than those used in the fabrication process for a a-Si:H PV device (less than 180 ^{0}C). The results indicate the potential of multi-disperse self-assemble nanoparticles (SANPs) to achieve broadband resonant response for a-Si:H PV devices. Finally a plasmonic enhanced a-Si:H PV using multi-disperse SANPs is realized when AgNPs are integrated to the commercially fabricated *nip*-a-Si:H PV devices. The devices are characterized for both quantum efficiency and light I–V to evaluate the cell parameters (Jsc, Voc, FF and η). Real–time spectroscopic ellipsometry (RTSE) data is used to model the device performance and the theoretical parameters are compared with the experimental data. Conclusions are drawn and recommendations and future work is suggested.

1. Introduction

1.1 Motivation

The objective of this study is to increase the efficiency of hydrogenated amorphous silicon solar cells using plasmonic perfect meta-absorbers. The use of nano-structures on top of p-layer to excite multiple plasmonic resonances is proposed. Changing the nanostructure shape, spacing or geometry will tune the resonances to provide impedance matching at the front surface of the cell resulting in light being preferentially forward scattered into the solar cell and coupled into multiple Fabry-Perot modes. The scattering and re-scattering of photons will result in increased photon lifetimes and hence increases their chance of being absorbed whilst the reduction in active material thickness will increase the probability for the photo-generated charge carries to be collected before recombination occurs. This decrease in the physical dimension of the device active material layers is also expected to decrease the photo-induced degradation also known as the Staebler-Wronski effect (SWE).

1.2 Dissertation Outline

Chapter 2 reviews the recent promising advances in the use of plasmonic nanostructures forming metamaterials to improve absorption of light in thin-film solar photovoltaic (PV) devices. It introduces the concepts of plasmonics and metamaterial before exploring the theoretical approaches to plasmonic light trapping mechanisms in thin-film PV devices. Then it further explores plasmonics for improved PV cells optical properties and the associated fabrication techniques and economics before drawing conclusions to guide the project design process. Chapter 3 discusses the limitations of ultra-thin transparent conducting oxides for integration into plasmonic-enhanced thin-film solar photovoltaic devices, while Chapter 4 describes a new method of preparing highly conductive ultra-thin indium tin oxide for plasmonic-enhanced thin film solar photovoltaic devices. Chapter 5 is focused on the influence of oxygen concentration on the performance of ultra-thin RF magnetron sputter deposited indium tin oxide films as a top electrode for photovoltaic devices and Chapter 6 describes a detailed study on ambient-dependent agglomeration and surface-enhanced Raman spectroscopy response of self-assemble silver nano-particles for plasmonic photovoltaic devices. Then, Chapter 7 provides the experimental evidence of a plasmonic enhanced a-Si:H PV using multi-disperse self-assemble silver nanoparticles. Finally, Chapter 8 discusses the experimental results in a broader perspective and draws recommendations to guide future work.

2. Advances in Plasmonic Light Trapping in Thin-Film Solar Photovoltaic Devices[1]

2.1. Introduction

The growing environmental concerns for the combustion of fossil fuels are driving a renewed interest in developing solar photovoltaic (PV) devices, which convert sunlight directly into electricity. PV is an established, technically-viable and sustainable solution to society's energy needs [1]. However, in order to out-compete highly subsidized fossil fuels to reach mass deployment at the terawatt scale, further decreases in the LCOE from solar are needed [2]. Conventional (1st generation polycrystalline and single crystalline silicon [c-Si]) PV have extremely limited abilities to improve performance and/or reduce costs [3]. Second generation thin-film PV technology does have this ability. Unfortunately, as these thin-film technologies evolve, their costs become progressively dominated by those of the constituent materials such as the top cover sheet and encapsulation [4]. Thus, the most promising approach to further drive down costs for clean solar electricity is to copiously increase the conversion efficiency of thin-film PV [3, 5]. Practically this means that more sunlight must be absorbed by the PV and converted into electricity. Various methods of optical enhancement have been developed such as the two classical methods of (i) scattering from a top roughened anti-reflection coating and (ii) using a detached back reflector [6, 7]. More sophisticated light management in thin-film PV is important to ensure absorption of the entire solar spectrum, while reducing semiconductor absorber layer thicknesses, which reduces deposition time, material use, embodied energy and greenhouse gas emissions, and economic costs. Recent advances in optics, particularly in plasmonics and nanophotonics provide new methods to improve the optical enhancement in thin-film PV. Theoretical work on the use of plasmonic nanostructures on PV devices has indicated that absorption enhancement of up to 100% is possible for thin-film PV devices using nanostructured metamaterials [6, 8]. This chapter reviews the recent promising advances in the use of plasmonic nanostructures to improve absorption of light in thin-film solar PV devices. Metal nanostructures have a strong interaction with light, which enables unprecedented

---

[1] "The material contained in this chapter was previously published in the book *Solar Cell Nanotechnology*".

control over the propagation and the trapping of light in the absorber layer of thin-film PV. Both the theoretical and experimental literature is reviewed on multiple nanoscale geometries of metamaterial absorbers and PV materials. Finally, the future of the use of novel nanostructures to improve light trapping architectures and enhance photocurrent generation in PV devices is outlined.

2.1.1 Plasmonics Basics

Plasmonics represent a rapidly growing field for the application of surface/interface plasmons towards realization of a variety of surface-plasmon-based devices including: biosensors, nano-imaging, waveguides, data storage, PV, light-emitting devices, and others [9, 10]. Plasmonics mainly involve two types of plasmons: 1) Surface Plasmon Polaritons (SPP), and 2) Localized Surface Plasmons (LSP).

In general, surface plasmons (SPs) can be described as the non-propagating collective vibrations of the electron plasma near the metal surface [11, 12]. SPs are collective oscillations of surface electrons whereas SPP describes a coupled state between an SP and a photon. On the other hand, LSP are surface excitations in bounded geometries such as metallic nanoparticles or voids of various topologies [13]. The fluctuations of surface charge results in highly localized and significantly enhanced electromagnetic fields in the vicinity of metallic surfaces. A detailed treatment of theory and fundamentals of plasmonics is given in [11–14]. In PV applications, light impinging on a metal surface produces surface waves along the metal-dielectric interface when they interact with the collective oscillations of free electrons in the metal. These surface waves (SPP), have shown potential for making plasmonic metamaterial "perfect absorbers" to enhance the efficiency of PV devices [15]. Perfect metamaterial absorbers can be designed with broadband, are polarization-independent, and have wide-angle optical absorption [16]. These critical features, lacking in most optical enhancement schemes for solar cell designs, are ideally required to maximize the efficiency of PV. Wide-angle reception, for example, is particularly important to increase solar energy conversion efficiency for maximized temporal and spatial response of the modules to solar radiation. This then eliminates the need for a physical tracking mechanism, which is beneficial as tracking schemes are known to increase both PV system's initial costs and operating costs.

Various configurations used to excite SPPs for different applications are illustrated in Figure 2.1 [13]. The attenuated total reflectance (ATR) configuration is often used for sensing applications. The geometry of the metallic structures can be

manipulated to achieve desired surface plasmon resonances and propagating properties. Typically, surface plasmon resonances exhibit a strong relationship to the size, shape and the dielectric properties of the surrounding medium. The resonances of noble metals are mostly in the visible or infrared region of the electromagnetic spectrum, which is the range of interest for photovoltaic applications [17].
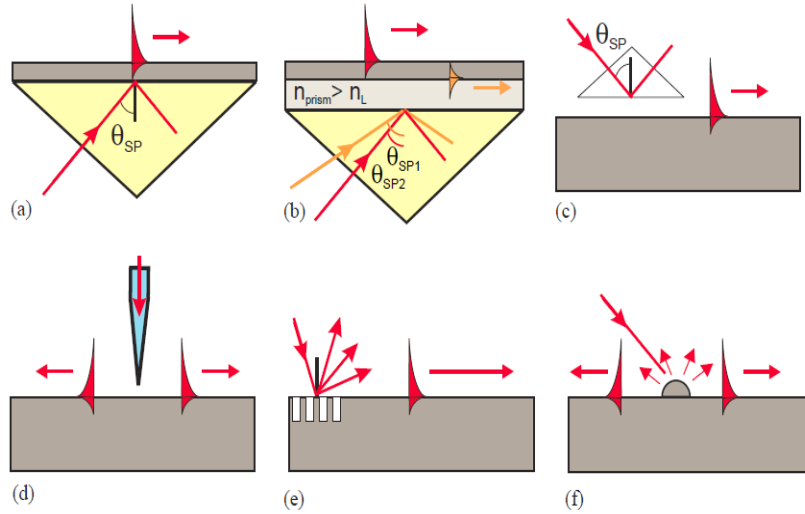
Figure 2. 1. SPP excitation configurations: (a) Kretschmann geometry, (b) two-layer Kretschmann geometry, (c) Otto geometry, (d) excitation with a SNOM probe, (e) diffraction on a grating, and (f) diffraction on surface features. *Figure reproduced with permission A. V. Zayats* [13].

2.1.2 Metamaterials

Metamaterials are rationally designed geometries of artificial optical materials [14, 18], with electromagnetic response in nearly arbitrary frequencies [19]. Usually metamaterials are in the form of periodic structures with sub-wavelength features. The uniqueness of these novel materials is that they exhibit optical properties not observed in their constituent materials, i.e., they derive properties mainly from structure rather than from composition and they have enabled unprecedented flexibility in manipulating light waves and producing new functionalities [20]. Some of the proposed applications for metamaterials include super-lenses that allow sub-wavelength resolution beyond the diffraction limit, and the electromagnetic cloak, which promises the ultimate optical illusion — invisibility [18].

Ultrathin metamaterial nanostructures exhibiting broadband and wide-angle resonant absorption have been proposed for PV devices and demonstrated both theoretically and practically, through device simulations and fabrication [17, 19, 21, 22]. Different cell geometries have been investigated in diverse configurations, with the metal-insulator-metal (MIM) being the most common.

Recently, more complex structures have been developed. The main difference between plasmonic metamaterial absorbers and other plasmonic approaches for enhancing solar power conversion efficiency is that the metamaterial approach provides more degrees of freedom in terms of impedance matching to minimize reflection and more flexible management of light in terms of polarization independence and wide angular reception. Therefore, plasmonic metamaterial absorbers can potentially provide better management of light. However, metamaterial absorbers have not been studied systematically in the literature for solar cell applications. The "super absorber" proposed by Aydin *et al.* [21], for example, uses a lossless spacer where almost all the power is absorbed by metal, hence resulting in significant Ohmic loss (i.e. heating). Nevertheless, there is potential to transfer this energy lost in the metal to the semiconductor if a semiconductor spacer replaces the dielectric spacer in the perfect (or super) absorbers, which can then be used in thin-film PV.

2.2. Theoretical Approaches to Plasmonic Light Trapping Mechanisms in Thin-film PV

The ability of metallic nanostructures to sustain coherent electron oscillations SPPs and LSPs leading to electromagnetic fields confinement and enhancement has attracted substantial attention in the PV scientific community [18, 23, 24]. Plasmonic solar cells have been investigated around the following main configurations: i) metal nanoparticles, ii) nanowires, and iii) metallic nanostructures (MIM/IMI), which can also be regarded as simple metamaterial absorbers.

Designs have been proposed for two-dimensional, ultra-thin, wide-angle perfect absorber structures for infrared light with a theoretical limit of nearly 100% absorption at the tunable resonant wavelength [24]. In 2011, another group reported an average measured absorption of 0.71 over the entire visible spectrum (400–700 nm) from their ultrathin (260 nm), broadband and polarization independent plasmonic super absorber consisting of a MIM stack [21]. They further demonstrated through simulation that absorption levels in the order of

0.85 are possible. By using suitably engineered metal nanostructures integrated in thin-film PV designs, effective light trapping mechanisms and geometries can be achieved. Plasmonic light-trapping geometries for thin-film PV such as those proposed by Atwater and Polman [6] have the potential of enhanced light absorption throughout the entire AM 1.5 solar spectrum. Using these same geometries proposed in [6], researchers experimentally demonstrated superior cell efficiencies of ultra-thin n-i-p hydrogenated amorphous silicon (a-Si:H) solar cells with plasmonic back reflectors compared to randomly textured cells [26]. These absorber layer thickness savings are particularly important for a-Si:H-based PV as this would reduce the light-induced degradation as well as save on manufacturing costs [27]. Recently, another research group designed and fabricated ultra-thin (100 nm) film silicon on insulator (SOI) Schottky photo-detectors for photocurrent enhancement in the spectral range 600–950 nm and achieved a spectral integrated 31% enhancement [28].

The advances recorded so far in the field of plasmonic PV devices can be attributed to the availability of electromagnetic (EM) field modeling tools such as COMSOL Multiphysics and Lumerical FDTD, which have provided important insights into both device design and optimization [29, 30]. Simulation studies have been the principal guiding tool in the area of plasmonics by providing a holistic picture of the interactions between EM fields and nanostructures at sub-wavelength scale. Simulation information such as the scattering or resonant absorption by nanoparticles behaving like dipoles have not only provided deep insights into the various processes such as the near field and coupling effects, but also served as accurate optimization tools [31, 32].

2.2.1 Optimal Cell Geometry Modeling

Optimization of plasmonic light trapping in a solar cell is a complex balancing act in which several physical parameters must be taken into account. However, the problem is simplified by the use of recently developed tools for nanoscale fabrication and nanophotonics characterization, as well as the emergence of powerful electromagnetic simulation methods [6]. Cell geometry simulations have been based on theoretical parameters from other reported models for optimization by continually changing model parameters [33]. The flexibility in this type of a model usually results in impressive theoretical PV performance parameters being reported, such as a FF > 0.73 and J_{sc} > 15 mA/cm². The other common approach is to use parameters from a physical model, which are experimentally determined

using tools such as variable angle spectroscopic ellipsometry for determining optical properties. An example of such a model device and metal top surface structure are shown in Figure 2.2. In this kind of model, usually the physical parameters such as thickness and dielectric properties of layers are the initial inputs for optimizing plasmonic meta-structures. To ensure consistency between the prepared cell samples and the simulated models, both the layer thicknesses and optical parameters are kept constant as the period, height and width of the nanostructures are varied. The metallic parts (back contact and front nanostructure) are made of silver. Optical constants of silver (Ag), a-Si:H, indium tin oxide (ITO), aluminum-doped zinc oxide (ZnO:Al) and silicon nitride (Si_3N_4) are available [34, 35]. However, if the material specifications of the samples differ from that reported in literature, the parameters of interest can be physically determined using spectroscopic ellipsometry [36].

(a)   (b)
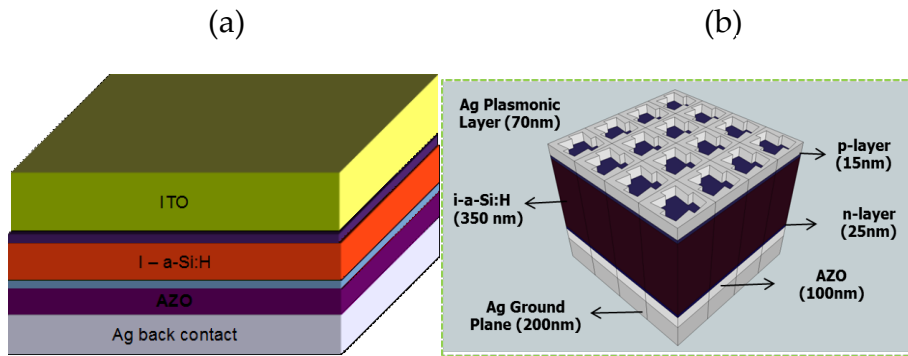
Figure 2.2. Typical schematic device design for (a) the standard single junction of a-Si:H solar cell, (b) the plasmonic enhanced n-i-p a-Si:H solar cell with top surface Ag metallic structure, which takes the place of the standard TCO (ITO or ZnO) contact(*Not to scale*).
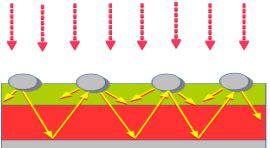
In designing optimal cell geometry for plasmonic PV cells, it is paramount to maximize the absorption within the semiconductor region while minimizing it within the metallic regions over the entire solar spectrum for a wide range of incidence angles. The radius of curvature technique (RCT) [37] can be employed to minimize the metallic losses, so that optical absorption is directed toward the semiconductor layers. This technique requires identification of resonant modes of the metamaterial absorber that contributes to optical absorption, followed by a geometric tailoring of the nanostructure based on underlying resonant currents. It is also necessary to develop and optimize the metamaterial absorbers to satisfy the requirements of wide-angle reception [38] and polarization-independent operation. To achieve this task different nanostructure geometries such as a square-grid structure (i.e., cross structures formed by perpendicularly placed
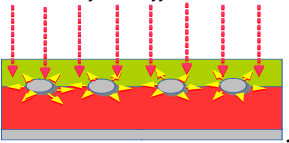
metallic stripes) or any isotropic design found in the literature [25, 33, 39–41] can be used. Broadband response can be achieved by employing the nano-antenna concept [41, 42] or the "super absorber" design demonstrated in Ref. [21]. The model output helps to inform in selecting the nanostructure parameters giving the optimum absorption (see Table 2.1) for the actual integration into experimental cells. At these parameters, the nanostructures start to exhibit both features (i.e., polarization independence and broadband response) within a single design and the potential to operate over the entire visible spectrum (400–700 nm) and wide angular ranges
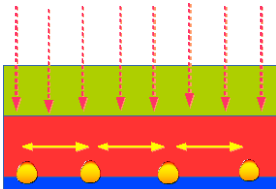
2.2.2 Optical Properties Simulations

The SPP coupling must be stronger in the semiconductor than in the metal for efficient light absorption to occur. Hence metal nanostructure design must be such as to result in increased propagation length in the desired solar-cell geometry. For high efficiency, the PV must be optically thick, but electronically thin having minority carrier diffusion lengths several times the material thickness if all the photogenerated carriers are to be successfully collected [6]. Designing PV cells optimized for enhanced optical absorption is a sophisticated task that often involves a balancing of the physical parameters of the device. For example, small particles can be used to create a very intense forward scattering anisotropy with albedos greater than 90%, however they exhibit equally high Ohmic losses. Balancing between nanostructure size and Ohmic losses is a critical design task. Increasing the effective scattering cross section can be achieved by spacing the nanostructure further away from the active semiconductor substrate at the expense of the near-field coupling, hence another balancing act. EM modeling tools thus play a crucial role in helping researchers find an optimal balance of design parameters by revealing insights into light interactions with different possible modes within the substrate material at subwavelength scale. It is difficult to separate optical properties simulation from cell geometry modeling as device models must maintain broadband, wide angle and polarization-independent absorption. All these properties fundamentally determine the final device's optical characteristics in general, particularly the quantum efficiency (QE).

Table 2.1. Selected Plasmonic Solar Cells Parameters (Adapted from Gu et al, 2012.)

Mechanism	Solar cell type	Plasmonic material and location	Fabrication method	Enhancement (Relative)	Enhancement (Absolute)
Metallic nanoparticles (on top of the solar cell) dipole scattering – *far field nect*. 	a-Si thin-film, substrate-configured (Derkacs et al., 2006)	Au NPs, front	Synthesis + coating	J_{SC}= 8.1 % , η = 8.3 %	J_{SC} from 6.66 to 7.2 mA/cm^2 , η from 2.77 % to 3 %
	multi-Si wafer, commercial(Fahim et al., 2012)	Au NPs, front	Chemical synthesis + dip coating	η = 35.2 %	η - 15.2 % , J_{SC} - 32.3 mA/cm^2 , FF -76 %, V_{oc} – 0.62 V (Best cell results)
	a-Si/c-Si heterojunction (Losurdo et al., 2009)	Au NPs, front	Sputtering on heated substrate	J_{SC} 20 % , η = 25 %	J_{SC} from 19 to 22.9 mA/cm^2 , η from 7.5 % to 9.4 %
	p-n Si:μcSi [Temple et al, 2009]	Ag NPs, front and Al back contact	Deposition (e-beam) + annealing	Highest values for λ *less than 550 nm*	η - 9.06%, V_{oc} = 0.57V, J_{SC} - 21.49 mA/cm^2, FF - 73.84%

	GaAs (Nakayama et al., 2008)	Ag NPs, front	Evaporation through anodic Al template	J_{SC} - 8 % , η - 25 % J_{SC} from 11 to 11.9 mA/cm²	η - from 4.7 % to 5.9 %
	Organic, P3HT:JSCBM [Morfa et al,2008]	Ag NPs, front	Synthesis + spin coating	η from 1.3 % to 2.2 %	J_{SC} - 58 % , η - 69 % J_{SC} from 4.6 to 7.3 mA/cm²
	Organic, P3HT:JSCBM [Lee et al, 2009]	Au NPs, front	Electrostatic assembling	J_{SC} - 36 % , η - 20 %	J_{SC} from 10.74 to 11.13mA/cm² , η from 3.04 % to 3.65 %
Metallic embedded NPs– *near field effect*	InGaN [Wang et al, 2010]	Ag NPs, embedded	(Numerical simulation)	η - 27 % (calculated)	η from 10.59 % to 13.53 % (calculated)
	Organic, CuJsc-PTCBI tandem[26]	Ag clusters, at interface of two sub-cells	Deposition	J_{SC} - 29 % , η - 26 % (calculated)	J_{SC} from 3.65 to 4.72 mA/cm² , η from 1.9 % to 2.4 % (calculated)

Metallic nanostructures (back contact / semiconductor interface) *SPP/ photonic mode coupling.*	poly-Si thin-film, superstrate-configured [Ouyang et al, 2011]	Ag NPs, rear	Deposition + annealing	J_{SC} - 44 %	J_{SC} from14.85 to 21.42 mA/cm²
	a-Si thin-film, superstrate-configured [Chen et al,2012]	Ag NPs, rear	Synthesis + coating	J_{SC} - 14.3 % , η - 23 %	Highest η - 8.1 %
	a-Si thin-film, substrate-configured [[Ferry et al, 2011]	Ag nanostructure, rear	Nanoimprint lithography	J_{SC} - 47 % , η - 15 %	J_{SC} from 11.52 to 16.94 mA/ cm² , η from 6.32 % to 9.6 %
	n-i-p a-Si:H [Ferry et al, 2009]	Ag nanostructure, rear and front grating.	Nanoimprint Lithography (sol-gel imprint and FIB milling).	-	η - 6.16% Voc 0.81V, J_{SC} 12.5 mA/cm² FF 61%, λ from 600 to 800 nm
	n-i-p a-Si:H [Eminan et al, 2011]	Ag nanostructure, rear	Deposition (Sputter/ evaporation) + annealing	EQE enhancement factor of 2.5	Highest values; Voc 0.82 V, Jsc from 12.12 mA/cm², FF - 50% , λ from 700 to 800 nm

| | n-i-p a-Si:H [Ferry et al, 2010] | Ag nanostructure, rear | Nanoimprint Lithography (sol-gel imprint) | - | Highest values; η - 6.6%, Voc 0.89V, J_{SC} 13.4 mA/cm^2 , FF 66%, λ from 550 – 650 nm |

The arbitrary absorption, A, is one parameter that is usually simulated for both the transverse electric (TE) mode and the transverse magnetic (TM) mode with the ultimate objective being making both as close to unity as possible. It is important to note that absorption in this case is determined from:

$$A = 1 - T - R \qquad\qquad (2.1)$$

where T and R represent the transmitted and the reflected radiation respectively. However, as no radiation is transmitted through the PV devices with silvered back-contacts, Eq. 2.1 can therefore be reduced to:

$$A = 1 - R \qquad\qquad (2.2)$$

As seen in Eq. 2.2, the absorptivity of a cell is determined by its reflectivity; hence the goal of optical device simulation is aimed at reducing R as much as possible. Conventionally, reflectivity in solar cells are reduced by incorporating an anti-reflecting coating (ARC) on the front surface of the cell, and ITO is commonly used although it is not ideal. For example, the use of ITO as a front contact layer results in poor a-Si:H absorption at short wavelengths and increased sheet resistance, which is undesirable in high-efficiency solar cells [33]. In plasmonic PV devices, ITO is replaced with metallic nanostructures (metamaterial perfect absorbers), which are often embedded in a thin layer of transparent and non-conducting Si_3N_4, resulting in enhanced energy conversion efficiency over the entire visible spectrum [12]. Reflection losses are not the only optimization as it is important to also maximize the spectral absorption $A(\lambda)$ in the active absorber as that determines cell performance under solar illumination. Optimizing the device for fabrication involves changing nanostructure, size, shape and their periodic spacing until a significant enhancement in comparison to the reference device is achieved. To obtain a realistic device performance, the AM 1.5G spectrum [43] is integrated into the simulation resulting in $A(\lambda)$ over the entire spectrum. The incident P (λ) and output power, $P_{out}(\lambda)$ can be monitored, and using the relationship below, $A(\lambda)$ can be determined for different situations.

$$A(\lambda) = \frac{P_{in}(\lambda) - P_{out}(\lambda)}{P_{incident}(\lambda)} \qquad\qquad (2.3)$$

2.2.3 Electrical Properties Simulations

When simulating for electrical properties, two simplifying assumptions are usually made: 1) all absorbed photons will excite electron-hole (e-h) pairs, and 2) all photogenerated e-h pairs are successfully collected. Furthermore, these assumptions help to establish a link between simulated optical properties and

electrical properties hence making it possible to use Eq. 2.4 to calculate photocurrent density resulting from integrating $A(\lambda)$ and the normalized AM1.5G spectral photon flux density, $\varphi_{1.5}(\lambda)$ over the range of wavelengths:

$$J_{sc} = q \int \frac{A(\lambda)\Phi_{1.5}(\lambda)\lambda}{hc} \, d\lambda \qquad\qquad (2.4)$$

The most important cell performance parameters are its short circuit current, I_{sc}, maximum power current, I_{mp}, open circuit voltage, V_{oc} and the maximum power voltage, V_{mp}. However, the other performance parameter, the fill factor, FF, is commonly used to collectively describe the degree to which V_{mp} matches V_{oc} and I_{mp} matches I_{sc}.

Photocurrent enhancements have been reported in various studies involving plasmonic solar cells with different enhancement schemes. Relative photocurrent enhancement of 47% (11.52–16.94 mA/cm²) in a-Si thin film using Ag rear nanostructures [26], and 58% (4.6–7.3 mA/cm²) in organic P3HTPCBM using front Ag nanoparticles [44] with efficiency enhancements of 15% and 69% respectively, have been achieved using the scattering (far field) mechanism from either the front or back of the cell. Near field enhancement has achieved slightly lower photocurrent enhancement compared to the far-field enhancement: 20% (19–22.9 mA/cm²) for a-Si/c-Si hetero-junction using front Au nanoparticles [45], 44% (14.85–21.42 mA/cm²) for poly-Si thin film with rear Ag nanoparticles [46] and 60% for a-Si thin film with Ag front nanowire array was achieved through numerical simulation [47]. Efficiencies reported for metamaterials geometries related to solar cells have been mainly based on numerical simulation and mostly on MIM geometries instead of real PV devices. Although most models have achieved wide-angle broadband absorption, some have failed to quantify the photocurrent enhancement that could be achieved from their proposed cell geometries. Notable exceptions are Wang *et al.*, who used numerical simulation to calculate a maximum J_{sc} value of 19.7 mA/cm² for their a-Si:H based Ag metamaterials effective film cell [48]. They also reported a FF of 0.7 at V_{oc} of 0.87 V and J_{sc} of 4.6 mA/cm² [48]. In addition, Wu *et al.* reported a 41% efficiency improvement in their solar thermos-photovoltaic (STPV) cell also from numerical simulation [49].

2.3 Plasmonics for Improved Photovoltaic Cells Optical Properties

2.3.1 Light Trapping in Bulk Si Solar Cells

For the last 30 years it has been assumed that surface texturing in optical sheets can provide an intensity enhancement factor of $4n^2(x)$ for indirect bandgap semiconductors such as crystalline silicon [50]. Conventional thick c-Si-based solar cells have incorporated a pyramidal surface texture as a standard design for commercial devices [15]. In bulk c-Si solar cells, material costs account for 40% of the final module price [15]. This fact has been the main driver behind the growth of thin-film PV technologies as the reduction of material volume directly provides a reduction in materials costs.

Unfortunately, similar light enhancement through surface texturing is unsuitable for thin-film PV due to:

i. Geometrical limitations: Pyramidal texture features (microns in size) are usually much larger than the actual thin-film cell thickness [15, 17].

ii. Technical reasons: Although texturing of submicron features can be achieved through plasma etch techniques, this can damage the absorber and degrade the cell resulting in greatly reduced device efficiency [43]. Furthermore, texturing will result in increased surface area, which promotes greater minority carrier recombination.

New mechanisms for enhancing light trapping in thin-film PV have been proposed and investigated, and have shown that light coupling/enhancement into the substrate without increased recombination losses can be achieved through use of plasmonics.

2.3.2 Plasmonic Light-Trapping Mechanisms for Thin Film PV Devices

Plasmonic light-trapping techniques may provide considerable reduction in the PV material layer thickness by a factor ranging from 10 to 100 [6], while enhancing absorption through folding and concentrating [15] the incident light energy into the thin-film semiconductor layer. Three different techniques are used as shown schematically in Figure 2.3. In the mechanism described in Figure 2.3(a), metallic nanoparticles act as subwavelength scattering elements to preferentially scatter light into the high-index semiconductor substrate resulting in the anti-reflection effect over a broad spectrum [6, 15, 17] at the surface of the cell. Also, the angular redistribution of the scattered light folds light into thin absorber layers and further increases its optical path length. In addition, at the right nanostructure sizes and specific dielectric material properties, intense localized fields due to SP resonances may result and the energy from the surface plasmons may be emitted as light and

scattered in the direction of the semiconductor through a dipole effect [17, 51]. Incident sunlight is collected by subwavelength-scale metal particles with their large extinction cross section and reradiated into semiconductor in multiple angles to increase optical path length in thin-film photovoltaic layers.

(a)   Metallic nanoparticle (on top of the PV) dipole scattering – far field effect.
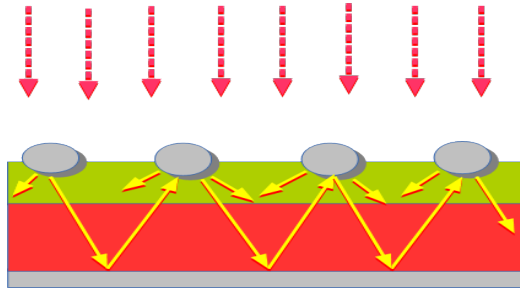
(b)   Metallic nanoparticle (embedded in the active semiconductor layer of PV) localized SPP field enhancement – near field effect.
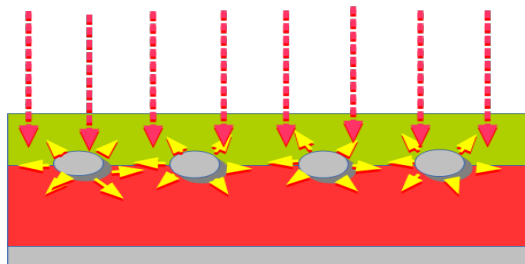
(c)   Metallic nanostructures (back contact / semiconductor interface) SPP/ photonic mode coupling.
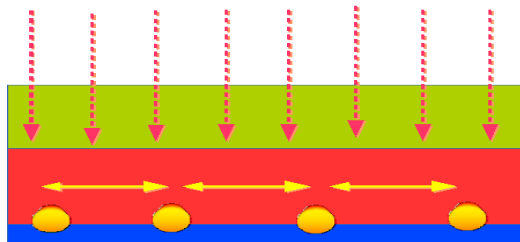
Figure 2.3. Schematic representation of three different plasmonic light trapping schemes for thin-film PV devices.

The second mechanism, shown in Figure 2.3(b), takes advantage of nanoparticles being used as subwavelength antennas with the ability to directly couple the

plasmonic near-field into the semiconductor thin-film layer through the near-field dipole effect. The plasmonic field near an emitting dipole is intense and localized to a few tens of nanometers around the nanoparticle, hence decreasing the spacing and particle size will further enhance this effect [17]. Furthermore, placing nanoparticles directly inside the semiconductor have been observed to directly excite electron-hole pairs leading to enhanced photogenerated charge collection facilitated by the presence of an enhanced electric field. Optical steering effects have also been suggested to contribute to overall enhancement [52]. The optical steering of light from subwavelength scale structures, which can be achieved by modifying the nano-antenna radiation pattern through changing the LSP resonances results in a form of wavelength dispersion at the nanoscale where light of different frequencies is scattered into different directions. This mechanism has shown potential in organic and direct bandgap semiconductors where carrier diffusion lengths are small and electron-hole pairs are usually generated close to the collection junction [6, 17].

The third mechanism, shown in Figure 2.3(c), involves the direct patterning of the metal back contact into some form of a back diffraction grating to trap the incident light at long wavelengths into guided SPP modes, in such a way to increase photon lifetime in the active medium [15, 53]. Generally, a solar cell designed for these types of plasmonics absorb the blue side of the spectrum effectively leaving the longer red wavelengths, which are then coupled into the waveguide or/and SPP modes propagating in the plane of the semiconductor layer [54]. However, for each photonic mode, part of the light will be absorbed into the semiconductor layer and part will be lost. The advantage of this mechanism, though, is that the incident solar flux is effectively rotated through an angle of $\pi/2$ radians therefore providing for light to be absorbed along the lateral dimensions of the solar cell [6] in which the cell dimensions are considerably larger than the optical absorption path length. Incident sunlight is coupled into surface plasmons propagating at the semiconductor-metal interface via subwavelength-size grooves to increase the optical path by switching the light direction from normal to the PV absorber layer to lateral to the PV absorber layer [55]. Since metallic back contacts are part of the standard design for most solar cells, nano-texturing of the back contact can be integrated into current fabrication techniques, although a substrate effect can hamper optimal semiconductor growth.

Considering design challenges associated with each of the proposed mechanisms above, currently, having nanoparticles/nanostructures on the front surface or back

contact have been the most preferred options by many researchers especially for inorganic thin-film PV technologies. The advantage of these approaches is that they enable semi-independent optimization of plasmonic properties of the cell as the optical properties are isolated from the electrical properties of the cell. However, having nanostructure within the semiconductor layer is still an active research area for groups working with organic and quantum dots based PV technologies.

2.3.3 Experimental Results

The most recent experimental enhancements and efficiencies of plasmonic PV devices are summarized in Table 2.1.

2.4 Fabrication Techniques and Economics

Current research in fabrication of plasmonic structures for PV is focused on reducing the fabrication cost in order to make plasmonic based light-trapping technologies economically viable. Plasmonic coupling mechanisms described in this chapter require stringent control of process parameters for integration of dense arrays of metal nanostructures with dimension tolerances at the nanometer scale. The majority of fabrication techniques used in most of the reviewed literature is based on cleanroom techniques such as electron-beam lithography (EBL) or focused ion-beam lithography (FIB).

These techniques allow precise control of design parameters of nanostructures at sub-wavelength scale; however, they are too expensive and not suitable for large-scale production. Large-scale, inexpensive and scalable fabrication techniques must be developed to enable giga-watt production of plasmonic-based PV modules.

2.4.1 Lithography Nanofabrication Techniques

Some of the most common fabrication techniques are summarized in Table 2.2.

Table 2.2. Common lithographic nanofabrication techniques for PV device fabrication.

Lithographic Technique	Types	Application in PV fabrication	Feature sizes	Comments
Electron beam lithography (EBL).	Direct write EBL	- Top surface nano-patterning - Back contact texturing	- Approximately 10 nm (single line)	- Well established technology - Good reproducibility

			- 20-40 nm (3D line)	- High spatial resolution - High precision - Fast turn-around - Low throughput and expensive (ideal for R&D but not suitable for large industries)
	Electron Projection Lithography (EPL)	- Top surface nano-patterning	- Approximately. 130 nm or less	- High precision - Critical dimensions still a concern - Incapable of fabricating complex nanostructures - Low throughput.
Ion-beam lithography	Focused ion-beam (FIB)	- Top surface nano-patterning	- 4 to 8 nm using Ga ion source	- High precision - Well established technology - Slow and expensive
	Deep-ion beam lithography (DIBL)	- Back contact texturing	- Less than 200 nm	- Expensive
Next generation lithography	Nano-imprint lithography (NIL)	- Top surface nano-patterning - Back contact texturing - Embossing silica sol-gel on glass substrate.	- 5 nm CDs are possible	- Most promising technology - Potentially economic - Creation of mask/stamp still time consuming and expensive
	Substrate conformal imprint lithography (SCIL)			
	Colloidal lithography	- Nanowires - Nanocones	- sub 10 nm feature sizes.	- Good precision

		- Nanoshells - Nanowells		- Not suitable yet for large scale production - Expensive
Others	X-ray, Extreme UV, Holographic, Dip pen lithography.	- Si solar cell back and front contact	- uses 13.4 nm λ to achieve less than 30 nm features for extreme UV - Approx. 0.3 μm or less for x –ray.	- 26 nm line achieved for EUV. - low throughput and expensive

Despite having well-established lithographic technologies for PV devices fabrication, challenges still exist regarding the cost of implementing the processes. The challenges are further compounded by the fact that most of the well-established processes are not only expensive, but they also have low throughput rendering them unattractive for large-scale industrial fabrication regardless of their capability to produce highly uniform sub 10 nm critical dimensions (CDs). To achieve large-scale fabrication and bring down the price of solar cells, fabrication processes such as EBL, FIB and other next generation lithographic (NGL) techniques must be adapted for high throughput so as to reduce the production costs through the economics of scale. The lithographic technique that has shown great potential for large-scale adoption is nanoimprint/softimprint lithography (NIL) [6, 15, 17, 26, 54, 56–57]. However, the stamp creation process is still considerably tedious and expensive.

2.4.2 Physical/Chemical Processing Techniques

Physical and chemical techniques can be described as the backbone of the semiconductor industry for both very traditional large-scale integration (VLSI) fabrication and the novel giga-watt PV industry. Deposition techniques such as atomic layer deposition (ALD) and molecular beam epitaxy (MBE) have presented researchers the flexibility to control precise device parameters such as doping and layer thickness through *in-situ* control of crystal growth at the atomic level. This has resulted in excellent film quality resulting in high-quality devices. However, these two techniques have low throughput and are currently expensive. On the contrary, chemical deposition processes such as plasma assisted/enhanced chemical vapor deposition (PACVD/PECVD), atmospheric pressure chemical

vapor deposition (APCVD) and metal-organic chemical vapor deposition (MOCVD) are well established large-scale fabrication techniques. PECVD is currently the standard fabrication technique for thin-film a-Si:H PV devices with f lm growth rates of 1 A°/s at 13.56 MHz giving optimum quality device performance [54, 65, 66]. Increasing this rate would be beneficial for large-scale fabrication and higher rates have been achieved with PECVD. Nanostructure and thin-film fabrication techniques are summarized in Table 2.3.

Table 2.3. Physical and chemical processes commonly used for PV devices fabrication

Physical/Chemical processing	Types	Application in PV fabrication	Advantages	Disadvantages
Physical Deposition	Atomic – Layer Deposition (ALD),	thin films isolating layers	· High aspect ratio and uniformity for nano-morphology fabrication · Pin-hole and particle free deposition is achieved · Excellent film quality and step coverage.	· high vacuum process · low throughput · Expensive process.
	Molecular Beam Epitaxy (MBE)	thin films	- precise control of compositions and morphology - in situ control of crystal growth at atomic level	low throughput expensive process
Physical Vapor Deposition (PVD)	Evaporation	thin films nanoparticles/ nanostructures	- High scale fabrication - less costly	high temperature process
	Sputtering	thin films etching	- high film uniformity - high etch rates	- introduces defects in film.

21

		nanostructures		
Chemical depositions	Chemical Vapor Deposition (PECVD, PACVD, APCVD, MOCVD, HWCVD)	thin film (semiconductor and organic) Si nanowires Single walled nanotubes ARC/ITO layers	- High throughput for large scale fabrication. - Well established technologies. - Low cost	- High vacuum equipment - highly toxic gases (requiring post process conditioning)
Nanoparticles fabrication processes	Wet chemistry (Sol-gel)	Nano-layers	- high purity from raw materials - good homogeneity from raw materials - high shape uniformity - low temperature process	- high cost of raw materials - long processing times - Health hazards of organic solutions - cracking and shrinkage
	Gas phase processing (pyrogenic and controlled detonation synthesis)	nanoparticles	- precise control of features sizes	- complex and expensive processes
	Mechanical milling	Nano-patterning	- precise control of features sizes around 10 nm scale	- complex and expensive processes
Others	High velocity deformation, mechano-chemical processes, plasma and flame spray	coatings metal nanoparticles	- high film uniformity	- low throughput - expensive process

2.5. Conclusion and Outlook

The potential of thin-film plasmonic-enhanced solar cells is evident from simulations reviewed in this chapter. There is a reason to be optimistic about the future of high-efficiency solar cells as demand and the cost of land escalates [2, 6,

17]. As fabrication techniques evolve, it will be possible to fabricate less expensive and higher efficiency thin-film solar cells based on plasmonic quantum dots, optical nano-antenna and other novel technologies. Quantum dot solar cells are being investigated and the results reported are promising. Quantum dots (or semiconductor nanocrystals) exhibit optical properties that are size dependent. Their absorption spectrum can be tuned, which has advantages for solar cells, where the nanocrystal size can be selected to optimize the absorption of nearly the entire AM 1.5 solar spectrum resulting in increased efficiency. QDs have demonstrated the ability to extract energy from "hot electrons," which is typically lost in conventional solar cells [67-69]. Some of the QDs-based solar cells demonstrated so far include a 20-nm-thick layer of CdSe semiconductor quantum dots deposited on a Ag film [70], and 11.6% (Au nanoparticles) or 10.9% (Ag nanoparticles) [49].

Future solar cells must provide low cost at high efficiencies closer to the thermodynamic limit of 93% [3]. Using tandem multi-junction cells with a series of varying bandgap materials stacked in decreasing order of bandgap is a promising option to circumvent the Shockley-Queisser limit of single bandgap devices [17, 55]. A balance limit calculation estimated that a 36-junction cell ideally would reach 72% efficiency at a concentration of 1,000 suns relative to the 37% for a 1-junction device [71]. Plasmonic tandem solar cells can be designed by stacking layers of QDs of increasing size from the top to the bottom of the cell, or nanoparticles imbedded in semiconductor material in a similar manner. By variation of particle or dots size, it is possible to absorb from the blue (at the top of the cell) to the red (at the bottom) wavelengths of the solar spectrum using minimal material resources. An alternative structure would be to have semiconductors of different bandgaps stacked on top of each other separated by plasmonic structured metal films, each optimized for different optical spectral bands.

Acknowledgements

References

1. J. Pearce, Photovoltaics - A Path to Sustainable Futures. Futures 34(7), 663-674 (2002).

2. K. Branker, M. J.M. Pathak, J. M. Pearce, "A Review of Solar Photovoltaic Levelized Cost of Electricity", Renewable & Sustainable Energy Reviews 15, pp.4470-4482 (2011).

3. M.A. Green, Third Generation Photovoltaics: Advanced Solar Energy Conversion,

4. Springer-Verlag, Berling, 2003.

5. Woodcock, J. M., H. Schade, H. Maurus, B. Dimmler, J. Springer, and A. Ricaud. "A Study of the upscaling of thin film solar cell manufacture towards 500 MWp per annum." In Proceedings of the 14th European Solar Energy Conference, Barcelona, pp. 857-860. 1997.

6. M.A. Green, Third Generation Photovoltaics, Springer, 2005.

7. H. A. Atwater, and A. Polman. "Plasmonics for improved photovoltaic devices." Nature materials 9, no. 3 (2010): 205-213.

8. Roco, M.C., Mirkin, C.A. and Hersam, M.C., 2011. Nanotechnology research directions for societal needs in 2020: summary of international study. Journal of nanoparticle research, 13(3), pp.897-919.

9. F. Zhu, P.J. Jennings, J.C.L Cornish, G. Hefter, C.P. Lund, 35th Ann. Conf. of the

10. Australian and New Zealand Solar Energy Soc., December, Canberra, 1997.

11. S.A. Maier, Plasmonics: Fundamentals and Applications. Springer, 2007.

12. Halas NJ. Plasmonics: an emerging field fostered by Nano Letters. Nano letters. 2010 (10):3816-22.

13. Rand, B.P., Peumans, P. and Forrest, S.R., Long-range absorption enhancement in organic tandem thin-film solar cells containing silver nanoclusters. Journal of Applied Physics, 96(12), pp.7519-7526, 2004.

14. Schaadt, D. M., B. Feng, and E. T. Yu. "Enhanced semiconductor optical absorption via surface plasmon excitation in metal nanoparticles." Applied Physics Letters 86, no. 6 (2005): 063106.

15. V. Zayats, I. I. Smolyaninov, and A. A. Maradudin, "Nano-optics of surface plasmon polaritons,"Phys. Rep. 408, 131–314 (2005).

16. J.M. Pitarke, V.M. Silkin, E.V. Chulkov, P.M. Echenique, Rep. on Prog. in Phys.Vol. 70, no. 1, pp. 1–87, 2007.

17. P. Spinelli, V.E. Ferry, J. van de Groep, M. van Lare, M.A. Verschuuren, R.E.I.

18. Schropp, H.A. Atwater, A. Polman, J. Opt., Vol. 14, no. 2, p. 024002, 2012.

19. S. Hayashi, T. Okamoto, J. Phys. D: App. Phys., Vol. 45, no. 43, p. 433001, 2012.

20. S. Pillai, M.A. Green, Sol. Energ. Mat. and Sol. Cells, Vol. 94, no. 9, p. 1481, 2010.

21. W. Cai, V. M. Šalaev, Optical Metamaterials: Fundamentals and Applications. Springer, 2009.

22. S.A. Maier, H.A. Atwater, J. Appl. Phys. Vol. 98, p. 011101, 2005.

23. A. Sihvola, Metamaterials, Vol. 1, no. 1, p. 2, 2007.

24. K. Aydin, V.E. Ferry, R.M. Briggs, H.A. Atwater, Nat. Comm., Vol. 2, p. 517, 2011.

25. S.Y. Chou, W. Ding, Opt. Express, Vol. 21, p. A60, 2013.

26. S. Lal, S. Link, N.J. Halas, Nat. Photon., Vol. 1, no. 11, p. 641, 2007.

27. N. Verellen, Y. Sonnefraud, H. Sobhani, F. Hao, V.V. Moshchalkov, P.V. Dorpe,

28. P. Nordlander, S.A. Maier, Nano Lett., Vol. 9, no. 4, p. 1663, 2009.

29. C. Wu, Y. Avitzour, G. Shvets, Proc. of SPIE Vol. 7029, p. 70290W, 2008.

30. V.E. Ferry, M.A. Verschuuren, C. van Lare, E.I. Ruud, H.A. Atwater, A. Polman, Nano Lett. Vol. 11, p.4239, 2011.

31. C.R. Wronski, J.M. Pearce, R.J. Koval, X. Niu, A.S. Ferlauto, J. Koh, R.W. Collins. Mat. Res. Soc. Symp. Proc. Vol. 715, p. A13.4, 2002.

32. J. Trevino, C. Forestiere, G. Di Martino, S. Yerci, F. Priolo, L. Dal Negro, Optics Express, Vol. 20, no. S3, p. A418, 2012.

33. A. Aubry, D.Y. Lei, A.I. Fernández-Domínguez, Y. Sonnefraud, S.A. Maier, J.B. Pendry. Nano Letters, Vol. 10, no. 7, p. 2574, 2010.

34. F.J. Beck, S. Mokkapati, A. Polman, K.R. Catchpole. App. Phys. Lett., Vol. 96, no. 3, pp. 033113, 2010.

35. J.R. Cole, N.J. Halas. App. Phys. Lett., Vol. 89, no. 15, p. 153120, 2006.

36. M.A. Green, S. Pillai, Nat. Photon., Vol. 6, no. 3, p. 130, 2012.

37. Massiot, C. Colin, N. Pere-Laperne, P. Roca i Cabarrocas, C. Sauvan, P. Lalanne, J.-L. Pelouard, S. Collin. Appl. Phys. Lett., Vol. 101, no. 16, p. 163901, 2012.

38. P.B. Johnson, R.W. Christy. Phys. Rev. B, Vol. 6, no. 12, p. 4370, 1972.

39. E.D. Palik, Handbook of optical constants of solids. Orlando: Academic Press, 1985.

40. H. Fujiwara, Spectroscopic ellipsometry: principles and applications. Wiley, 2007.

41. D.Ö. Güney, T. Koschny, C. M. Soukoulis, Phys. Rev. B, Vol. 80, p. 125129, 2009.

42. M. Diem, Th. Koschny, C. M. Soukoulis, Phys. Rev. B, Vol. 79, p. 033101, 2009.

43. X., Liu, T., Starr, A.F., Starr, W.J., Padilla, Phys. Rev. Lett., Vol. 104, p. 207403, 2010.

44. K.B. Alici, A.B. Turhan, C.M. Soukoulis, E. Ozbay, Opt. Express, Vol. 15, p. 14260, 2011.

45. C. Wu, G. Shvets, Opt. Lett., Vol. 37, p. 308, 2012.

46. Y. Cui, J. Xu, K.H. Fung, Y. Jin, A. Kumar, N.X. Fang, Appl. Phys. Lett. Vol. 99, p. 253101, 2011.

47. S. Pillai, K.R. Catchpole, T. Trupke, M.A. Green, J. Appl. Phys., Vol. 101, no. 9, p. 093105, 2007.

48. A.J. Morfa, K.L. Rowlen, T.H. Reilly, M.J. Romero, J. van de Lagemaat, Appl. Phys. Lett. Vol. 92, p. 013504, 2008.

49. M. Losurdo, M.M. Giangregorio, G.V. Bianco, A. Sacchetti, P. Capezzuto, G. Bruno, Solar Energy Mat. and Sol. Cells, Vol. 93, no. 10, p. 1749, 2009.

50. Z. Ouyang, X., Zhao, S., Varlamov, Y., Tao, J., Wong, Pillai, Supriya, Prog. Photovoltaics Res. Appl. Vol. 19, p. 917, 2011.

51. C. Rockstuhl, S., Fahr, F., Lederer, J. Appl. Phys. Vol. 104, p. 123102, 2008.

52. Y. Wang, T., Sun, T., Paudel, Y., Zhang, Z., Ren, K., Kempa, Nano Lett. Vol. 12, p. 440, 2011.

53. C. Wu, B. N. Iii, J. John, A. Milder, B. Zollars, S. Savoy, G. Shvets, J. Opt., Vol. 14, p. 024005, 2012.

54. E. Yablonovitch, G. D. Cody. IEEE Trans. Elec. Dev. Vol. 29, no. 2, p. 300, 1982.

55. B. S. Luk'yanchuk, M. I. Tribel'ski, V. V. Ternovski, J. Opt. Technol., Vol. 73, no. 6, p. 371, 2006.

56. A., Djalalian-Assl, D.E., Gómez, A., Roberts, T.J., Davis, Opt. Lett. Vol. 37, p. 4206, 2012.

57. M. Yang, Z. Fu, F. Lin, X. Zhu, Opt. Express, Vol. 19, no. S4, p. A763, 2011.

58. V. E. Ferry, M. A. Verschuuren, H. B. T. Li, E. Verhagen, R. J. Walters, R. E. I. Schropp,

59. H. A. Atwater, A. Polman. Proc. 25th EU-PVSEC Conference, Valencia, 2010.

60. Tanabe, Energies, Vol. 2, no. 3, p. 504, 2009.

61. M. J. Madou. Fundamentals of Microfabrication and Nanotechnology: Manufacturing Techniques for microfabrication and nanotechnology. CRC Press, 2011.

62. Derkacs, S. H. Lim, P. Matheu, W. Mar, E. T. Yu. Appl. Phys. Lett. Vol. 89, p. 093103, 2006.

63. N. F. Fahim, B. Jia, Z. Shi, M. Gu, and S. Kim, Opt. Express Vol. 20, p. A694–A705, 2012.

64. T. L. Temple, G. D. K. Mahanama, H. S. Reehal, D. M. Bagnall, Solar Energy Mat. and Solar Cells, Vol. 93, no. 11, p. 1978, 2009.

65. Nakayama, K. Tanabe, H.A. Atwater, Appl. Phys. Lett. Vol. 93, p. 121904, 2008.

66. H. Lee, J. H. Park, J. S. Kim, D. Y. Lee, K. Cho,. Organic Electronics, Vol. 10, no. 3, p. 416, 2009.

67. J.-Y. Wang, F.-J. Tsai, J.-J. Huang, C.-Y. Chen, N. Li, Y.-W. Kiang, and C. C. Yang, Opt. Express, Vol. 18, no. 3, p. 2682, 2010.

68. X. Chen, B. Jia, J. K. Saha, B. Cai, N. Stokes, Q. Qiao, Y. Wang, Z. Shi, M. Gu, Nano Lett., Vol. 12, no. 5, p. 2187, 2012.

69. C. Eminian, F.-J. Haug, O. Cubero, X. Niquille, and C. Ballif, Prog. Photovolt.: Research and Appl., Vol. 19, no. 3, p. 260, 2011.

70. R. E. I. Schropp, K. F. Feenstra, E. C. Molenbroek, H. Meiling, J. K. Rath, Phil. Mag. Part B, Vol. 76, no. 3, p. 309, 1997.

71. R.W. Collins, A.S. Ferlauto, G.M. Ferreira, C. Chen, J. Koh, R.J. Koval, Y. Lee, J.M. Pearce, C. R. Wronski, Solar Energy Mat. and Solar Cells, Vol. 78, p. 143, 2003.

72. A.J. Nozik, Phys. E Low-Dimens. Syst. Nanostructures Vol. 14, p. 115, 2002.

73. A., Luque, A. Martí, A.J. Nozik, MRS Bull. Vol. 32, p. 236, 2007.

74. A.J. Nozik, M.C. Beard, J.M. Luther, M. Law, R.J. Ellingson, J.C. Johnson, Chem. Rev. Vol. 110, p. 6873, 2010.

75. D. Pacifici, H. J. Lezec, H. A. Atwater. Nat Photon, Vol. 1, no. 7, p. 402, 2007.

76. C.H. Henry. Limiting efficiencies of ideal single and multiple energy-gap terrestrial solar-cells. J. Appl. Phys. . 1980, 51, 4494–4500.

3. Limitations of Ultra-Thin Transparent Conducting Oxides for Integration into Plasmonic-Enhanced Thin Film Solar Photovoltaic Devices[2]

3.1 Introduction

Despite the material, sustainability, economic and technical benefits of thin-film solar photovoltaic (PV) devices [1–3], conventional crystalline silicon (c-Si) modules dominate the market [4]. The cost of c-Si PV has fallen to the point that the balance of systems (BOS) and thus the efficiency of the modules plays a major role in the levelized cost of electricity for solar [5]. There is thus a clear need to improve the efficiency of thin-film devices further [6]. Recent developments in plasmonics theory promise new methods with great potential to enhance light trapping in thin-film PV devices [7–14]. To fully exploit these potential benefits offered by plasmonic-based devices, TCOs with high transmittance (low loss) and low enough resistivity are to be used as device top contacts. However, for current transparent conducting oxides (TCOs) to be successfully integrated into the novel proposed plasmonic enhanced PV devices, ultra-thin TCOs films are required [14]. For example, simulations by Vora et al. showed a 19.65 % increase in short circuit current (Jsc) for nano-cylinder patterned solar cell (NCPSC) in which the ITO layer thickness was kept at 10 nm to minimize the parasitic Ohmic losses and simultaneously act as a buffer layer while helping to tune the resonance for maximum absorption [14]. TCOs such as the most established indium tin oxide (ITO), aluminum-doped zinc oxide (AZO) and zinc oxide (ZnO) are standard integral materials in current thin-film solar PV devices [15–18]. Bulk material properties for common TCOs including ITO have been well researched and documented for different processing conditions and substrates [15, 16, 19–23]; however, this is not the case for ultra-thin TCOs. The few exceptions include Sychkova et al. [24], who reported both optical and electrical properties of 9–80 nm ITO films deposited by pulsed DC sputtering varied with thickness and showed a general increase in resistivity with decrease in film thickness [24]. Other notable studies on ultra-thin ITO films using various deposition techniques include the following: Chen et al. who used filtered cathodic vacuum arc (FCVA) to deposit

---

[2] "The material contained in this chapter is previously published in *Mater Renew Sustain Energy*".

30–50 nm on heated quartz and Si substrates [25]; Tseng and Lo, who used DC magnetron sputter for 34.71–71.64 nm ITO film on PET (polyethylene terephthalate) [26]; Kim et al. who used RF magnetron sputter for films between 40 and 280 nm deposited on PMMA substrate heated at 70 ^{0}C [27]; Alam and Cameron, who used sol–gel process for 50–250 nm film deposited on titanium dioxide film [20]; and Betz et al. who used planar DC magnetron sputtering for 50, 100 and 300 nm films on glass substrates [28]. The results from these few thin TCO studies reveal a pattern in which resistivity increases rapidly as film thickness decreases from 50 to 10 nm.

The electrical properties of ITO thin films depend on the preparation method, the deposition parameters used for a given deposition technique and the subsequent heat treatments. Key factors for the low resistivity have not been clearly documented because of the complex structure of the unit cell of crystalline In_2O_3 formed by 80 atoms and the complex nature of the conducting mechanisms in polycrystalline films [29]. The issue is further complicated by the large number of processing parameters, even for a single technique. To probe these challenges and to determine if ITO, AZO and ZnO are viable candidate materials for use in plasmonic- enhanced thin-film PV devices, sensitivity analysis on TCO thickness (10–50 nm) versus absorption was performed using COMSOL Multiphysics RF module v4.3b on the optical absorption in the i-a-Si:H layer of nano-disk patterned thin-film a-Si:H solar cells (NDPSC) shown in Fig. 3.1.a [15]. These simulation results are used to guide the experimental work which investigated both optical and electrical properties of ultra-thin (10 nm on average) films simultaneously deposited on both glass and silicon substrates (with a thermally grown oxide layer. The effects of deposition and post-processing parameters on material properties of ITO, AZO and ZnO ultra-thin TCOs were probed and the suitability of TCOs for integration into plasmonic-enhanced thin-film solar PV devices was assessed. From these results some of the limitations of thin TCOs for plasmonic optical enhancement of thin-film PV were identified.

3.2 The optical effects of TCO thickness

Sensitivity analysis for the proposed silver nano-disk patterned solar cell (NDPSC) was performed in the 300–750 nm spectral range to determine the optimum ITO layer thickness which would promote maximum enhancement and minimize Ohmic losses. Having a TCO spacer layer with as low as possible Ohmic losses is desirable for efficient coupling of light from the silver nano-discs into the active

layers of the device. The results are shown in Fig. 3.1.b and theoretically show 10 nm films offer the best absorption and hence the greatest potential to improve efficiency in plasmonic-based PV devices. From these results, AZO and ITO offer the best potential due to lower Ohmic losses and ZnO, despite having the greatest Ohmic losses among the three TCOs, is still promising particularly for the sub 20 nm films since its absorption (>250 W/m2) is still higher than that expected of a standard PV device.

3.3 Experimental details

The focus of the study was to investigate ways of improving material properties of ultra-thin TCOs for integration into plasmonic-enhanced thin-film solar PV devices by studying the effects of different process parameters on both optical and electrical properties of sub 50 nm films. A comparative study of the three most commonly used TCOs in thin-film commercial solar cells is undertaken, and a more in-depth study of ITO is performed.

3.3.1. Sample preparation and fabrication

Samples of ITO with thickness ranging from 10 to 50 nm were deposited on both glass and n-doped silicon (with a 32-nm thermally grown oxide layer) substrates using rf sputter deposition techniques previously described in refs [30–32].

(a)

Period of unit cell: 550 nm

Dia of cylinder: 240 nm

Height of cylinder: 50 nm

ITO 10 nm on top of p layer

Standard solar cell Parametrs as measured through ellipsometry

Period of unit cell: 550 nm

Nano cylinder is of silver

(b)
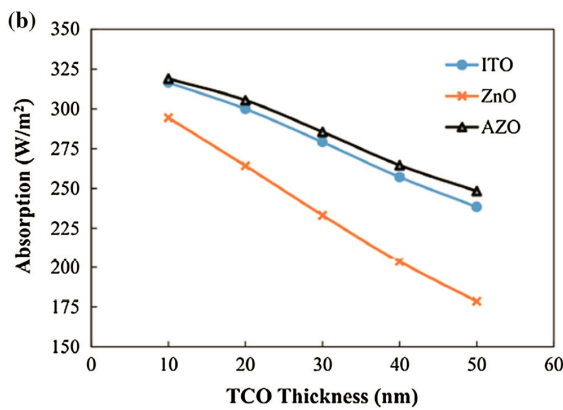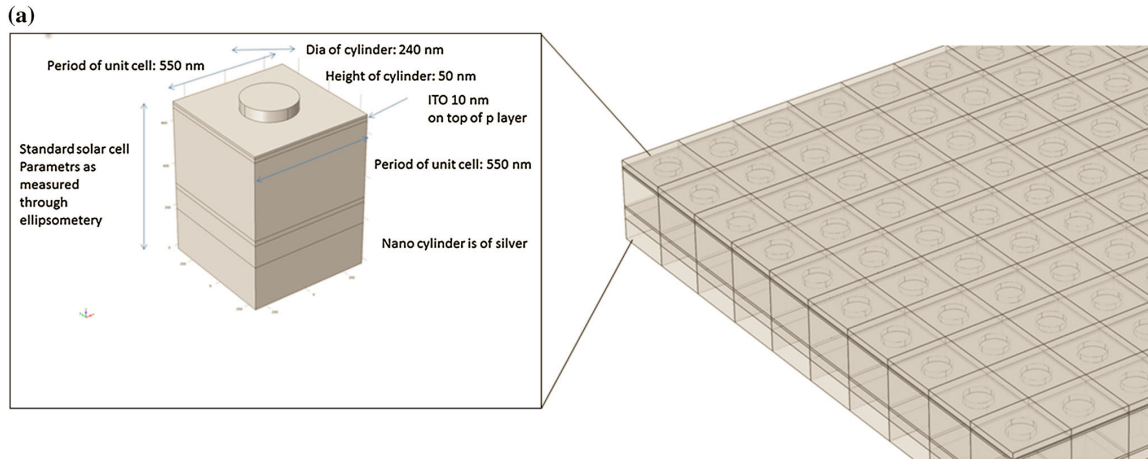
Figure 3.1 a Structure of the NDPSC with an enlarged unit cell, b absorption as a function of ITO, ZnO and AZO thickness. The results simulated using COMSOL show how the useful optical absorption in the active regions of plasmonic PV devices varies with TCO type and thickness. Theoretically, at small film thicknesses Ohmic losses decrease and useful optical absorption increases [15]

A 99.99 % 4-inch pressed ITO (Sn_2O:In_2O_3 10:90 % wt) target was used, and an average base pressure of 7×10^{-8} Torr was achieved before deposition. Both the glass and silicon substrates were ultrasonically cleaned in isopropanol for 5 min. All other process parameters such as target bias [900 V (ITO and ZnO) and -500 V (AZO)] and substrate distance (75 mm) were kept constant through the experiment. Substrates and target were sputter pre-cleaned in an argon environment for 5 min before each run. The protocol for pre-cleaning is described in Ref. [29].

To investigate substrate dependency, ITO was deposited on a pair of substrates for 1 min with 0 % oxygen ratio and 100 W rf power. ZnO samples were processed at rf power of 100 W on glass and silicon substrates in an argon environment and 0 % oxygen in the same system as ITO using a stoichiometric

99.99 % 4-inch pressed ZnO target. The process pressure was maintained at 7.1 x 10^{-3} torr and the deposition rate was calculated to be 8 nm/min. AZO was processed using a Perkin–Elmer Model 2400-8 J rf sputter deposition system using an 8-inch (203.2 mm) target. The rf power was kept at 500 W, argon flow rate at 18.0 sccm, oxygen rate of 2.0 sccm and process pressure at 7.3 x 10^{-3} Torr. The system was initially pumped to a base pressure of 6.0 x10^{-8} Torr. The process parameters are summarized in Table 3.1.

Table 3.1. Summary for optical parameters for TCOs.

Sample name	TCO	Substrate type	RF Power (W)	Target Bias (V)	Process gases flow rates (sccm)		Film Thickness (nm)
					Ar	O_2	
0A	ITO	Glass					9.55
0B		Si/SiO$_2$					10.02
1A$_1$		Glass					19.92
1A$_2$		Si					19.75
1B							10.23
1C		glass					20.01
1D							30.79
1E			100	900	10	0	39.70
1F							50.03
2A$_1$	ZnO	Glass					9.51
2A$_2$							10.05
2B							20.01
2C		Si / SiO$_2$					29.72
2D							38.98
2E							48.31
3A	AZO	Glass					12.16
3B							11.93
3C		Si / SiO$_2$	500	500	18.0	2.0	20.39
3D							30.04
3E							40.63

To investigate the effects of post-processing treatment on both optical and electrical effects, additional samples of ITO films on sodalime glass (SLG) substrates were processed using a different instrument [33] to obtain a pair of film samples with varying thicknesses from 10 to 50 nm in steps of 10 nm. The system is a four-gun sputtering system with a target to substrate spacing of approximately 4-inch. An ITO (90 % In_2O_3/10 % SnO_2 from Lesker) target was used. The material was sputtered using 100 W rf under 4 mTorr of Ar. Deposition time was varied for film thickness with 36 s resulting in 10 nm (~3 A/sec). This deposition rate was

determined by depositing for a set amount of time and measuring the resulting film thickness using stylus profilometry (Veeco Dektak 150).

One sample for each as-deposited pair was divided into three samples using a diamond scriber. The three pieces were then annealed separately at 400 ^{0}C for 10, 20 and 30 min, respectively, using UHP forming gas (FG) (95 % N_2/5 % H_2 from Air Gas) in a sealed (by vacuum coupling components) quartz tube inside a tube furnace. The furnace was equilibrated at the heating temperature prior to sample introduction. The samples were placed in the quartz tube; then the tube was purged with FG at 5 scfm for 5 min—this was approximately four exchanges of tube volume. After purging, the samples were introduced into the hot zone with a vacuum-sealed push rod, and the flow rate was reduced to approximately 150 sccm for the duration of heating. After heating, the samples were removed from the hot zone and cooled by increasing the gas flow. After characterization, the sample previously annealed at 400 ^{0}C for 30 min was further annealed at 500 ^{0}C for 10 min.

3.3.2. Optical and electrical characterization process

The film thickness measurements and optical characterization were carried out using spectroscopic ellipsometry (J.A Woollam Co UV–VIS V-VASE with control module VB-400). In each case, a standard scan was performed ranging from 300 to 1000 nm in increments of 10 nm for the 65^0, 70^0 and 75^0 incident angles. Random detailed scans were performed for the quality check purposes although they are normally not necessary for isotropic samples. Ellipsometry analysis was performed following the process by Synchkova [24]. Intensity measurements were carried out using the VASE for normal transmission incidence (0^0 reflection angle) for the three TCOs on glass substrates for the same wavelength range as above. A baseline scan was obtained for the clean SLG substrate first followed by the main data scans using baseline data. Both the baseline and the data scans were acquired in close successions to minimize errors due to light source intensity fluctuations. Electrical characterization was performed using a four-point probe (4-PP) system consisting of ITO optimized tips consisting of 500 micron tip radii set to 60 g pressure and an RM3000 test unit from Jandel Engineering Limited, UK. The sheet resistance of the 10 and 20 nm TCOs on glass and on silicon substrates with a spacer oxide layer was determined by direct measurement for both forward and reverse currents. For each TCO on glass sample, a mean sheet resistance value

from three random points was used in the final results whilst a mean of only two points was used for the TCO on Si samples since they were smaller.

All samples were imaged for film quality and a compositional analysis was done using a Hitachi S4700 field emission scanning electron microscope (FE-SEM). Atomic force microscopy (AFM) was performed using a Veeco Dimension 3000 equipment with cantilever tips (Tap300Al-G) on a 1:1 acquisition aspect ratio. The field of view was 2 lm at 512 pixel width and scans performed at a speed of 0.5 Hz. Three randomly selected fields of view were acquired per sample and the analyzed areas were limited near to the center of the sample. Roughness analysis was then performed on a defect-free region.

3.4. Theory and calculations

The theoretical derivations of both the resistivity and attenuation coefficient of the ITO films are highlighted in Sects. 3.1 and 3.2 below to explain the underlying processes contributing to the results reported in this paper.

3.4.1. Resistivity measurements

Sheet resistance measurement was used to obtain the resistivity:

$$ R = R_s \frac{L}{W} \frac{d}{t} $$ (3.1)

where R is the resistance, Rs is the sheet resistance, and L, W and t are the sheet length, width and thickness, respectively.

As the film thickness is measured, the bulk resistivity q (in ohm cm) can be calculated by multiplying the sheet resistance by the film thickness in cm:

$$ \rho \times t $$ (3.2)

3.4.2. Transmittance

To determine the true transmittance of the TCOs, it was necessary to perform a correction on the experimental data to compensate for losses due to both surface reflection and absorption due to the glass substrate. It is assumed light passing through the glass substrate undergoes attenuation according to Beer-Lambert's law:

$$ I_g = I_o e^{-\alpha_g t_g} $$ (3.3)

35

where I_0 and I_g represent the initial incident intensity and intensity through the glass substrate, α_g and t_g are the attenuation coefficient of the glass and glass thickness, respectively.

The total normalized transmittance, T is given by;

$$\tag{3.4}$$

where A and R represent the total absorbance and reflectance, respectively.

3.5. Results and Discussion

3.5.1. TCOs characterization

The transmittance and resistivity measurements results for the TCOs are discussed below.

3.5.1.1. Transmittance

Fig 3.2 below shows how transmittance of the TCOs studied varied within the 300 to 1000 nm wavelength range.
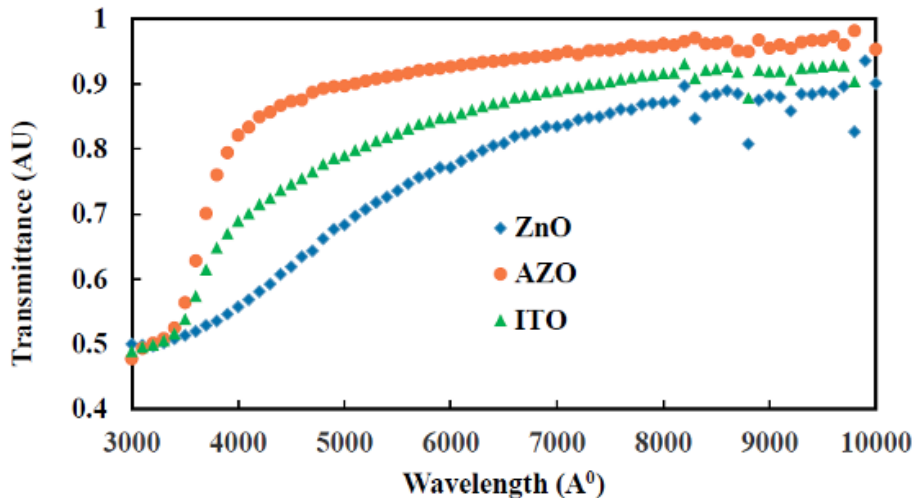
Figure 3.2. Transmittance results for 20 nm thick ITO, ZnO and AZO films. Transmittance results support the sensitivity analysis results. For the 20 nm films, AZO has greater than 90% transmittance for the 300 – 1000 wavelength range, whilst ITO and ZnO show an average transmittance greater than 80% and 70%, respectively, in the same spectral range.

3.5.1.2 Sheet Resistance

The resistivity of the 20 nm as-deposited TCO films on SLG substrates are shown in Table 3.2. ZnO, despite having the worst transmittance (Fig 3.2), has the lowest resistivity among the three TCOs being compared here and AZO has the highest resistivity value. ITO has transmittance comparable to that of AZO and its resistivity is slightly higher than that of ZnO making it the most promising candidate material for plasmonic based devices.

Table 3.2. Resistivity of 20 nm as-deposited ITO, AZO and ZnO films on SLG substrates.

Sample	Substrate	Thickness (nm)	Sheet Resistance, R_s ($\Omega/\square$) x 10^3	Resisitivity,ρ (Ω.cm)
ITO	glass	20	623	1.3×10^{-3}
AZO	glass	20	876	1.7×10^{-3}
ZnO	glass	20	390	7.8×10^{-4}

Table 3.3 shows the dependence of ITO sheet resistance with substrate type and thickness. There was a marked difference between the readings on the 10 nm and 20 nm on Si samples, however there was no discernible difference between the readings on the 10 nm and 20 nm on glass.

Table 3.3. Sheet resistance of various as deposited TCO samples

Sample	Substrate	Thickness (nm)	Input current	Sheet Resistance, R_s ($\Omega/\square$) x 10^3	Resisitivity,ρ (Ω.cm)
ITO	glass	10	100 nA	830	8.3×10^{-4}
		20		623	1.3×10^{-3}
	Si	10	1 μA	422	4.2×10^{-4}
		20		83.9	1.7×10^{-4}

There were very small amounts of fluctuation which can be expected on high resistance samples, and it was more prominent on the Si samples. The readings reversed well, indicating that the film was uniform, with the worst correlation on the 10 nm Si sample. This is the limit of four point probe capability. The 10 nm ITO on glass showed the highest resistivity whilst the lowest resistivity value was recorded for the 20 nm on Si substrate sample. The results are further confirmed by the nature of the microstructure observed by SEM (*vide infra*) for these samples.

3.5.2. ITO characterization

3.5.2.1. Transmittance measurements for ITO

Transmittance measurements for ITO samples deposited on SLG substrates are shown in Fig. 3.3. All transmittance values were normalized as given in equation (4). It can be noted that there is no discernible difference between the as-deposited and the heat treated samples particularly for the 30 nm, 40 nm and 50 nm films. However, it is also interesting to note that for the 10 nm and 20 nm films, the as-deposited films have the highest transmittance with the 10 nm film being almost 100% transmitting throughout the visible spectra. For the 40 nm film, annealing at 400 ^{0}C for 20 minutes gives the best transmittance. Generally it is observed that heat treated ITO films in FG environment improves transmittance in the UV region of the spectra.

(a)

- as-deposited
- 10 min
- 20 min
- 30 min

(b)

- as-deposited
- 10 min
- 20 min
- 30 min
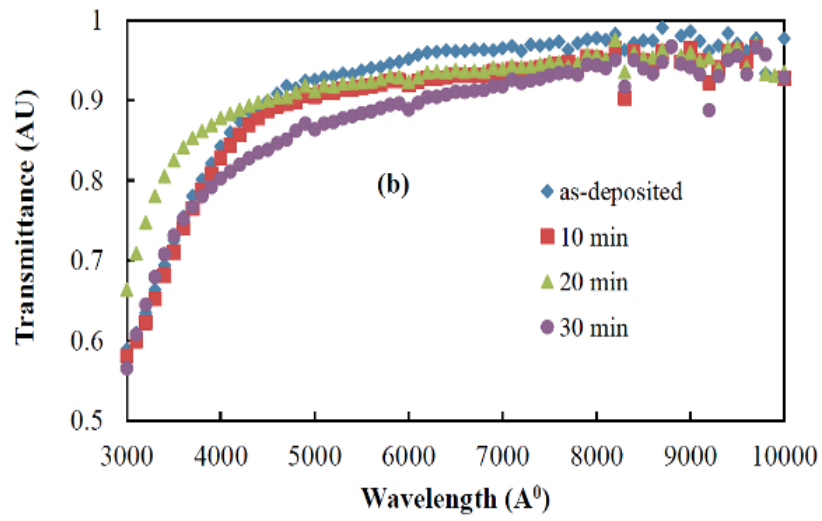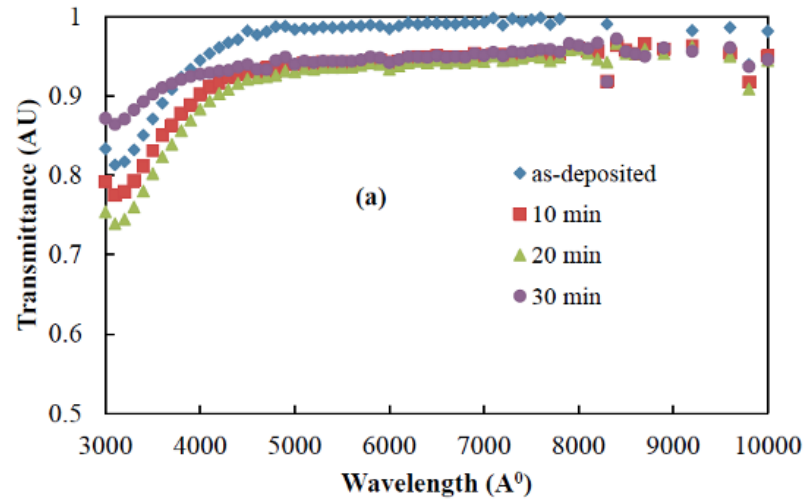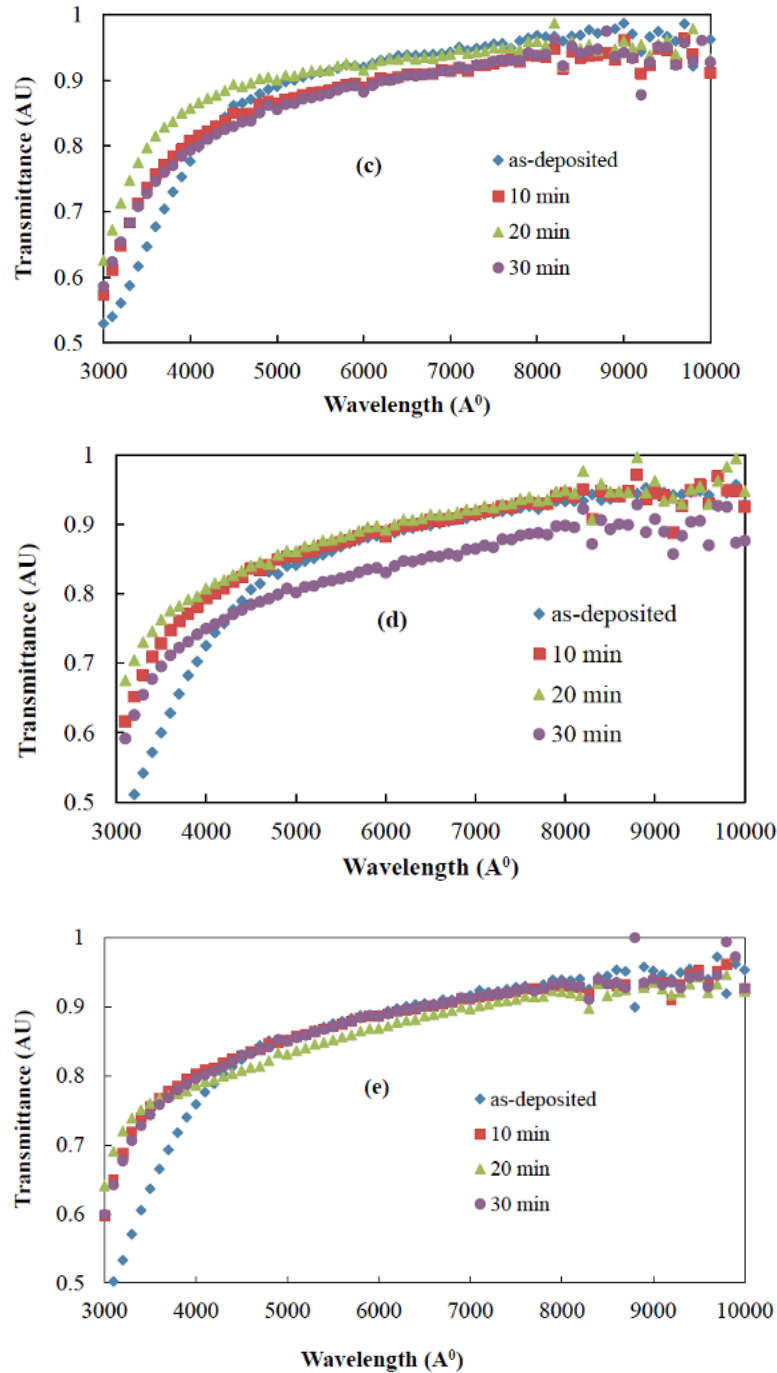
Figure 3.3. Transmittance spectra for ITO as-deposited and annealed films on sodalime glass for (a) 10 nm, (b) 20 nm, (c) 30 nm, (d) 40 nm, and I 50 nm ITO thickness.

As-deposited thinner ITO samples (10 and 20 nm) have the transmittance greater than 95%. It is interesting to note that the 40 nm film sample does not seem to follow this general trend, particularly the sample annealed for 20 minutes. This

sample film shows the greatest increase in mean roughness (*vida infra*) when all other films' roughness are decreasing and it also has the best transmission for all the 40 nm film samples. The general trend is that the overall transmittance curve for the as-deposited ITO shifts down with increasing film thickness (i.e., the as-deposited film becomes less transparent with increasing thickness as expected). Around visible spectrum and at higher wavelengths, the transmittance for the as-deposited ITO approaches to that of the annealed ITO (i.e., annealing is not much effective here in improving transparency). However, around UV wavelengths the transmittance for the as-deposited ITO shifts down below that of the annealed samples (i.e., at small wavelengths annealing is more effective as the annealed samples are more transparent). This is a well-known phenomenon (Burstein – Mess Shift) which is a result of ITO optical band gap shifting towards higher energies when annealed in FG or H_2 gas. This is attributed to increase in carrier concentration and is well documented [25]. In addition, it appears that among the annealed samples, 20 min gives the optimum transmittance for thicknesses below 50nm especially at large wavelengths. There observed trend means that the use of thinner (10 nm), more transmitting and low loss (Ohmic losses) films will result in more light being coupled into the underlying i-a-Si:H layer rather than being absorbed in the TCO layer as is the case with thicker film (>20 nm).

3.5.2.2. Electrical Characterization

Fig. 3.4 shows the dependence of sheet resistance on film thickness, annealing temperature and time. Films annealed for 20 min gives the lowest resistivity and show the same trend as those annealed for 30 minutes whilst the as-deposited resistivity versus thickness trend in similar to film annealed for 10 minutes. Results here show that annealing in FG lowers the resistivity. The lowest resistivity of approximately 4 x 10^{-4} Ωcm is for the 40 nm film annealed for 20 minutes. The highest resistivity value for the annealed samples is for the 20 nm film annealed for 10 min.
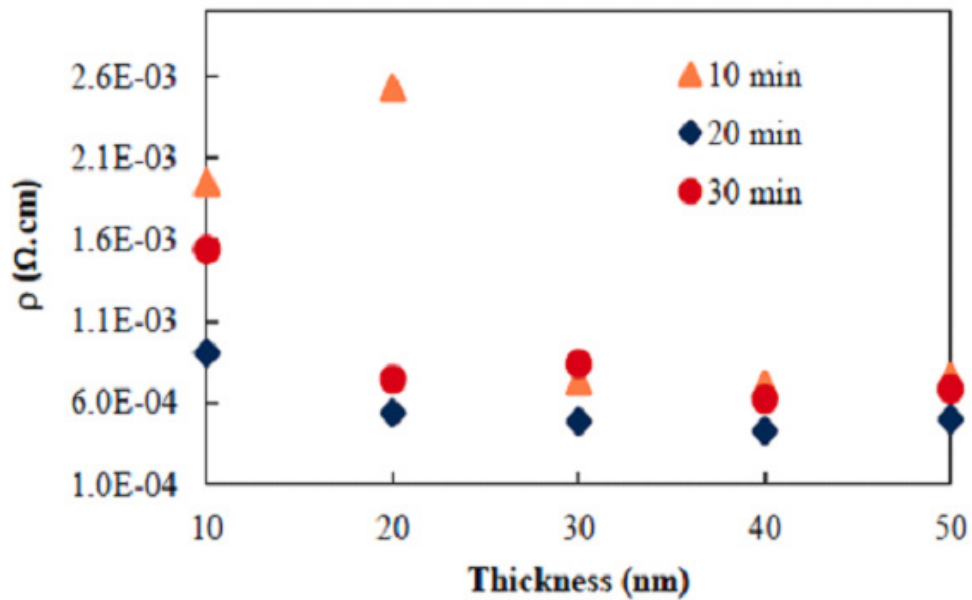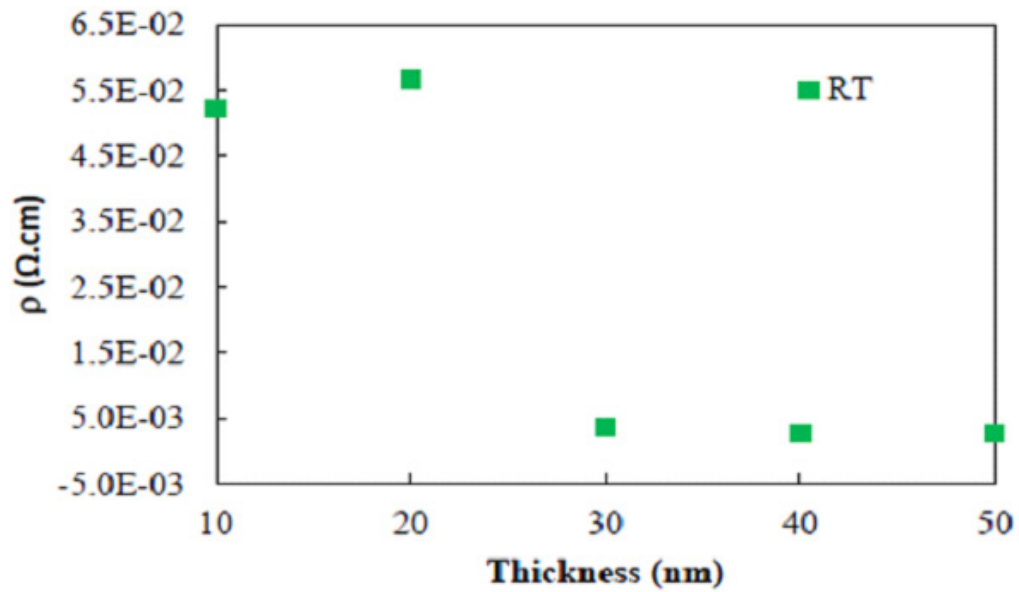
Figure 3.4. Variation of resistivity with ITO film thickness for; (a). As-deposited/ room temperature (RT), and (b). Annealed films for 10, 20, and 30 minutes.

3.5.3. Film morphology and roughness

3.5.3.1. Effect of substrate on ultra-thin ITO films

Fig. 3.5. shows results from SEM scans showing the surface morphology for both 10 nm and 20 nm as-deposited ITO films. Fig 3.5. (a), (b) and (c) show that the film surface is relatively smooth and predominantly amorphous in nature. Fig 3.5. (d) shows signs of grains development. The AFM analysis results are shown in Fig 3.6.
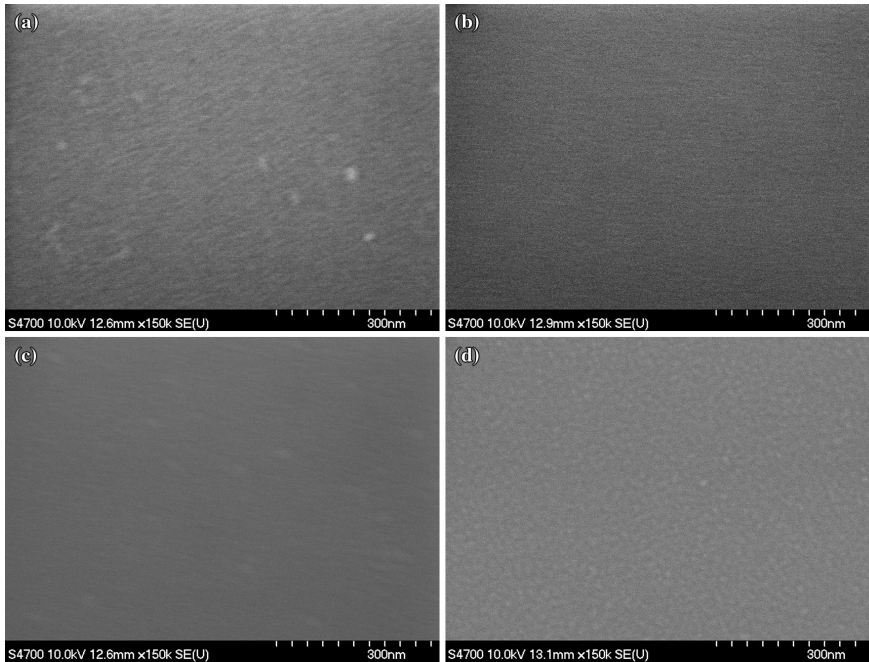
Figure 3.5. FESEM images for (a) 10 nm ITO on glass, (b) 10 nm ITO on silicon (with oxide spacer), (c) 20 nm ITO on glass and (d) 20 nm ITO on silicon (with oxide spacer).
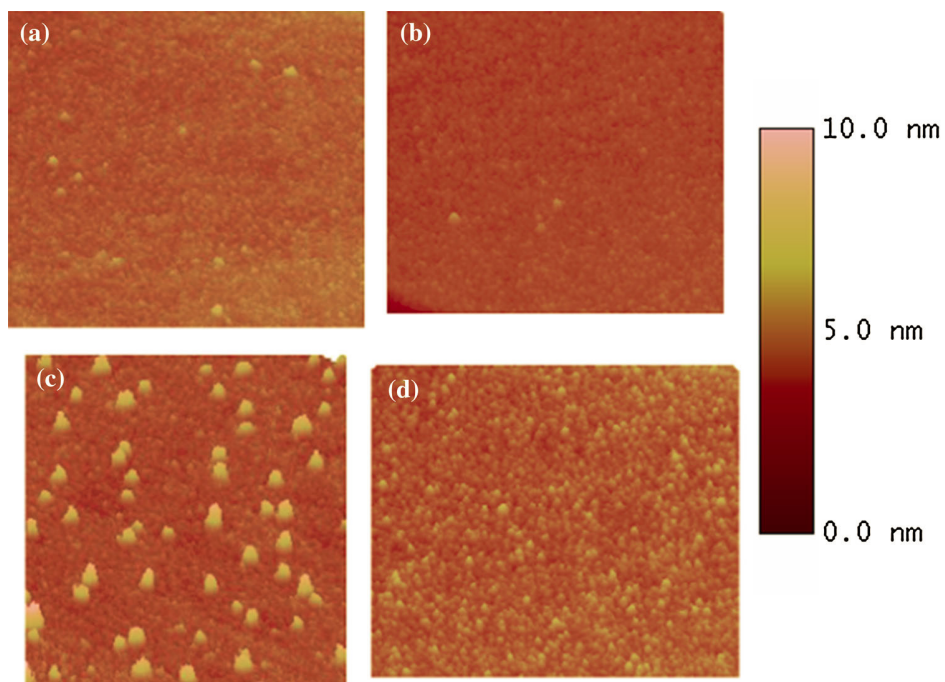
Figure 3.6. AFM images for as-deposited (a) 10 nm ITO on glass, (b) 10 nm ITO on silicon (with oxide spacer), (c) 20 nm ITO on glass and (d) 20 nm ITO on silicon (with oxide spacer). Image scale is 10 nm.

The results in Fig. 3.6 shows how mean roughness values of ITO varies with substrate type and are in agreement with the results shown in Fig. 3.5. It can be observed in these images that ITO tends to form uniform features on silicon with no evidence of defects. This is not the case with ITO on glass substrate which, despite having finer features (10 nm film) exhibit some larger defects. These defects seem to increase with the increase in film mean roughness and thickness. Despite the presence of a few dust particles on the sample surface, results confirmed that the sputtered films were of good quality. The AFM roughness results are summarized in Table 3.4.

Table 3.4. Summary of AFM results for as-deposited ITO films on glass and Si substrates.

Film	Roughness (nm)		Observations
	RMS roughness (Rq)	*Mean roughness (Ra)*	
ITO on Si wafer, 10 nm	0.44	0.35	Uniform, small features

ITO on Si wafer, 20 nm	0.58	0.45	Uniform features larger than 10 nm
ITO on glass, 10 nm	0.37	0.29	Very fine features with some larger defects
ITO on glass, 20 nm	0.83	0.52	Fine features with many large defects

3.5.3.2. Effect of annealing time on ultra-thin ITO films

When ultra-thin ITO films were subjected to post-processing treatment at 400 ^{0}C in a FG environment, different treatment times produced different effects. The as-deposited films mean roughness for this second batch of ITO samples were observed to vary between 0.67 nm and 0.85 nm. The 10 nm film had the smallest mean roughness value whilst the 20 nm film had the largest value. This may be due to the presence of surface defects features which seem to be more pronounced on the 20 nm film compared to all the other samples. Generally, all samples show a varying degree of dust particles presence and potential artifacts. Sections of the film samples which exhibited heavy dust particles (and any other contaminants) presence, striations and potential artifacts that were not consistent with other areas on the sample were excluded from the analysis.

The images show a sharp increase in the mean roughness for generally all films after 10 minutes of heat treatment. Whilst the film roughness is small for both the 10 nm and 20 nm films, it is observed to increase by a factor of two for the 30 nm to 50 nm film thickness samples. There is a trend for all films showing a decrease in mean roughness after 20 minutes of post-processing treatment with the 30 nm film showing the greatest decrease from approximately 1.9 nm to 1 nm. Evidently, annealing for 30 minutes results in a slight improvement in film roughness for the 30 nm to 50 nm range of film. However, the thinner films (10 nm and 20 nm) shows great deterioration in film mean roughness when annealed for longer periods of time (30 min or greater). This can be explained by the onset of islands on both of these films. Island formation is more pronounced on the quasi 2D 10 nm film resulting in the mean roughness increasing from the initial value of approximately 0.7 nm to 1.9 nm. The effects of annealing different ITO films in forming gas at 400

45

[0]C for 10, 20 and 30 minutes on films surface roughness are compared and summarized in Fig. 3.7.
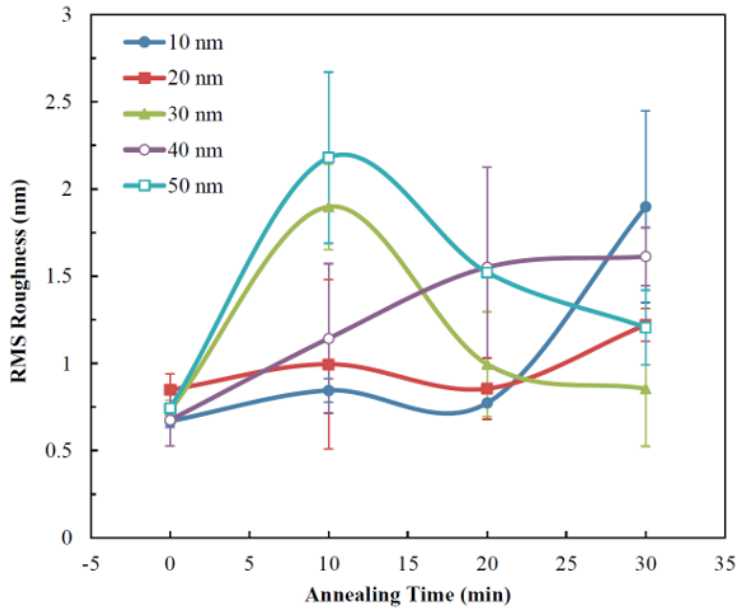
Figure 3.7. RMS roughness of annealed ITO films. The figure shows a time series with an overlap of error bars.

The detailed study on ITO showed some dependency of electrical properties and surface roughness with substrate type which is consistent with results from previous studies on slightly thicker films. Also ITO films on glass show a high degree of surface defects and finer amorphous-like features which may explain the high and oscillating values of sheet resistance on these films. Films grown on Si substrate have uniform, but large features. However, the same films have higher resistivity values. All samples, as-deposited and annealed, have a transmittance value greater than 80% with the as-deposited films being superior except for the 40 nm films for which the annealing for 20 minutes gives the best transmittance. Further analysis of samples show films annealed for 20 minutes generally have the lowest resistivity and lower roughness values.

Future work is needed to improve other TCOs such as AZO and ZnO and to engineer new high conductivity low loss materials for integration into plasmonic devices. AZO exhibited a transmittance superior to that of ITO while ZnO had the best sheet resistance among the three TCOs being compared. Further investigative work is needed to find the balance between films with useful resistivity and acceptable Ohmic losses in plasmonic-based PV devices. Future work should

focus on different processing techniques such as DC sputtering as well as exploring other post-processing environments.

3.6. Conclusions

Ultra-thin TCOs and in particular ITO presents a number of challenges for use as thin top contacts on plasmonic-enhanced PV devices. First, both ultra-thin TCO optical and electrical parameters differ greatly from those of thicker (bulk) films deposited under the same conditions. Secondly, they are delicate due to their thickness, requiring very long annealing times to prevent film cracking. The reactive gases (usually oxygen or hydrogen) require careful monitoring to avoid over-oxidizing or over-reducing the film as it impacts their stoichiometry. There is a trade-off between conductivity and transparency of the deposited films. The sub 50 nm TCO films investigated exhibited desirable optical properties (transmittance greater than 80%), which makes viable for plasmonic PV devices applications. However, all films evaluated here had resistivity values too high to be considered as materials for the top contact of conventional PV devices.

References

1. Shah, P. Torres, R. Tscharner, N. Wyrsch, H. Keppner, Photovoltaic technology: The case for thin-film solar cells. *Science*, *285*(5428) (1999), 692-698.

2. J. M. Pearce, Photovoltaics—a path to sustainable futures. *Futures*, *34*(7) (2002), 663-674.

3. V. Fthenakis, Sustainability of photovoltaics: The case for thin-film solar cells. *Renewable and Sustainable Energy Reviews*, *13*(9), (2009), 2746-2750.

4. T. Saga, Advances in crystalline silicon solar cell technology for industrial mass production. *NPG Asia Materials* 2(3), (2010), 96–102.

5. K. Branker, M. J. M.Pathak, J. M. Pearce, A review of solar photovoltaic levelized cost of electricity. *Renewable and Sustainable Energy Reviews*, *15*(9), (2011) 4470-4482.

6. M. A. Green, Thin-film solar cells: review of materials, technologies and commercial status. *Journal of Materials Science: Materials in Electronics*, *18*(1), (2007) 15-19.

7. J. Gwamuri, D. Ö. Güney, J. M. Pearce, Advances in Plasmonic Light Trapping in Thin-Film Solar Photovoltaic Devices, in: A. Tiwari, R. Boukherroub, M. Sharon) (eds), *Solar cell Nanotechnology,* John Wiley & Sons, Inc., Hoboken, NJ, USA. 2013, pp. 243–270.

8. A. Vora, J. Gwamuri, N. Pala, A. Kulkarni, J. M. Pearce, D. Ö. Güney, Exchanging Ohmic Losses in Metamaterial Absorbers with Useful Optical Absorption for Photovoltaics, *Scientific reports*, vol. 4, 2014.

9. T. Khaleque, R. Magnusson, Light management through guided-mode resonances in thin-film silicon solar cells, J. Nanophoton. 8(1), (2014) 083995–083995.

10. M.A. Green, Third Generation Photovoltaics: *Advanced Solar Energy Conversion* (Springer Series in Photonics), Springer, 2005.

11. H. A. Atwater, A. Polman, Plasmonics for improved photovoltaic devices, *Nat Mater*, vol. 9, no. 3, (2010) 205–213.

12. S. A. Maier, Plasmonics: *Fundamentals and Applications*. Springer, New York, 2007.

13. S. A. Maier, H. A. Atwater, Plasmonics: Localization and guiding of electromagnetic energy in metal/dielectric structures, *Journal of Applied Physics*, vol. 98, no. 1, (2005) 011101.

14. Kevin M. McPeak, Sriharsha V. Jayanti, Stephan J. P. Kress, Stefan Meyer, Stelio Iotti, Aurelio Rossinelli, and David J. Norris, Plasmonic Films Can Easily Be Better: Rules and Recipes, *ACS Photonics,* vol. *2* (3), (2015) 326 – 333

15. A. Vora, J. Gwamuri, J. M. Pearce, P. L. Bergstrom, D. Ö. Güney, Multi-resonant silver nano-disk patterned thin film hydrogenated amorphous silicon solar cells for Staebler-Wronski effect compensation, *Journal of Applied Physics*, vol. 116, no. 9, (2014) 093103.

16. K. Kulkarni, K. H. Schulz, T.-S. Lim, M. Khan, Electrical, optical and structural characteristics of indium-tin-oxide thin films deposited on glass and polymer substrates, *Thin Solid Films*, vol. 308, (1997) 1–7.

17. K. Kulkarni, K. H. Schulz, T. S. Lim, M. Khan, Dependence of the sheet resistance of indium-tin-oxide thin films on grain size and grain orientation

determined from X-ray diffraction techniques, *Thin solid films*, vol. 345, no. 2, (1999). 273–277.

18. J. W. Leem, J. S. Yu, Indium tin oxide subwavelength nanostructures with surface antireflection and superhydrophilicity for high-efficiency Si-based thin film solar cells, *Optics express*, vol. 20, no. 103, (2012) A431–A440.

19. Guillen, J. Herrero, Comparison study of ITO thin films deposited by sputtering at room temperature onto polymer and glass substrates, *Thin solid films*, vol. 480, (2005) 129–132.

20. J. George, C. S. Menon, Electrical and optical properties of electron beam evaporated ITO thin films, *Surface and Coatings Technology*, vol. 132, no. 1, (2000)45–48.

21. M. J. Alam, D. C. Cameron, Characterization of transparent conductive ITO thin films deposited on titanium dioxide film by a sol–gel process, *Surface and Coatings Technology*, vol. 142, (2001) 776–780.

22. Houng, A. Wang, Characterization of indium tin oxide films by RF-assisted DC magnetron sputtering, *Applied Surface Science*, vol. 258, no. 15, (2012) 5593–5598.

23. Thestrup, J. Schou, A. Nordskov, N. B. Larsen,"Electrical and optical properties of thin indium tin oxide films produced by pulsed laser ablation in oxygen or rare gas atmospheres, *Applied surface science*, vol. 142, no. 1, (1999) 248–252.

24. Terzini, P. Thilakan, C. Minarini, Properties of ITO thin films deposited by RF magnetron sputtering at elevated substrate temperature, *Materials Science and Engineering: B*, vol. 77, no. 1, (2000)110–114,.

25. A. Sytchkova, D. Zola, L. R. Bailey, B. Mackenzie, G. Proudfoot, M. Tian, A. Ulyashin, Depth dependent properties of ITO thin films grown by pulsed DC sputtering, *Materials Science and Engineering: B*, vol. 178, no. 9, (2013) 586–592.

26. L. Cruz, C. Legnani, I. Matoso, C. Ferreira, H. Moutinho, Influence of pressure and annealing on the microstructural and electro-optical properties of RF magnetron sputtered ITO thin films. Materials Research Bulletin 39, (2004) 993–1003.

27. J. Chen, X. W. Sun, B. K. Tay, Fabrication of ITO thin films by filtered cathodic vacuum arc deposition, *Materials Science and Engineering: B*, vol. 106, no. 3, (2004) 300–304.

28. K.-S. Tseng, Y.-L. Lo, Effect of sputtering parameters on optical and electrical properties of ITO films on PET substrates, *Applied Surface Science*, vol. 285 (2013)157–166.

29. D.-H. Kim, M.-R. Park, H.-J. Lee, G.-H. Lee, Thickness dependence of electrical properties of ITO film deposited on a plastic substrate by RF magnetron sputtering, *Applied Surface Science*, vol. 253, no. 2, (2006) 409–411.

30. U. Betz, M. K. Olsson, J. Marthy, M. F. Escolá, On the synthesis of ultra smooth ITO thin films by conventional direct current magnetron sputtering, *Thin Solid Films*, vol. 516, no. 7 (2008) 1334–1340.

31. R. B. H. Tahar, T. Ban, Y. Ohya, Y. Takahashi, Tin doped indium oxide thin films: Electrical properties, *Journal of Applied Physics*, vol. 83, no. 5, (1998) 2631–2645.

32. Perkin-Elmer RF Sputtering System-6 Inch protocol: MOST: Available: http://www.appropedia.org/Perkin-Elmer_RF_Sputtering_System-6_Inch_protocol:_MOST

33. S.A. Knickerbocker, Ph.D. Dissertation, Michigan Technological University, 1995.

34. T.S. Lim, M.S. Thesis, Michigan Technological University, 1997

35. University of Toledo, PVIC material deposition: RF/DC Magnetron Sputtering Utility System. Available: http://www.utoledo.edu/research/pvic/material_deposition.html.

4. A New Method of Preparing Highly Conductive Ultra-Thin Indium Tin Oxide for Plasmonic Enhanced Thin Film Solar Photovoltaic Devices[3].

4.1. Introduction

To increase the efficiency of solar photovoltaic (PV) cells while reducing costs, several light management schemes have been proposed and investigated, such as metal nano-particles, nanowires, and plasmonic metallic nanostructures (metal–insulator–metal (MIM)/insulator–metal–insulator (IMI)) [1], [2], [3], [4], [5], [6] and [7]. The lowest cost per unit power can be obtained with thin film hydrogenated amorphous silicon (a-Si:H) PV[8]. Although a-Si:H is a thin film material with a direct mobility gap, the Staebler–Wronski effect or light induced degradation effectively limits the intrinsic layer thickness [9], [10],[11], [12] and [13]. Thus, historically light trapping was first applied to a-Si:H [14] and [15]and remains important today to improve device performance. Modeling studies of plasmonic metallic nanostructures have shown great potential as a light management scheme in thin-film nanodisc-patterned a-Si:H solar cells [16]. Their ability to sustain coherent electronic oscillations leading to electromagnetic field coupling and confinement [17] has made plasmonic enhancement an area with very high prospects for light harvesting in PV devices [18] and [19]. A number of technical and fabrication related issues act as a barrier to the full realization of plasmonic based commercial grade PV devices. Parasitic optical absorption (ohmic losses) in the metallic structure and high carrier recombination near the metal–semiconductor interfaces remain significant challenges [16], [20], [21] and [22].

The most prominent fabrication challenge is the complication of scalable and economically viable techniques for controlled nanostructure patterning. The fact that plasmonic resonances are highly dependent on both shape and geometry of nanostructures [23] means that design parameters should be highly controlled throughout the fabrication process. Another design challenge for plasmonic enhanced PV devices, such as the one proposed by Vora et al. [16], is the

---

[3] "The materials contained in this chapter is previously published in *Solar Energy Materials and Solar Cells.*"

requirement for ultra-thin transparent conducting oxides (TCOs) with high transmittance (low loss) and low enough resistivity to be used as device top contacts/electrodes [20]. Most work on TCOs is on relatively thick layers [24] and the few reported cases of thin TCO showed a marked decrease in conductivity [25]. Recent work on ultra-thin TCOs (aluminum-doped zinc oxide (AZO), indium-doped tin oxide (ITO) and zinc oxide (ZnO)) [20] revealed an unavoidable trade-off between the transmittance and resistivity and the challenge to strike a balance between optical and electrical parameters of different TCOs when fabricated with conventional growth methods. Ultra-thin films showed a tendency to be both amorphous and continuous or as isolated islands, which explained the observed poor electrical properties. Improving the electrical properties of these films through annealing proved ineffective since the delicate thin films would nucleate to form grain clusters.

In order to overcome this challenge, this study investigates a novel method of producing continuous ultra-thin (<40 nm) TCOs. First ~80 nm ITO films are sputtered in various argon–oxygen atmospheres and annealed to increase conductivity. These films were then characterized optically and electrically. The most promising materials were then reduced in thickness with a well-controlled low-cost chemical etching process to reach the desired thickness. The degradation in the electrical conductivity was tracked as a function of thickness.

4.2. Material and methods

This study focus was on achieving thinner ITO films (<40 nm) with optimal optical and electrical properties to be used both as a buffer layer and as the top contact for the solar cell structure proposed by [16] and is shown in Fig. 1. Film processing was done by RF sputter deposition techniques (Perkin-Elmer Model 2400) [26] and [27]. The approach used was to grow films with a targeted thickness of 80 nm and then reduce the thickness to <40 nm. Thin films were grown on (100) prime silicon substrates with a 98 nm thermally grown oxide, and on glass substrates using a 99.99% 100 mm diameter pressed ITO (Sn_2O:In_2O_3 10:90 wt%) target. Substrates were ultrasonically cleaned in isopropanol for 15 min followed by another 15 min in DI water (17.2 MΩ-cm) before they were dried using N_2. The sputtering chamber was initiated to a low 10^{-7} Torr base pressure to minimize

ambient condition impact on the resulting films. The sputtering process pressure was maintained at 7.5×10^{-3} Torr. The distance between the target and substrates was kept constant. As a standard procedure, the target was pre-sputter cleaned at a power of 150 W, whereas the sputter deposition of the films was performed at 100 W. The argon gas flow was maintained at approximately 10 sccm to attain the targeted processing pressure, and the oxygen gas flow was varied as listed in the Table 1. The sputter deposition rate was estimated to be in the range of 8–12 nm per minute, depending upon the oxygen flow rate.
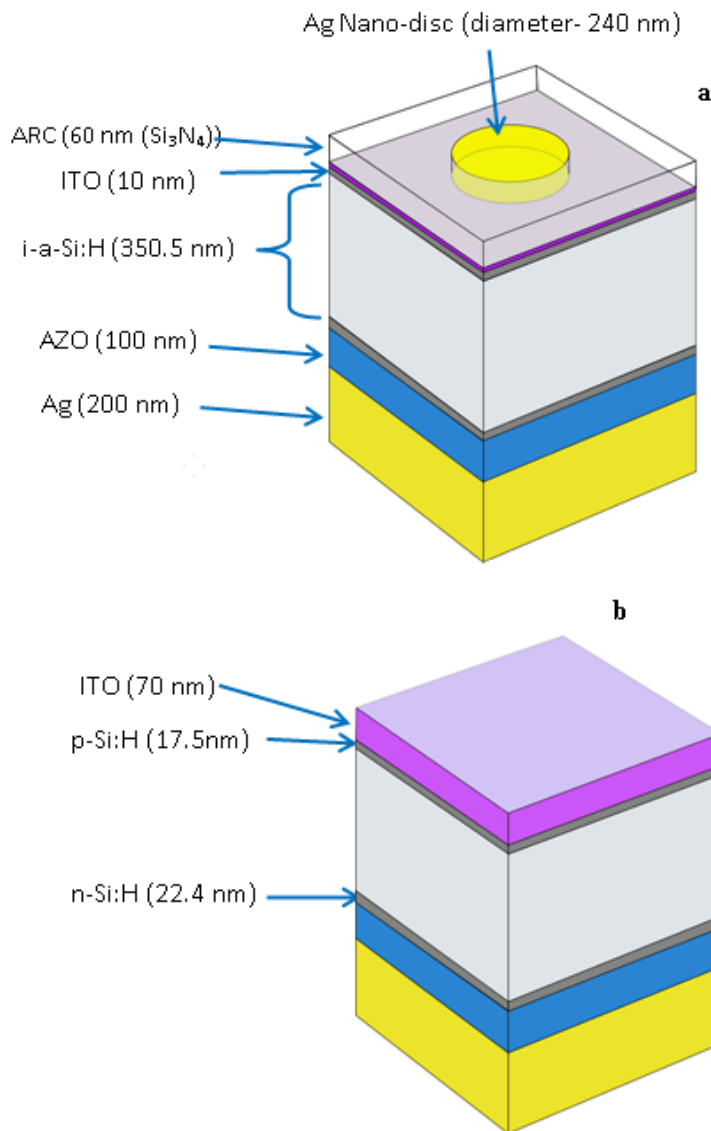
Figure 4.1. (a). Plasmonic solar cell structure, and (b). Reference cell. ARC refers to anti-reflecting coating.

Table 4.1. Summary of ITO processing parameters.

Sample ID	RF (W)	Gas ratio (Ar:O$_2$)	Film Thickness (nm)	Resistivity (Ω.cm)		Average transmittance (400 -800nm)	
				As - deposited	Annealed at 300 ^{0}C (30min)	As - deposited	Annealed at 300 ^{0}C (30min)
A1	100	10:0	98	1.6E-02	8.8E-04	60	70
A2	100	10:0.2	85	5.0E-03	5.5E-04	72	79
A3	100	10:0.3	78	1.8E-03	5.7E-04	65	71
A4	100	10:0.4	87	2.4E-03	8.0E-04	85	91
A5	100	10:0.5	89	6.7E-03	1.6E-03	84	88
A6	100	10:0.7	64	4.3E-02	1.7E-02	86	92
A7	100	10:1.0	63	4.7E-01	5.2E-02	86	94

Processed samples were cleaved and one part was annealed at 300 °C for 30 min in air to increase the crystallinity following the success of various reports [24] and [25]. Both as-deposited and annealed sample sets were then optically and electrically characterized to determine sample thicknesses, optical constants n and k, and sheet resistance (to obtain the resistivity). The optical properties were obtained using variable angle spectroscopic ellipsometry (VASE) (J.A Woollam Co UV–vis V-VASE with control module VB-400). Electrical characterization was performed using a four point probe system consisting of ITO optimized tips with 500 μm tip radii set to 60 g pressure and an RM3000 test unit from Jandel Engineering Limited, UK. In addition, structural properties for the selected films of lower sheet resistance and higher optical properties were investigated by X-ray diffraction (XRD) (Scintag 2000). The XRD were done for both the as-deposited and annealed ITO samples deposited on glass substrates.

The resistivity and transmittance measurements were also performed on samples deposited on glass, whereas the thicknesses were measured from the Si/SiO$_2$/ITO samples. Films with the transmittance values greater than 75% and resistivity values within the 10^{-4} Ω-cm range after annealing were selected for further processing. From Table 1, samples A2 (both on glass and Si/SiO$_2$) were subjected to the etching process using a standard chemical etchant for etching ITO. A

mixture of HCl:HNO$_3$:H$_2$O (1:1:5) volume ratio [28] was prepared and used for etching sample A2. All the etching was performed at room temperature, resulting in a slow and controlled etch rate for the Si/SiO$_2$ films. Etched samples were then thoroughly rinsed in DI water before they were dried in N$_2$ and subjected to optical and electrical characterization. The etch times were varied and the process repeated with a subsequent optical and electrical measurements between each etch. The surface morphology of the sample A2, as deposited, annealed and after etching were also investigated using an atomic force microscopy (Veeco Dimension 3000).

4.3. Theory/calculation

The complex relative permittivity (of the form $\varepsilon_r = \varepsilon' - j\varepsilon''$) of p-a-Si:H, i-a-Si:H, n-a-Si:H, and aluminum doped zinc oxide (AZO) of an a-Si:H solar cell (fabricated by ThinSilicon, Mountain View, CA) (Fig. 4.1) were measured using a J.A. Woollam variable-angle spectroscopic ellipsometer. The complex relative permittivity of both silver and silicon nitride (Si$_3$N$_4$) were taken from Palik [29] and the ITO optical properties were obtained from characterization of locally processed/optimized samples. The optical responses of the nano-disk patterned solar cell (NDPSC) was calculated through a fully-vectorial finite element based software package COMSOL Multiphysics RF module v5.0 in frequency domain. The NDPSC solar cell structure [16] was simulated using periodic boundaries for the vertical sides and excitation and output ports were used above and below the suspended air of the unit cell respectively. The absorbance in the i-a-Si:H layer was calculated from the power loss density function in COMSOL, which in turn was used to calculate theoretical absorbed power density in the i-a-Si:H layer of NDPSC and the reference using MATLAB r2013b as described by Vora et al. [16] for the incident AM 1.5 reference solar spectrum using the equation:

$$P_{i-a-Si:H} = \int A(\lambda) E_{AM1.5}(\lambda) d\lambda \qquad (4.1)$$

where $P_{i-a-Si:H}$ is the absorbed power density (W/m^2) in the i-a-Si:H layer, $A(\lambda)$ is the absorbance in i-a-Si:H layer as a function of wavelength, and $E_{AM1.5}(\lambda)$ is the spectral irradiance as a function of wavelength (obtained from NREL [30]. The optical enhancement (OE) is calculated using the equation:

$$OE = (P_{i-a-Si:H(NDPSC)}/P_{i-a-Si:H(Ref)} - 1) \times 100 \qquad (4.2)$$

where the subscript 'NDPSC' and 'Ref' denote NDPSC and reference cell, respectively.

4.4. Results

4.4.1. Electrical and optical characterization

The resistivity in Ω-cm for the as-deposited and annealed samples after 30 min at 300 °C are summarized in Table 4.1. The as-deposited values are presented here only for comparison purposes. As is observed in Table 4.1, sample A2 has the lowest resistivity value of 5.5×10^{-4} Ω-cm and a fairly high average transmittance of 79% for the annealed samples, hence it was chosen for further processing. The transmittance is expected to improve as the film thickness is decreased through etching whilst the resistivity is expected to show an inverse variation with thickness for the same film sample (A2).

Fig. 4.2(a) and (b) depicts the resistivity and transmittance versus the oxygen flow rate of the selected samples deposited on glass substrates. The effect of oxygen content on the resistivity of sputter deposited films is well documented [24] and 25. Accordingly, each sputter deposition system varies in its optimal range of process gas composition. In the system used for this study, it was found that the lowest resistivity 1.79×10^{-03} Ω-cm is obtained for the as-deposited samples processed with an oxygen flow rate of 0.3 sccm. Relatively, the as-deposited films without oxygen and with other flow rates show an order of magnitude difference in resistivity. Optical measurements show that an oxygen flow of 0.4–0.5 sccm gives as-deposited samples films with higher transmittance of about 85% in the visible wavelength range (400–800 nm).
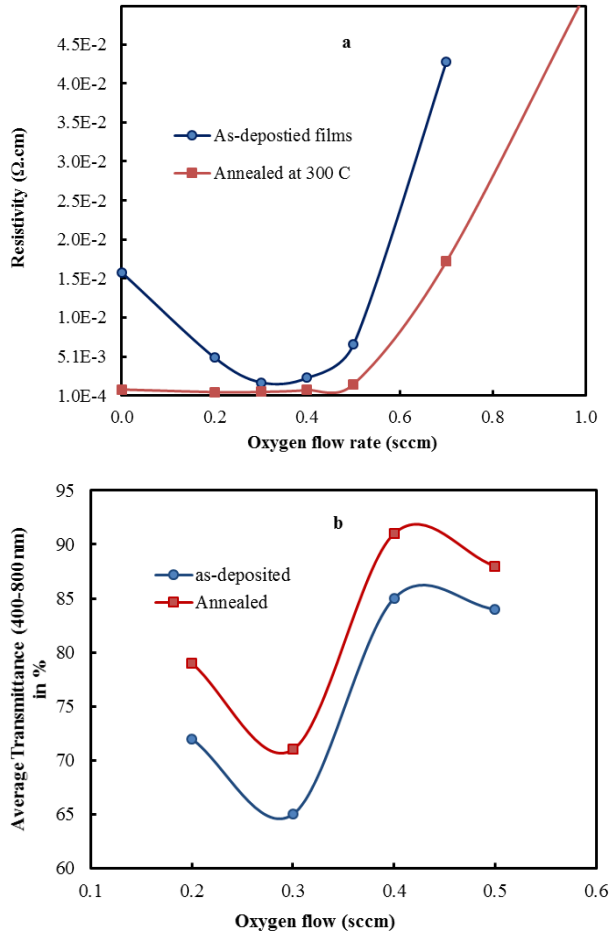
Figure 4.2. (a) Resistivity and (b) transmittance of as-deposited and annealed films as a function of oxygen flow rate. Annealing temperature was 300 °C.

Post processing annealing of samples in air at 300 °C for 30 min results in a substantial improvement in the resistivity and the transmittance as shown in the Table 4.1. The lowest resistivity values are obtained for the cases of 0.2 and 0.3 sccm oxygen flow and were recorded at 5.5×10^{-4} and 5.7×10^{-4} Ω cm, respectively. The average transmittance for the same samples in the 400–800 nm wavelength range showed ~10% difference and 0.2 sccm gave samples with a better transmittance than those deposited with oxygen flow rates of 0.3 and 0 sccm. It was observed that films processed at higher oxygen flow rates (0.4 and 0.5 sccm) showed about 90% transmittance. However, these same samples had a higher resistivity compared to the other samples and therefore are not appropriate for use as top contact for the proposed high efficiency plasmonic based a-Si:H PV device.

4.4.2. XRD analysis

XRD spectra for the as-deposited and annealed sample sets with various oxygen flow deposited on glass is illustrated in Fig. 4.3. (a) and (b). The raw data was corrected for base line using the Origin software. The data was smoothened before it was presented for analysis. The results indicate that the as-deposited films show a polycrystalline nature with some amorphous tendency. For all conditions, the (222) peak is pronounced and clearly defined, whereas the (400) and (441) peaks were not present for the as-deposited film with 0.2 sccm oxygen, but it is clearly present for the other deposition cases. The annealed samples show the presence of the (222), (400), and (441) peaks, and a weak (622) peak for the case of films deposited with 0.2 to 0.5 sccm oxygen. More details such as lattice constants, d-spacing and grain size that are extracted from the XRD are summarized in Table 4.2. It is well known that ITO deposited with the Ar+O_2 composition will have the preferred orientation of (222) and (400) [24].
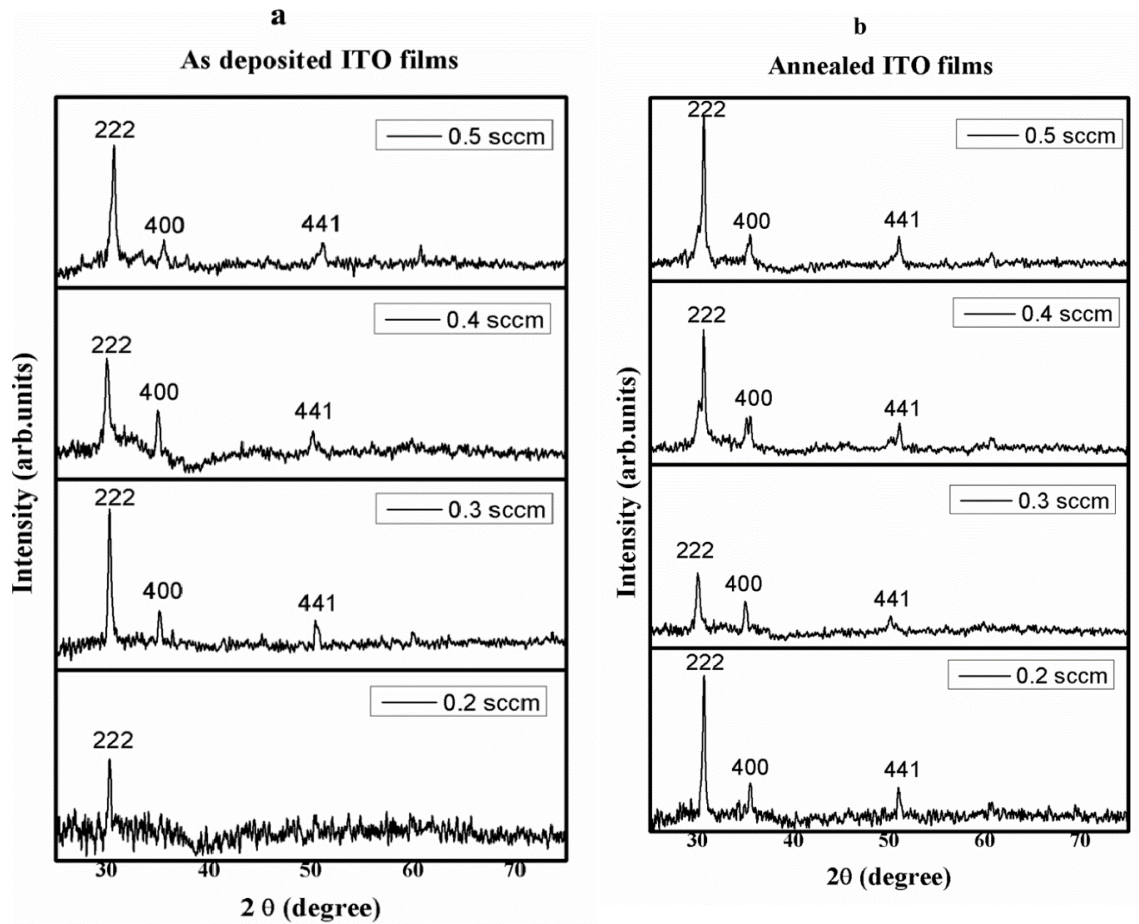
Figure 4.3. XRD analysis of selected (a) as-deposited and (b) annealed ITO film for various oxygen flow.

The intensity ratios (I_{222}/I_{400}), for the materials with various oxygen flow and annealing has the values of 1.93–4.68 as listed in Table 4.2 and shown in Fig. 4.4. The figure clearly indicates the large variation in the intensity ratio and thus the microstructure. The estimated grain size for the lowest oxygen flow cases was observed to increase for the annealed samples whilst for the other cases, the grain size decreased after annealing. Worth noting is the case for the 0.3 sccm sample, where the grain size drastically decreased after annealing (Table 4.2). By comparing the results with the intensity ratio of standard indium oxide (3.33), the high and low intensity ratios were observed for all of the materials.

Table 4.2. Summary of XRD analysis of selected ITO film samples.

Sample code	d spacing (Å)		Lattice constant (Å)		I_{222}/I_{400}	Grain size (nm)
	222	400	222	400		
Standard	2.921	2.529	10.118	....	3.33	....
0.2	2.872	2.552	11.486	10.207	....	22
0.2A	2.921	2.531	11.685	10.124	3.99	30
0.3	2.951	2.551	11.804	10.205	3.69	23
0.3A	2.974	2.562	11.898	10.249	1.93	14
0.4	2.919	2.528	11.67	10.113	2.1	26
0.4A	2.936	2.556	11.746	10.226	3.58	26
0.5	2.915	2.524	11.66	10.09	4.52	24
0.5A	2.920	2.535	11.676	10.113	4.68	20
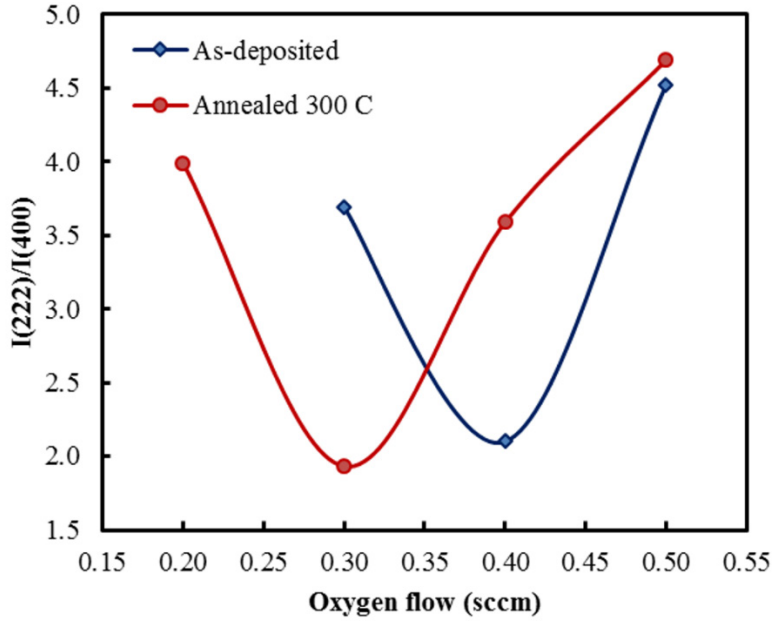
Figure 4.4. XRD analysis of selected as-deposited and annealed ITO film for various oxygen flow.

4.4.3. Chemical shaving: cyclic wet chemical etching

In this study, the samples with 0.2 sccm (A2 in Table 4.1) were used for the etching. The sample were etched at various times in the prepared etchant for several cycles and measured for the resistivity and thickness between each cycle. The obtained results are summarized inTable 4.3. Fig. 4.5(a) and (b) represents the etching time versus thicknesses and thickness versus resistivity for the measured sample. The samples were etched from 85 nm to 36 nm in 7 cycles with varying etching times. The variation in the resistivity corresponding to the remaining thickness were monitored and listed in Table 4.3. As the thickness of the film decreases the resistivity increases, but for the cycles etched we found that the resistivity is still in the order of 10^{-4} Ω cm. Chemical shaving was stopped after achieving a 36 nm film since this film showed desirable electrical properties and managing thinner films was going to be a challenge.

Table 4.3. Etching time and the measured thickness and electrical properties.

Etching time	Film Thickness (nm)	Sheet resistance Ω/Sq	Resistivity (Ω.cm)
0	85	70	5.6×10^{-4}
30	81	66	5.4×10^{-4}
60	78	68	5.3×10^{-4}
240	63	95	6.0×10^{-4}
360	54	105	5.7×10^{-4}
510	44	154	6.8×10^{-4}
660	36	250	9.0×10^{-4}
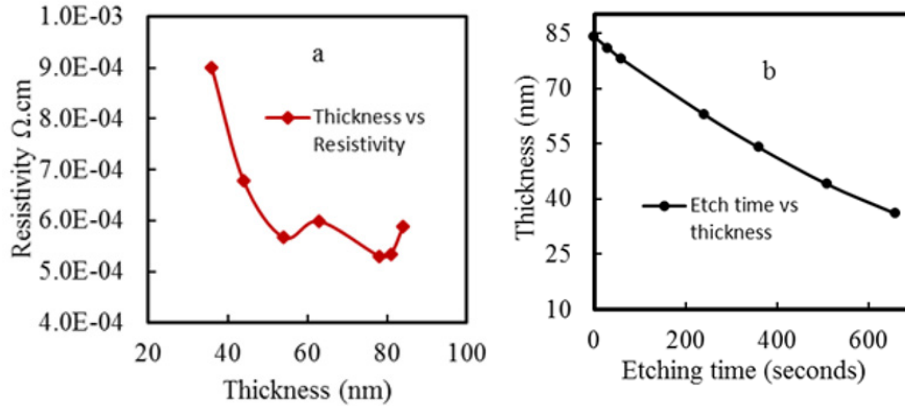
Figure 4.5. Variation of (a) sheet resistance with film thickness for ITO (A2) films; (b) annealed ITO film (A2) thickness with etch time.

4.4.3.1. AFM analysis

The AFM analysis showed that the etching process was quite uniform throughout the etched samples. There was no visible change in grain size with etching indicating that the annealed films were homogeneously micro-crystalline in nature with no evidence of an amorphous layer.

Fig. 4.6(a) shows the AFM images of the ITO sputtered film on silicon with oxide layer with different process as described in the Roughness values were taken from the area of 3000×3000 nm^2 and shown in Fig. 4.6(e). As can be seen in Fig. 4.6 there was a change in the surface morphology of the samples before and after etching. The root means square (rms) surface roughness of 2.4, 2.7 and 8.5 nm for the as-deposited and annealed, 30 s and 660 s etched samples was observed respectively.
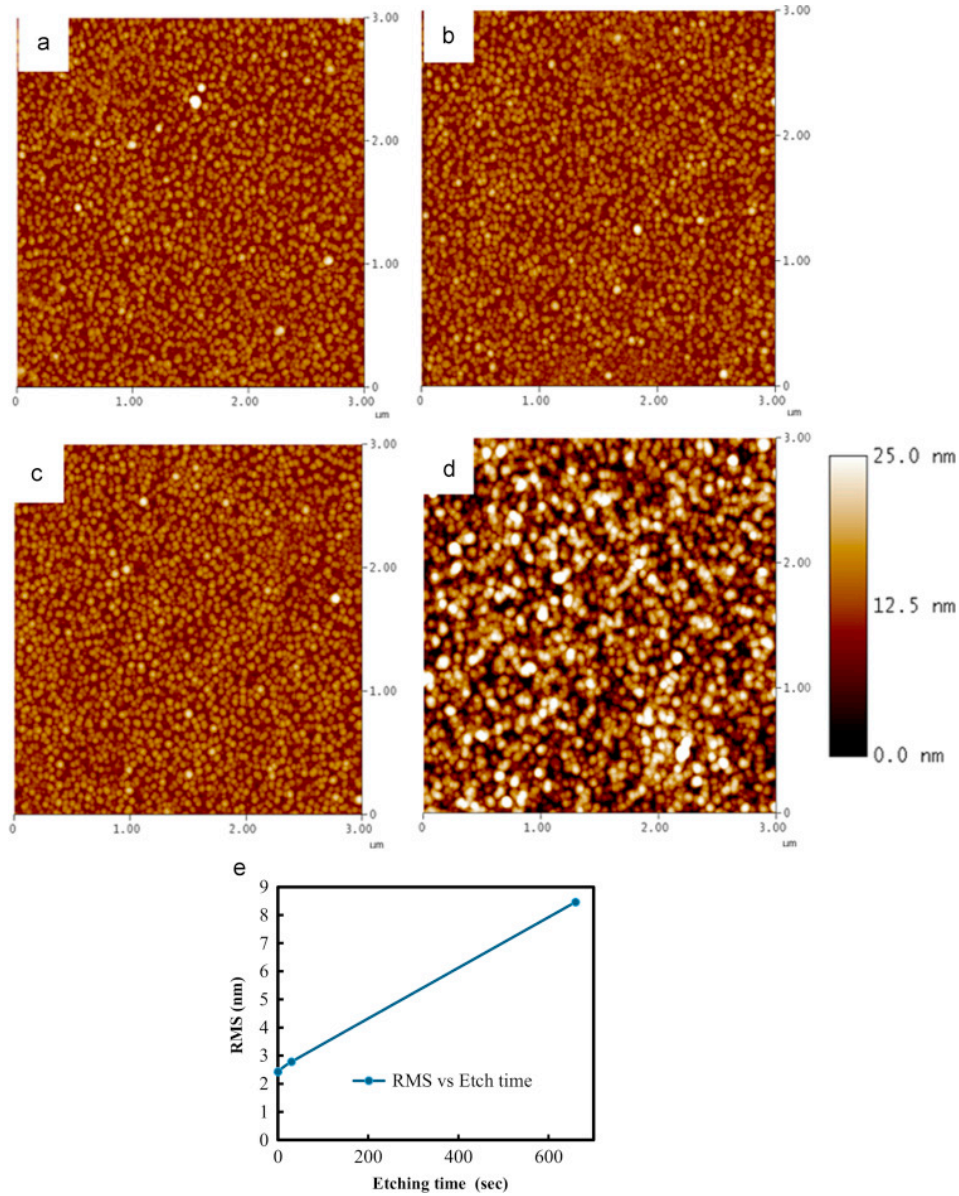
Figure 4.6. Shows the AFM images of the ITO sputtered film on silicon with oxide layer (a), annealed at 300 °C for 30 min (b), annealed film etched for 30 s (c) etched for 60 s (d) etched for 660 s and (e) illustration of etching time (s) vs. roughness in nm.

4.4.3.2. Optical inspection

Fig. 4.7 depicts the optical microscope image of the ITO surface for the as deposited (a) and for the annealed and etched films (b), respectively. The optical microscope inspection of the ITO surface of the as-deposited film on the Si/SiO$_2$ (98 nm) substrates shows a smooth surface with some defects locally that may be due to the substrate. The initial Si substrate had a 98 nm film of SiO$_2$ (blue in color) was sputtered with an ITO film of about ~80 nm. Thus, Fig. 4.7(a) shows a reflection of greenish in color, after the film is etched down to about 35 nm, the film becomes transparent enough for the bluish color of SiO$_2$ layer below to be visible. The color uniformity can be directly correlated to the film uniformity as already confirmed from the AFM characterization.
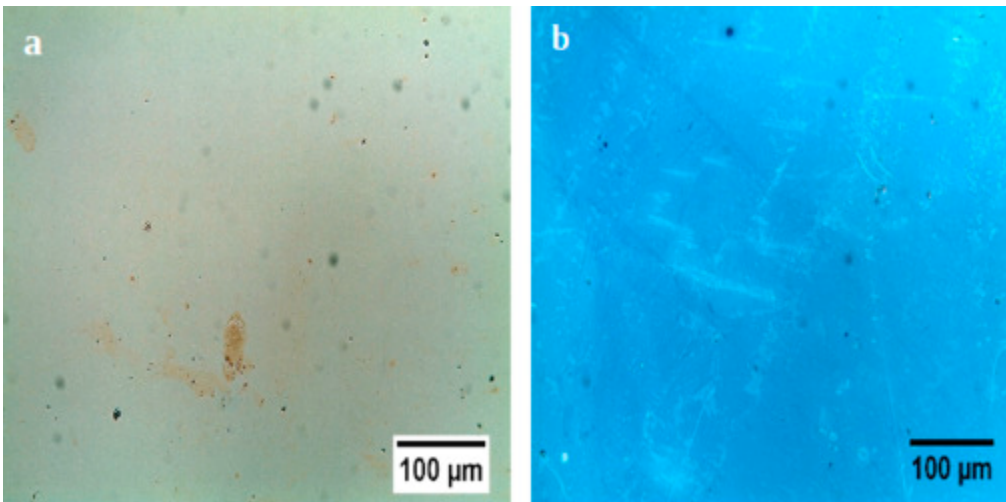
Figure 4.7. Optical microscope image on the surface of as-deposited (a) and etched for 660 s and (b) ITO thin films on the Si/SiO2 substrate.

4.4.4. Optical simulation

The optical simulation results are discussed below. Simulations for absorbance in the *i*-a-Si:H were carried out for the solar cell with device structure as shown in Fig. 4.1a and b. Optical parameters used in the simulation were obtained from subsequent chemical shaving cycles and fed into an optimized model to study the enhancement behavior of the device. The ITO layer was systematically increased from 36 nm to 81 nm for all film thicknesses shown in Table 4.3 without changing the underlying parameters of other layers and nano-disk. The absorbance and the absorbed power density in the *i*-a-Si:H layer was recorded for each measured thickness as seen in Fig.4. 8.
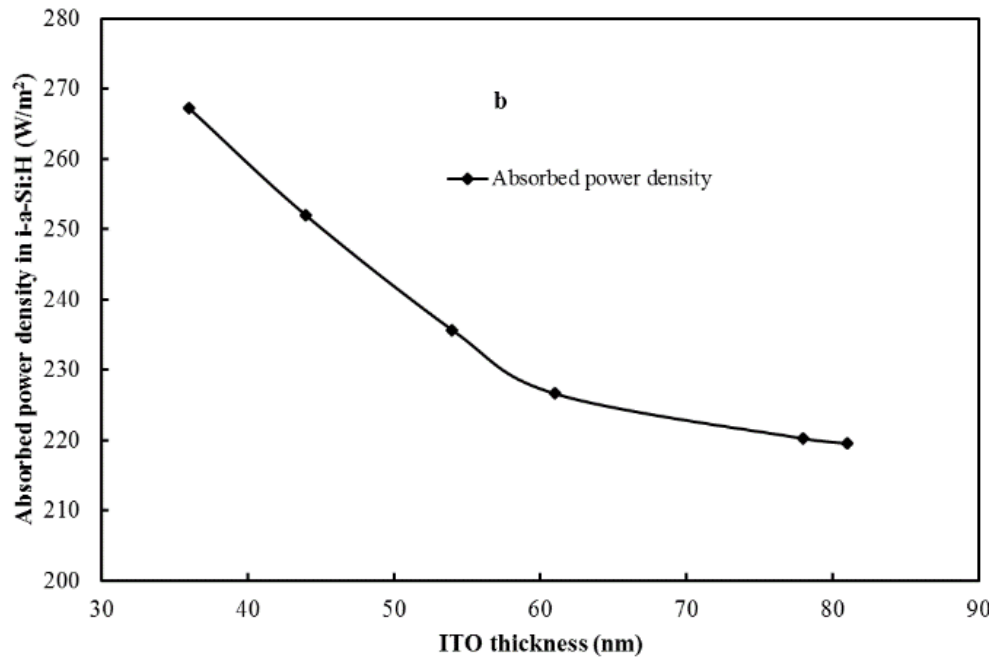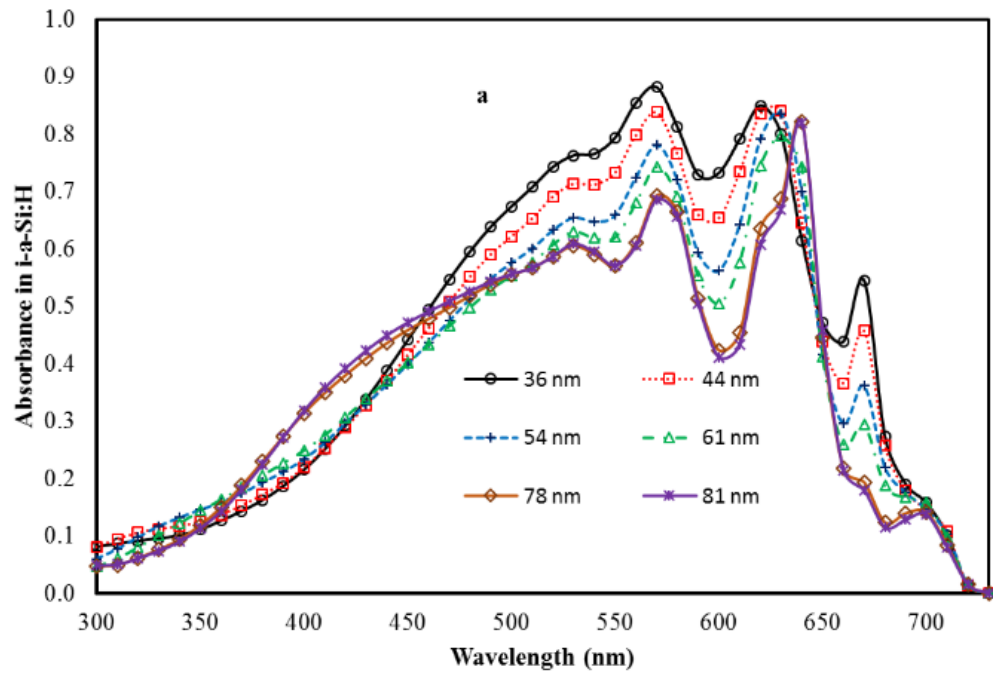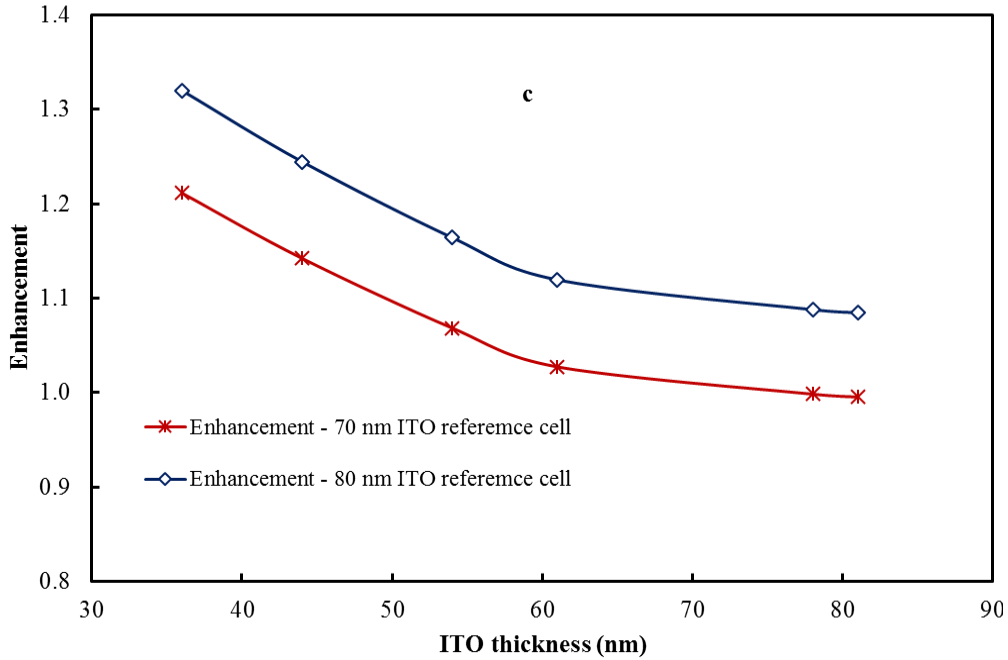
Figure 4.8. Numerical simulation results of a-Si:H PV devices. (a) Variation of absorbance with ITO layer thickness for the 300–730 nm wavelengths, (b) variation of absorbed power density in i-a-Si:H (W/m2 with ITO thickness and, (c)dependence of optical enhancement in the a-Si:H solar cell on ITO spacer thickness for 70 and 80 nm reference solar cell structures. Both reference cells have no nano-disc plasmonic structure (**Fig. 4.1.**(b)).

Results from simulation for absorbance in a solar cell with ITO spacer layer for thickness ranging from 36 to 81 nm are shown in Fig. 4.8.(a). The effect of ITO layer thickness on the absorbed solar radiation in the 300–730 nm spectral range is evident and the 36 nm thick ITO film offers the best overall enhancement. Fig.4.8.(b) shows the dependence of absorbed power density in *i*-a-Si:H on ITO thickness. Absorption is highest (~270 W/m^2) when the ITO layer between the plasmonic nano-disks and the *p*-a-Si:H is thinnest (36 nm) and lowest (220 W/m^2) for 81 nm ITO. Fig. 4.8.(c) shows how optical enhancement in *i*-a-Si:H varies with ITO layer thickness for two reference cells; one with ITO top layer of 70 nm and the other with 80 nm. Both reference cells have no nano-disc plasmonic structure (Fig. 4.1.(b)).

4.5. Discussion

Simulation results show a theoretical enhancement of 21% from the proposed cell structure (Fig. 4.1) with the locally fabricated and optimized 36 nm ITO film. These

results provide a clear opportunity for improving a-Si:H PV efficiency and should be pursued for future work. Electrical characterization confirms a clear dependence of sheet resistance on the reactive gas composition as shown in Fig. 4.2. There is a marked increase in sheet resistance as the oxygen concentration increases for the as-deposited films. However, annealing the films in air for 30 min results in a large decrease in the sheet resistance for the 0.3 and 0.4 sccm oxygen gas flow rates. Evidently, the annealed films are more crystalline in nature unlike the as-deposited films, which exhibit a predominantly amorphous microstructure. AFM images are also presented to compliment the XRD results. As has been previously reported, annealing improves film homogeneity as it provides sufficient energy to allow the Sn atoms to diffuse into the indium oxide matrix. This has the effect of decreasing the overall lattice disorder resulting in an increase in carrier mobility [31].

These observed diffraction lines agree with cubic bixbyite indium oxide structure JCPDS card no: 06-0416 and la-3 space group (Number: 206). Impurity of Sn phases is not observed in the XRD spectrum in the deposited and annealed films. It is evident from these results that the Sn atoms occupy the substitution sites of the indium atoms. In general, the intensities ratio was responsible for the combination of In^{3+} and O^{2-} ions in the ITO films [24]. This type of pairing enhances the indium oxide network formation and maintains the periodicity of the indium oxide. A critical level of In^{3+} and O^{2-} pairs are required for the formation of these networks. Below the critical level, defects in the indium oxide films will result. Hence the peak intensities of the films are greatly influenced by these combinations as reflected in the XRD spectra in Fig. 3. ITO films with thicknesses greater than 100 nm, have been well studied and documented [32] and [33]. However, their properties cannot be extrapolated to films of thickness 90 nm and below due to significant and unpredicted microstructures associated with these ultra-thin films [20].

4.6. Conclusions

Cyclic wet chemical etching performed at room temperature was used to thin ITO films from 81 nm down to 36 nm. The films were characterized at the end of each cycle for electrical and optical properties. The sheet resistance of the thinnest film (36 nm) was observed to be on the same order as much thicker commercial ITO films currently utilized as transparent electrodes in PV and other opto-electronic

devices. Optical properties of the shaved films were used in an optimized model to predict the optical enhancement of nano-disc plasmonic a-Si:H solar cells. Simulations indicate that optical enhancement greater than 21% are possible in the 300–730 nm wavelength range when compared to the reference cell. Using the novel chemical shaving method described here, high-quality ultra-thin ITO films capable of improving the efficiency of thin film a-Si:H solar cells have been demonstrated. The methods employed in the optimization process are well established and economically viable, which provide the technical potential for commercialization of plasmonic based solar cells.

References

1. J. Gwamuri, D.O. Guney, J.M. Pearce. Advances in Plasmonic Light Trapping in Thin-Film Solar Photovoltaic Devices, Solar cell nanotechnology. John Wiley & Sons, Inc., Hoboken, NJ, USA (2013), pp. 241–269

2. J. Trevino, C. Forestiere, G. Di Martino, S. Yerci, F. Priolo, L. Dal Negro. Plasmonic-photonic arrays with aperiodic spiral order for ultra-thin film solar cells. Opt. Express, 20 (2012), p. 418

3. K. Aydin, V.E. Ferry, R.M. Briggs, H.A. Atwater. Broadband, polarization-independent resonant light absorption using ultrathin, plasmonic super absorbers.Nat. Commun., 2 (2011), p. 517

4. H.A. Atwater, A. Polman. Plasmonics for improved photovoltaic devices. Nat. Mater., 9 (2010), pp. 205–213

5. V.E. Ferry, M.A. Verschuuren, H.B.T. Li, E. Verhagen1, R.J. Walters, R.E.I. Schropp, H.A. Atwater, A. Polman, Light Trapping In Thin Film Plasmonic Solar Cells, Proc. 25th EU-PVSEC Conference, Valencia, 2010, pp. 6–10.

6. S. Pillai, M.A. Green. Plasmonics for photovoltaic applications. Sol. Energy Mater. Sol. Cells, 94 (2010), pp. 1481–1486

7. C. Wu, Y. Avitzour, G. Shvets. Ultra-thin wide-angle perfect absorber for infrared frequencies Proc. SPIE, 7029 (2008), p. 70290

8. Mehta. S, GreenTech Solar, 2010 〈 http://www.greentechmedia.com/articles/read/the-prospects-of-amorphous-silicon-down-but-hardly-out〉.

9. D.L. Staebler, C.R. Wronski. Reversible conductivity changes in discharge-produced amorphous Si, Appl. Phys. Lett., 31 (1977), pp. 292–294

10. H. Kakinuma, S. Nishikawa, T. Watanabe. Thickness dependence of Staebler-Wronski effect in a-Si:H. J. Non-Cryst. Solids, 59 (1983), pp. 421–424

11. H. Fritzsche. Development in understanding and controlling the Staebler–Wronski effect in a-Si: H., Ann. Rev. Mater. Res., 31 (2001), pp. 47–79

12. R.J. Koval, J.M. Pearce, A.S. Ferlauto, R.W. Collins, C.R. Wronski. Evolution of the mobility gap with thickness in hydrogen-diluted intrinsic Si: H materials in the phase transition region and its effect on p-i-n solar cell characteristics. MRS Proc., 664 (2001)

13. M.J.M. Pathak, K. Girotra, S.J. Harrison, J.M. Pearce. The effect of hybrid photovoltaic thermal device operating conditions on intrinsic layer thickness optimization of hydrogenated amorphous silicon solar cells.,Sol. Energy, 86 (2012), pp. 2673–2677

14. H.W. Deckman, C.R. Wronski, H. Witzke, E. Yablonovitch. Optically enhanced amorphous silicon solar cells. Appl. Phys. Lett., 42 (1983), pp. 968–970

15. T. Tiedje, B. Abeles, J.M. Cebulka, J. Pelz. Photoconductivity enhancement by light trapping in rough amorphous silicon. Appl. Phys. Lett., 42 (1983), pp. 712–714

16. A. Vora, J. Gwamuri, J.M. Pearce, P.L. Bergstrom, D.O. Guney. Multi-resonant silver nano-disk patterned thin film hydrogenated amorphous silicon solar cells for SWE compensation. J. Appl. Phys., 116 (2014), p. 093103

17. A.V. Zayats, I.I. Smolyaninov, A.A. Maradudin. Nano-optics of surface plasmon polaritons., Phys. Rep., 408 (2005), pp. 131–314

18. H.A. Atwater. The Promise of Plasmonics. Sci. Am., 296 (2007), pp. 56–62

19. S.A. Maier. Plasmonics: Fundamentals and Applications. Springer, Germany (2007)

20. J. Gwamuri, A. Vora, R.R. Khanal, A.B. Phillips, M.J. Heben, D.O. Guney, P.L. Bergstrom, A. Kulkarni, J.M. Pearce. Limitations of Ultra-Thin Transparent Conducting Oxides (TCOs) for Integration into Plasmonic-Enhanced Thin Film Solar Photovoltaic Devices. *Mater. Renew. Sustain. Energy* (2015), *4*, pp. 1–12

21. A. Vora, J. Gwamuri, N. Pala, A. Kulkarni, J.M. Pearce, D.O. Guney. Exchanging Ohmic losses in metamaterial absorbers with useful optical absorption for photovoltaics. Sci. Rep., 4 (2014), p. 4901

22. M.A. Green, S. Pillai. Harnessing plasmonics for solar cells. Nat. Photon., 6 (3) (2012), pp. 130–132

23. S.A. Maier, H.A. Atwater. Plasmonics: Localization and guiding of electromagnetic energy in metal/dielectric structures. J. Appl. Phys., 98 (2005) 011101–011101

24. M. Marikkannan, M. Subramanian, J. Mayandi, M. Tanemura, V. Vishnukanthan, J.M. Pearce. Effect of ambient combinations of argon, oxygen, and hydrogen on the properties of DC magnetron sputtered indium tin oxide films. AIP Adv., 5 (2015), p. 017128

25. Rein, Margrethe Holmer, PhD. Thesis, Submitted to University of Oslo, Norway, 2015.

26. S.A. Knickerbocker. Ph.D. Dissertation. Michigan Technological University, United States (1995)

27. T.S. Lim, M.S. Thesis, Michigan Technological University, 1997.

28. M. Logue, Indium–Tin-Oxide (ITO) Etchant Mixture Standard Operating Procedure, available at ⟨http://ssel-sched.eecs.umich.edu/wiki/Public.ITO%20Etching.ashx⟩.

29. E. Palik. Handbook of Optical Constants of Solids. Academic Press, Orlando (1985), pp. 355–357

30. ⟨http://rredc.nrel.gov/solar/spectra/am1.5/⟩.

31. L.A. Ryabova, V.S. Salun, I.A. Serbinov. Transparent conductive films of In2O3:Sn prepared by the pyrolysis method. Thin Solid Films, 92 (1982), pp. 327–332

32. A.K. Kulkarni, K.H. Schulz, T.S. Lim, M. Khan. Electrical, optical and structural characteristics of indium-tin-oxide thin films deposited on glass and polymer substrates. Thin Solid Films (1999), p. 345

33. D.H. Kim, M.R. Park, G.H. Lee. Preparation of high quality films ITO films on plastic substrates using RF magnetron sputtering. Surf. Coat. Technol., 201 (2006), pp. 927–931

5. Influence of Oxygen Concentration on the Performance of Ultra-Thin RF Magnetron Sputter Deposited Indium Tin Oxide Films as a Top Electrode for Photovoltaic Devices[4]

5.1. Introduction

Solar photovoltaic (PV) based electricity production is one of the significant ecofriendly methods to generate sustainable energy needed to mitigate the looming global energy crisis [1]. Despite technical improvements [2] and scaling [3], which have resulted in a significant reduction in crystalline silicon (c-Si) PV module costs, for continued PV industry growth [4,5], PV costs must continue to decline to reach a levelized cost of electricity [6] low enough to dominate the electricity market. One approach to reduced PV costs further is to transition to thin film PV technology [7]. Hydrogenated amorphous silicon (a-Si:H) based PV [8] have shown great potential for large scale [9] sustainable commercial production due to lower material costs and use of well-established fabrication techniques [10,11]. However, there is need to improve the efficiency of a-Si:H PV devices if they are to become the next dominant technology for solar cells commercialization. One method to improve a-Si:H PV performance is with optical enhancement [12]. Recent developments in plasmonic theory promise new light management methods for thin-film a-Si:H based solar cells [13–23]. However, previous work has shown these plasmonic approaches require the development of ultra-thin, low-loss and low-resistivity transparent conducting oxides (TCOs) [24]. Tin doped indium oxide (ITO), zinc oxide (ZnO) and tin oxide (SnO$_2$) are the three most important TCOs and are already widely used in the commercial thin film solar cells [25]. In addition, aluminum-dope zinc oxide (AZO) and fluorine-doped tin oxide (FTO) are among the other most dominant TCOs in various technological fields particularly the optoelectronic devices industry where TCOs have proved indispensable for applications such as photo electrochemical devices, light emitting diodes, liquid crystal displays and gas sensors [26,27]. ITOs can be prepared by direct current (DC) and radio frequency (RF) magnetron sputtering, electron beam evaporation, thermal vapor evaporation, spray pyrolysis, chemical solution deposition, and sol gel methods [28–34]. RF magnetron sputtering can be used to control the electrical and optical properties of the ITO thin films and is heavily used in industry [35].

---

[4] "The material contained in this chapter was previously published in *Materials.*"

Recent work by Vora *et al.* has emphasized the need for ultra-thin ITO top electrodes with low resistivity and high transmittances in the visible range of the electromagnetic spectrum as a prerequisite for the commercial realization of plasmonic-enhanced a-Si:H solar cells [36]. However, research by Gwamuri *et al.* has demonstrated that fabricating ultra-thin ITO films (sub-50 nm) using conversional methods presented a number of challenges since there is a trade-off between electrical and optical properties of the films [37]. It was evidenced from their results that electrical properties of RF sputter deposited sub-50 nm ITO films degraded drastically as their thickness is reduced, while the optical properties of the same films were seen to improve greatly [37]. To solve this problem, a novel method involving chemical shaving of thicker (greater than 80 nm) RF sputter deposited films was proposed and demonstrated [38]. Building on the promise of that technique, this study seeks to further understand the effect of oxygen concentration on the etch rates of RF sputter deposited ITO films and the impact on the TCO quality as a top electrode for PV devices. A detailed understanding of the interaction of all critical parameters, which determines the quality of ultra-thin ITO will help create even thinner layers with good quality to allow more finely tuned plasmonics resonances. ITO films were deposited using four different oxygen concentrations (0 sccm, 0.4 sccm, 1.0 sccm), annealed in air at 300 °C for 30 min and then etched for four different times (1, 3, 5 and 8 min) to establish the effect of oxygen on etch rates. These materials were characterized by x-ray diffraction (XRD), atomic force microscopy (AFM), Raman Spectroscopy, 4-point probe (4PP), and variable angle spectroscopic Ellipsometry (VASE). In addition, the thin films were investigated for candidates as acid-resistant TCOs for encapsulation of PV devices, which may reduce device processing steps and fabrication costs of completed modules in the future. The results are presented and discussed.

5.2. Materials and Methods

5.2.1. ITO Fabrication Process

ITO films were grown on (100) prime silicon substrates with a 98 nm thermally grown oxide, and on glass substrates using a 99.99% 100 mm diameter pressed ITO (SnO_2:In_2O_3 10:90 wt%) target. Before the deposition the substrates were ultrasonically cleaned in isopropanol and in DI water for 15 minutes and dried using N_2 atmosphere. The sputtering chamber was initiated to a low 10^{-7} Torr base pressure and the pressure was maintained at 7.5×10^{-3} Torr. The distance between the target and substrates was kept constant at 75 mm. As a standard procedure,

the target was pre-sputter cleaned at a power of 150 W, whereas the sputter deposition of the films was performed at 100 W. The argon gas flow rate was fixed at 10 sccm and the oxygen gas flow was varied such as 0, 0.4 and 1.0 sccm with sputter rate of 8–12 nm per minute. The sputter rate was seen to decrease with increase in oxygen flow rate. After deposition, ITO films were annealed at 300 °C for 30 min in air. ITO/Si films were subjected to the etching process using a standard chemical etchant mixture of HCl: HNO_3:H_2O (1:1:5) volume ratio. All the etching was performed at room temperature, resulting in a slow and controlled etch rate for the Si/SiO_2 films. Finally, the etched samples were thoroughly rinsed in DI water and dried under the nitrogen environment. This methodology was adapted from the previous study by Gwamuri *et al.*, 2015 [37].

The ITO films processed under different argon-oxygen ambient were chemically etched and characterized using various tools. The structural analyses of the ITO films were carried out using X-ray diffraction (XRD-Scintag-2000 PTS, Scintag Inc, Cupertino,CA, USA). Raman spectra for the ultra-thin film samples were measured at room temperature using Jobin-Yvon LabRAM HR800 Raman Spectrometer (Horiba Scientific, Edison,NJ, USA) with the excitation wavelength of 633 nm and the resolution is about ~0.1 cm^{-1}. Sheet resistance of the samples was characterized using four point probe station consisting of ITO optimized tips with 500 micron tip radii set to 60 grams pressure and an RM3000 test unit from Jandel Engineering Limited, Kings Langley, UK. The optical transmission and thickness of the films was determined using variable angle spectroscopic ellipsometry (UV-VIS V-VASE with control module VB-400, J.A. Woollam Co., Lincoln, NE, USA). Surface roughness was evaluated using a Veeco Dimension 3000 atomic force microscope (Veeco, Oyster City, NY, USA operated in tapping mode with Budget Sensors Tap300Al-G cantilevers (Innovative Solutions Bulgaria Ltd, Sofia, Bulgaria). It should be noted that transmittance data was measured for ITO on sodalime glass (SLG) substrate and all the rest of the data was on ITO on Si/SiO_2 substrate.

5.2.2. Chemical Shaving: Wet Etching

In this present work, the oxygen 0, 0.4 and 1.0 sccm deposited ITO films were used for the etching process for 1, 3, 5 and 8 min, respectively. The annealed ITO/Si samples are etched at room temperature using HCl:HNO_3:H_2O (1:1:5) combination and the resistivity and thickness of the films were checked for 1, 3, 5 and 8 min etched films. For the 0 sccm ITO films, the thickness of the film was changed from 70 to 44 nm for 1 to 5 min etching time. Similarly the 0.4 sccm films thickness changed from 89 to 47 nm and 84 to 22 nm for 1.0 sccm films. The decrement of

thickness was reflected in the resistivity values. The chemical reaction of the HCl and HNO_3 etching reactions are as follows [39]:

$$In_2O_3 + 2HCl \rightarrow 2InCl + H_2O + O_2 \ (\Delta H) \qquad (5.1)$$

$$In_2O_3 + 12HNO_3 \rightarrow 2In \ (NO_3)_3 + 6NO_2 + 6H_2O \qquad (5.2)$$
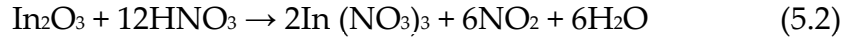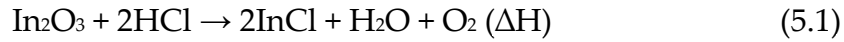
5.3. Results

5.3.1. Structural Analysis

5.3.1.1. XRD Analysis

XRD results for the ITO films deposited using different oxygen concentrations (0 sccm, 0.4 sccm, 1.0 sccm), annealed in air at 300 °C for 30 min and then etched for different times (1, 3, 5 and 8 min) are shown in Figure 5.1.
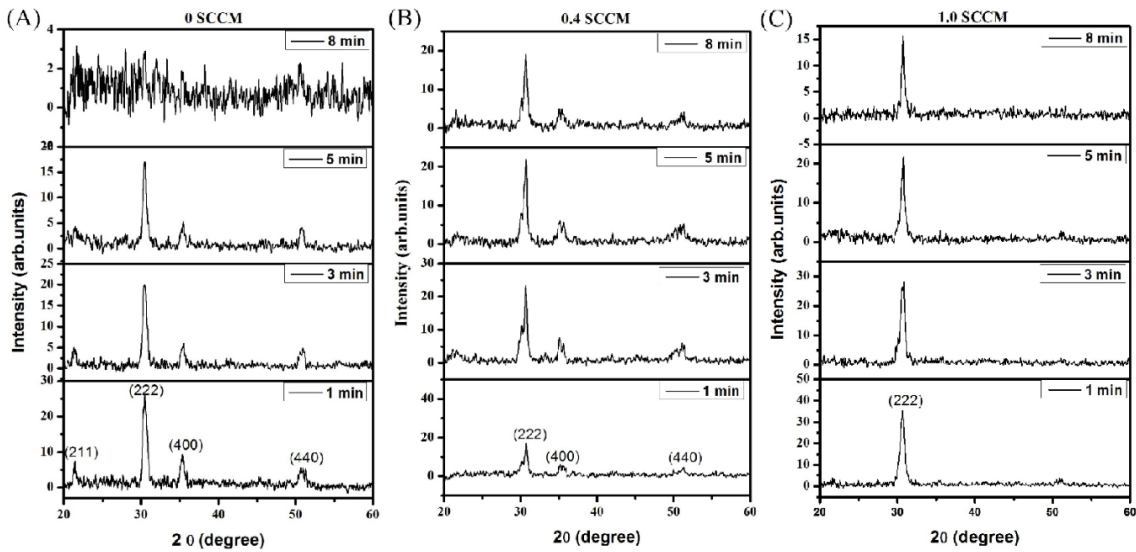
Figure 5.1. XRD pattern for ITO films deposited under different oxygen ambient conditions and etched for 1, 3, 5 and 8 min: (A) 0 sccm oxygen; (B) 0.4 sccm oxygen; (C) 1.0 sccm oxygen. Argon flow rate was maintained at 10 sccm for all materials.

In addition to that the peak shown at (222), (400) and (440) reflections are indexed to be cubic indium oxide (JCPDS No: 06-0416) [40]. All the films have a polycrystalline nature with stronger (222) reflection. No other tin phases could be identified from the cubic indium tin oxide. Normally the 30% of Sn is needed to exhibiting the SnO_2 diffraction lines in ITO. The (222) and (400) plane is ascribed for oxygen efficient and deficient nature of ITO films [41]. The effect of the oxygen flow rate on the peak intensity of the ITO films is clearly shown in the XRD spectrum. There is a general increase in the peak intensities with increased oxygen

flow rate. Similarly the reflections such as (211), (400) and (440) are due to the minimum oxygen concentration in the sputter chamber. These planes are absent in the XRD pattern of ITO film processed in an oxygen-rich (1.0 sccm) environment. There is a strong evidence that for the highest oxygen ambient (1.0 sccm), (222) is the preferred growth orientation for RF sputter deposited ITO films. Varying the oxygen concentration will result in changing the preferred growth orientation of the films to other crystal lattice planes such as the (211), (400) or (440). The intensity ratios are strongly dependent on the critical level of In^{3+} and O^{2-} pairs and the pairs' density is different for different etching periods of time [42]. The presence of high oxygen concentration induce the In-O bonding networks formation and promote growth of the (222) crystal lattice planes.

During the etching, ITO films are reduced to In–Cl and $In-(NO_3)_3$ resulting in the change in crystallinity of films etched for different periods of time. The structural parameters such as d spacing, lattice constants, net lattice distortion and grain sizes are estimated and listed in Table 5.1. in comparison to data from the Joint Committee on Powder Diffraction Standards (JCPDS)/International Centre for Diffraction Data (ICDD) database.

The etching process also distorts the ITO structural long - range order, which has an impact on the opto-electronic properties of the films. The grain size of films did not change even after etching for 8 min., particularly for ITO films processed in an oxygen deficient environment. During the etching process the excess weakly bound oxygen atoms are removed from the ITO surfaces exposing layers with different grain sizes. The ITO structure distortion due to etching for longer periods of time (8 min) can be seen from the XRD spectra shown in Figure 5.1. There was however no evidence of ITO film for the results shown in Figure 1A after they were etched for 8 min. There is evidence of decreased crystallinity for the rest of the ITO films (Figure 1B,C) as the oxygen atoms are stripped from the In–O network by the HCl and HNO_3.

Table 5.1. Structural parameters of ITO sputtered films with 0, 0.4 and 1.0 sccm oxygen and etched at 1, 3, 5 and 8 min.

Oxygen Flow Rate (sccm)	Etching Time (min)	D Spacing (222) (Å)	Lattice Constant (222) (Å)	Net-Lattice Distortion	Grain Size (222) (nm)
Standard JCPDS for ITO 06-0416	–	2.921	10.1180	–	–
0	1	2.932	10.1552	–0.0036	16
	3	2.934	10.1629	–0.2970	16
	5	2.934	10.1629	–0.2885	17
	8	–	–	–	–
0.4	1	2.908	10.0731	–0.0075	31
	3	2.912	10.0869	–0.0157	25
	5	2.914	10.0954	–0.0153	23
	8	2.914	10.0954	–0.0169	20
1.0	1	2.917	10.1059	–	13
	3	2.913	10.0915	–0.2828	13
	5	2.911	10.0845	–	14
	8	2.908	10.0764	–	19

5.3.1.2. AFM Analysis

Figure 5.2. shows the AFM surface topology of the ITO films deposited under three different oxygen environments and etched for 1 min and 8 min.
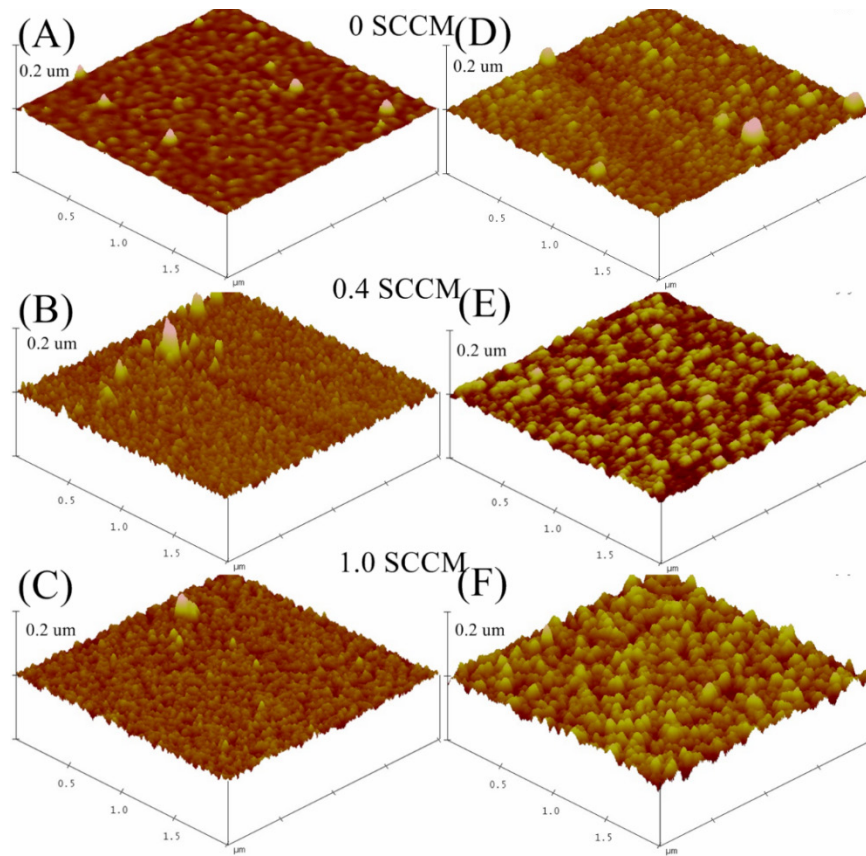
Figure 5.2. Surface topology image for 2 μm × 2 μm × 0.2 μm of the ITO film deposited under various oxygen environments: (A) 0 sccm oxygen, (B) 0.4 sccm oxygen, (C) 1.0 sccm oxygen, and etched for 8 min, (D) 0 sccm oxygen, (E) 0.4 sccm oxygen and 1 sccm oxygen. (A–C) etched for 1 min and (D–F) films etched for 8 min. The etching was performed at room temperature.

Figure 5.2A, B shows the ITO films deposited in an oxygen deficient ambient and etched for 1 and 8 min, respectively. Spherical sized grains are clearly visible in all AFM images presented in Figure 5.2. There is variation of surface roughness of the films with both oxygen flow rate and etching time of the ITO films. The minimum value of surface roughness of 0.65 nm was measured for ITO films sputtered using 0.4 sccm oxygen flow rate and etched for 1 min, while a maximum surface roughness value of 8.9 nm was observed for films processed at 1.0 sccm oxygen flow rate and etched for 1 min. There was a slight increase in roughness with etching time observed for 0 sccm and 0.4 sccm ITO film, for etching times 1 min to 8 min.. However, the 1.0 sccm films, showed the greatest variation in surface roughness even after 1 min etching process. Generally, the surface roughness of the films are observed to increase when the oxygen gas concentration is increased during processing.

5.3.1.3. Raman Spectroscopy

Figure 5.3. shows the Raman spectrum for ITO deposited at various oxygen compositions and etched at 1, 3, 5 and 8 min respectively. Raman spectroscopy is used to determine the structural conformations of the materials. Group theory predicts the Raman modes for cubic indium oxide, such as 4Ag (Raman), 4Eg (Raman), 14Tg (Raman), 5Au (inactive), and 16Tu (infrared) modes [43]. The modes observed are at 303, 621 and 675 cm^{-1} for all the films. Noticeable modes are exhibited at 302 and 621 for Eg and In–O vibrational mode [44]. The observed Raman modes in Figure 5.3. are in good agreement with previous reported results [40]. There are no other additional modes observable for the SnO and SnO$_2$ structures. In addition to that the broad band shown at 976 to 1013 cm^{-1} for all the etched films and it was not unassignable. The peak appeared at 1132, 1112, 1097 and 1120 cm^{-1} for 0, 0.4 and 1.0 sccm ITO etched films. These peaks are reported in the commercially ITO films [45]. The Raman results are correlated with XRD results. No other mixed phases were observed in the Raman spectrum indicating that etching process had no or little effect on the ITO structure.
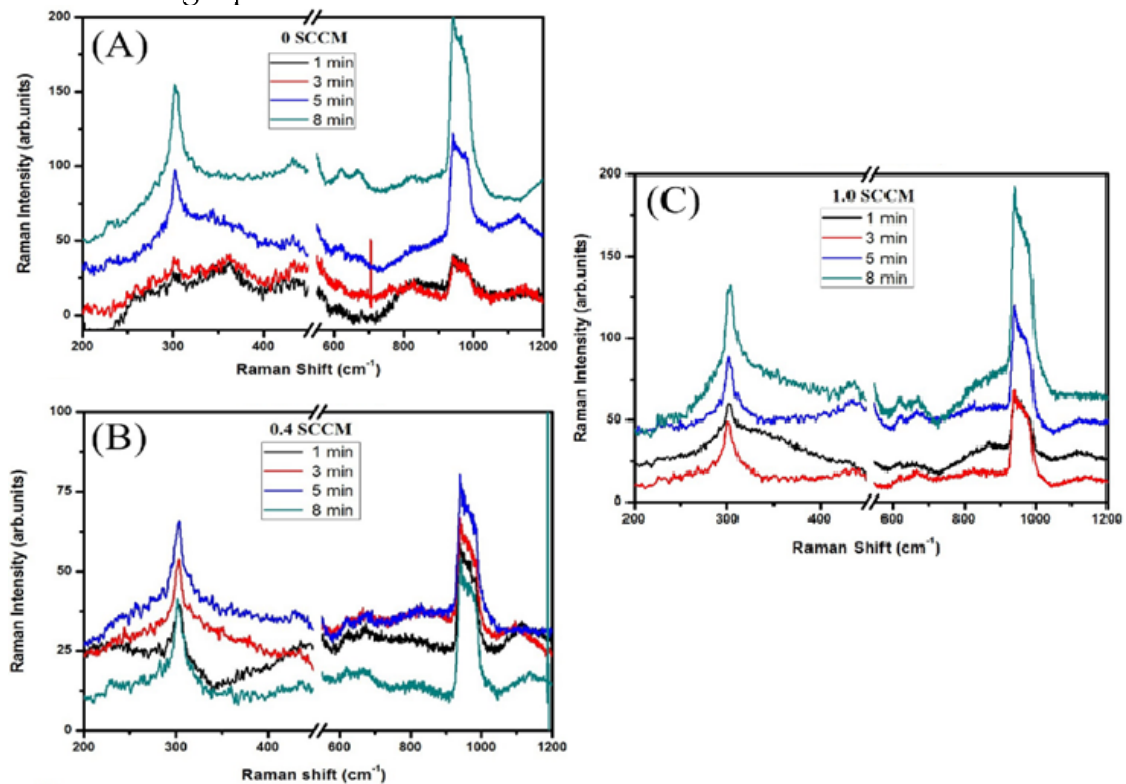
Figure 5.3. Raman spectra for the ITO films deposited under various oxygen concentrations and etched for 1, 3, 5 and 8 min., respectively. (A) 0 sccm; (B) 0.4 sccm; (C) 1.0 sccm.

5.3.2. Resistivity

The electrical properties of the different oxygen ambient deposited and etched ITO films were measured using a four point probe. The sheet resistance values of the ITO films are changed with respect to the oxygen ambient nature and etching time and are summarized in Table 5.2.

Table 5.2. Electrical and optical parameters of ITO films deposited under various oxygen compositions and etched for 1, 3, 5 and 8 min.

Oxygen flow rate (sccm)	Etching Time (min)	Sheet resistance($\Omega/\square$)	Thickness (nm)	Resistivity (Ω.cm)	Transmission (%)
0	1	83.28	70	5.83×10^{-4}	76.29
	3	103.47	59	6.11×10^{-4}	93.98
	5	209.49	44	9.22×10^{-4}	90.27
	8	–	–	–	100
0.4	1	209.02	89	1.86×10^{-3}	91.45
	3	194.23	88	1.71×10^{-3}	85.26
	5	240.08	85	2.04×10^{-3}	84.85
	8	326.9	47	1.54×10^{-3}	83.71
1.0	1	1000	84	8.4×10^{-3}	90.96
	3	2000	62	1.24×10^{-2}	89.25
	5	2400	50	1.20×10^{-2}	100
	8	7350	22	1.62×10^{-2}	100

From the obtained results, the minimum sheet resistance was observed for ITO deposited using argon ambient (0 sccm oxygen) and etched for 1 min. However, the same films exhibited the worst transmittance of about 76%. During processing in an argon rich environment, the bombardment by argon neutrals creates dangling bonds in the substrates and created the oxygen vacancies in the ITO films [46]. The argon environment (10 sccm) (*i.e.*, the oxygen deficient environment)

promotes oxygen vacancies that enhance electrical resistivity while degrading the optical properties of the films. This is reflected in the XRD spectra, where the (400) and (440) lattice planes are enhanced for ITO films processed in low oxygen (0 sccm and 0.4 sccm) environments. Hence, the 1.0 sccm deposited films in which the (222) lattice plane is dominant, showed a higher electrical resistivity compared to the other films. The resistivity of the films are highly dependent on the film thickness, which is a function of the etching time. Increasing the etching time decreases the thickness of the films, and, hence, the electrical properties while improving optical properties.

5.3.3. Transmittance

Optical transmittances of the ITO films on glass substrates are recorded from 300 to 1000 nm at room temperature and shown in Figure 5.2. All the films exhibited the highest average optical transmittance in the higher wavelength range. The highest optical transmittance is attained for 0 sccm oxygen ITO film etched for 8 min with and average etch rate of 5.2 nm/min (for 5 min etch) and the 1.0 sccm films etched for 5 and 8 min with average etch rates of 5.25 and 7.75 nm/min, respectively. The results are summarized in Table 5.2. The thickness of the film is an important parameter for determining both electrical and optical properties of the ITO films. In this work, the thickness was quantified using spectroscopic ellipsometry measurements and is shown in the Table 5.2. For transmittance measurements, the ITO films were deposited on SLG substrates. The SLG transmittance is measured and used as baseline data. All ITO films transmittance data involve baseline subtraction, hence 100% transmittance means that all of the ITO film has been etched off. The etch rates were much faster for the ITO on glass such that all the film was etched-off after an 8-min etch (Figure 5.4.A), and 5 and 8 min (Figure 5.4.C).

The results show a direct correlation between the oxygen concentration and the optical transmittances of the films and an inverse relationship with the electrical conductivity of the ITO films. These results are in agreement with observation from previous studies [47,48]. Figure 4A for 8 min etch, and Figure 5.4.C for 5 and 8 min etch showed a transmittance cut-off wavelength around 350 nm indicating the absorption edge.
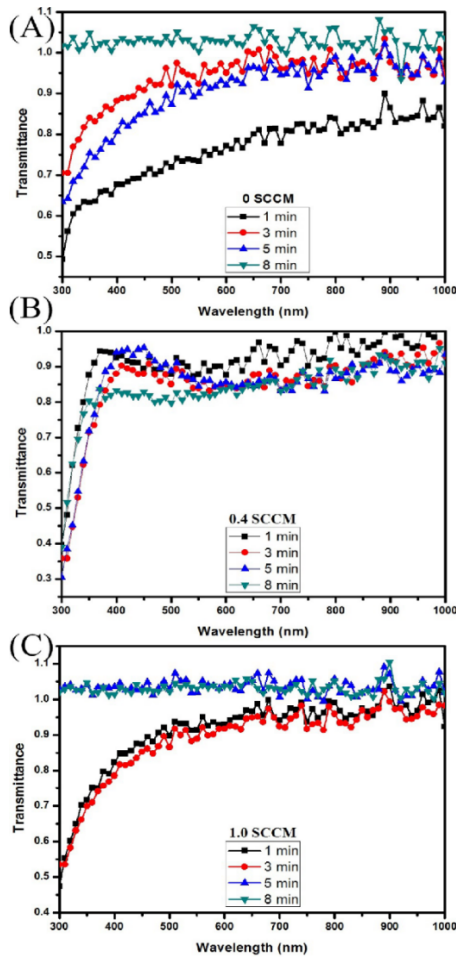
Figure 5.4. Optical transmission spectrum for the RF sputter deposited ITO films at different oxygen compositions and etched for min (A) 0 sccm, (B) 0.4 sccm, and (C) 1.0 sccm

5.4. Discussion

The results presented provide further insight on the interaction of the most common fabrication variables that influence the electrical and optical properties of ITO films for PV and other opto-electronic applications. There is evidence of a strong correlation between oxygen concentration and both the resistivity and transmittances of RF sputter deposited ITO films. The processing conditions have a strong bearing on the structure of the ITO films. The (222) lattice planes are preferred in films grown in oxygen rich ambient whilst more lattice planes; (211), (222), (400), and (440) are observed in films grown under less oxygen or oxygen deficient conditions. Wan *et al.* have reported the (211), (400) and (440) planes reflections as being associated with ITO films processed under high RF power in an oxygen deficient atmosphere [35]. From the structural analysis, the exhibited (222) reflection clearly indicated the cubic indium oxide formation. The film

81

growth rate decreased with increased O_2 concentration resulting in a much thicker ITO critical thickness (amorphous to polycrystalline transition thickness) for the 0 sccm RF sputtered films. The overall film is mixed phase crystalline and amorphous in nature. The noise is due to the ultra-thin porous and amorphous film left once the top crystalline film is etched off. This is not observed in the 0.4 and 1 sccm films because the increased oxygen composition results in reduced growth rates giving films that are more crystalline in nature with a much thinner critical thickness.

The lattice parameters and lattice distortion are seen to vary closely with oxygen concentration in the sputter chamber and the length of the etching process. The different oxygen- argon ratios sputtered ITO films have different etching behaviors, which then effected their electrical and optical properties. During the etching process, the crystal lattice of ITO films is degraded due to the exchange of bonds between indium oxide with HCl and HNO_3. This means that the indium oxide In–O and H–Cl bonds are substituted by In–Cl, In-$(NO_3)_3$ and O–H in the ITO surfaces [49]. These kinds of reactions may reduce the oxygen concentrations and distort structural long range order of the ITO films. This was reflected in the variation of electrical and optical properties of the ITO films with etching time. As no evidence of tin phases were detected, it can be concluded the reactions involving tin phases have negligible effect on the overall etch rates described in this study.

It is interesting to note that the ITO films processed at the 0.4 sccm oxygen flow rate presented the greatest resistance to acid etching in addition to exhibiting above moderate electrical and optical properties. These films show potential as candidate materials for encapsulation of PV devices or transparent conducting electrodes for varied application in acid-rich environment. However, further research into optimization of anti-acid (acid resistant) ITO films will be required before the material can be implemented in commercial PV devices.

Usually ITO is sputtered in varied combinations of reactive gas environments of argon with oxygen, hydrogen and nitrogen [40]. The oxygen ambient has been shown to be an important parameter to control electrical and optical properties. The highest oxygen concentrations enhance the transmission property and the oxygen deficient nature (oxygen vacancies) increased the electrical conductivity of the ITO thin films [47,48]. Hence, a sufficient amount of oxygen concentration can improve the opto-electronic performance of ITO thin films. High-quality ultra-thin ITO films are a needed significant step towards the realization and possible commercialization of plasmonic-based a-Si:H thin-film PV devices [15,24,36–38].

These devices have a potential to transform the thin-film based solar cells industry due to their low cost and ease of fabrication. In addition, plasmonic-enhanced PV has the potential to exhibit sophisticated light management schemes enabling unprecedented control over the trapping and propagation of light within the active region of the PV device [15], which would be expected to result in record-high device solar energy conversion efficiencies.

5.5. Conclusions

In this study, ultra-ITO thin films have been RF sputter deposited using different oxygen flow rates and chemical shaving is performed at room temperature for different time periods. The thicknesses of the films are altered as a result from 89 nm to 22 nm. In-between each etching process cycle, the films were characterized for both electrical and optical properties. Generally, the transmittance of the ITO films was observed to increase with decreasing film thickness, while the electrical properties were observed to degrade for the same films. This was attributed to the distortion of the In-O lattice long-range order due to the reduction reaction between the ITO and the etchants (acids). The novel method of chemical shaving further investigated here, is a simple and low-cost method with the potential to produce low loss and highly conductive ultra-thin and acid resistant ITO films for applications ranging from PV devices transparent electrodes to anti-acid materials. Using this method, ultra-thin ITO films with record low resistivity values (as low as 5.83×10^{-4} Ω.cm) were obtained and the optical transmission is generally high in the 300–1000 nm wavelength region for all films. The etching rate strongly depends on the oxygen concentrations of RF sputtered ITO films as well as on the post process annealing. This processing has an effect on the oxygen vacancies densities even for the 0 sccm O_2 films. Surface roughness increased as the concentration of oxygen increased as expected. The etching reactions are simple redox reaction, hence the rates should increase with increases in O_2 concentration especially for non-stoichiometric films with distorted ITO matrix. The etch rate, preferred crystal lattice growth plane, d-spacing and lattice distortion were also observed to be highly dependent on the nature of growth environment for RF sputter deposited ITO films.

Author Contributions: Jephias Gwamuri, Jeyanthinath Mayandi and Joshua M Pearce conceived and designed the experiments; Jephias Gwamuri, Jeyanthinath

Mayandi, Marikkannan Murugesan and Patrick K Bowen performed the experiments; all authors analyzed the data; Jeyanthinath Mayandi and Joshua M Pearce contributed materials and tools; and all authors wrote the paper.

Conflicts of Interest: The authors declare no conflict of interest.

References

1. J.M. Pearce. Photovoltaics—A path to sustainable futures. *Futures* **2002**, *34*, 663–674.
2. U. Pillai,. Drivers of cost reduction in solar photovoltaic. *Energy Econ.* **2015**, *50*, 286–293.
3. C. Honeyman.; T. Kimbis,. *Solar Market. Insight Report 2014 Q2*; Solar Energy Industrial Association and GTM research: DC, USA, 2014.
4. C. Candelise; M.Winskel,; R.J.K .Gross,. The dynamics of solar PV costs and prices as a challenge for technology forecasting. *Renew. Sustain. Energy Rev.* **2013**, *26*, 96–107.
5. E.S.Rubin; I.M.L. Azevedo; P. Jaramillo; S. Yeh,. A review of learning rates for electricity supply technologies. *Energy Policy* **2015**, *86*, 198–218.
6. K. Branker; M.J.M.Pathak; J.M. Pearce,. A Review of Solar Photovoltaic Levelized Cost of Electricity. *Renew. Sustain. Energy Rev.* **2011**, *15*, 4470–4482.
7. A. Shah; P. Torres; R. Tscharner; N. Wyrsch; H. Keppner,. Photovoltaic technology: The case for thin-film solar cells. *Science* **1999**, *285*, 692–698.
8. D.E. Carlson; C.R Wronski,. Amorphous Silicon Solar Cell. *Appl. Phys. Lett.* **1976**, *28*, 671−673.
9. J.M. Pearce,. Industrial symbiosis of very large-scale photovoltaic manufacturing. *Renew. Energy* **2008,** *33*, 1101–1108.
10. C.R. Wronski,; J.M. Pearce,; R.J. Koval,; A.S. Ferlauto,; R.W. Collins,. Progress in Amorphous Silicon Based Solar Cell Technology. Available online: http://www.rio12.com/rio02/proceedings/pdf/067 (accessed on 13 October 2015).
11. R.W. Collins; A.S. Ferlauto; G.M. Ferreira; C. Chen; , J. Koh; R.J. Koval; Y. Lee; J.M. Pearce; C.R. Wronski,. Evolution of microstructure and phase in amorphous, protocrystalline, and microcrystalline silicon studied by real time spectroscopic ellipsometry. *Solar Energy Mater. Solar Cells* **2003**, *78*, 143–80.
12. H.W. Deckman; C.R. Wronski; H. Witzke; E Yablonovitch. Optically enhanced amorphous silicon solar cells. *Appl. Phys. Lett.* **1983**, *42*, 968–970.
13. H.A. Atwater; A Polman. Plasmonics for improved photovoltaic devices. *Nat. Mater*. **2010**, *9*, 205–213.

14. D. Derkacs; S.H. Lim; P. Matheu; W. Mar; E.T Yu. Improved performance of amorphous silicon solar cells via scattering from surface plasmon polaritons in nearby metallic nanoparticles. *Appl. Phys. Lett*. **2006**, *89*, 093103–093105.

15. J.Gwamuri; D.Ö. Güney; J.M. Pearce,. Advances in Plasmonic Light Trapping in Thin-Film Solar Photovoltaic Devices. In *Solar Cell. Nanotechnology*; A., Tiwari, R., Boukherroub, M., Maheshwar Sharon, Eds.; Wiley: Hoboken, NJ, USA, 2013; pp. 241–269.

16. P. Spinelli; V.E. Ferry ,; J. van de Groep; M. van Lare; M.A. Verschuuren; R.E.I. Schropp; H.A. Atwater; A. Polman,. Plasmonic light trapping in thin-film Si solar cells. *J. Opt*. **2012**, *14*, 024002–024012.

17. W. Cai; V.M. Šalaev,. *Optical Metamaterials: Fundamentals and Applications*; Springer: NY, USA, 2009.

18. S.A. Maier; H.A. Atwater,. Plasmonics: Localization and guiding of electromagnetic energy in metal/dielectric structures. *J. Appl. Phys*. **2005**, *98*, 011101–011110.

19. K. Aydin; V.E. Ferry; R.M. Briggs; H.A. Atwater,. Broadband polarization-independent resonant light absorption using ultrathin plasmonic super absorbers. *Nat. Commun*. **2011**, *2*, 517.

20. C. Wu; Y. Avitzour; G. Shvets,. Ultra-thin wide-angle perfect absorber for infrared frequencies. *Proc. SPIE* **2008**, *7029*, doi:10.1117/12.797208.

21. V.E. Ferry; M.A. Verschuuren; C. van Lare; E.I. Ruud; H.A. Atwater; A. Polman,. Optimized spatial correlations for broadband light trapping nano patterns in high efficiency ultrathin film a-Si:H solar cells. *Nano Lett.* **2011**, *11*, 4239–4245.

22. J. Trevino; C. Forestiere; G. Di Martino; S. Yerci; F. Priolo; L. Dal Negro,. Plasmonic-photonic arrays with aperiodic spiral order for ultra-thin film solar cells. *Optics Express* **2012**, *20*, A418–A430.

23. I. Massiot; C. Colin; N. Pere-Laperne; P. Roca i Cabarrocas; C. Sauvan; P. Lalanne; J.-L. Pelouard; S. Collin,. Nanopatterned front contact for broadband absorption in ultra-thin amorphous silicon solar cells. *Appl. Phys. Lett*. **2012**, *101*, 163901–163903.

24. A. Vora; J. Gwamuri; N. Pala; A. Kulkarni; J.M. Pearce; D.Ö. Güney,. Exchanging Ohmic losses in metamaterial absorbers with useful optical absorption for photovoltaics. *Sci. Rep.* **2014**, *4*, 1–13.

25. K. Sato; Y. Gotoh; Y. Wakayama; Y. Hayashi; K. Adachi; H. Nishimura,. Highly textured SnO_2:F TCO films for a-Si solar cells. *Rep. Res. Lab. Asahi Glass Co. Ltd* **1992**, *42*, 129–137

26. A. Dixit; C. Sudakar; R. Naik; V.M. Naik; G. Lawes. Undoped vacuum annealed In$_2$O$_3$ thin films as a transparent conducting oxide. *Appl. Phys. Lett.* **2009**, *95*, 192105–192107.

27. J.H. Lan; J. Kanicki,. ITO surface ball formation induced by atomic hydrogen in PECVD and HW-CVD tools. *Thin Solid Films* **1997**, *304*, 123–129.

28. A. Thøgersen; M. Rein; E. Monakhov; J. Mayandi; S. Diplas,. Elemental distribution and oxygen deficiency of magnetron sputtered indium tin oxide films. *J. Appl. Phys.* **2011**, *109*, 113532.

29. H.K. Park; S.W. Yoon; W.W. Chung; B.K. Min; Y.R. Do,. Fabrication and characterization of large-scale Multifunctional transparent ITO nanorod films. *J. Mater. Chem. A* **2013**, *1*, 5860–5867.

30. S.I. Castaneda; F. Rueda; R. Diaz; J.M. Ripalda; I. Montero,. Whiskers in Indium tin oxide films obtained by electron beam evaporation. *J. Appl. Phys.* **1998**, *83*, 1–8.

31. J.L. Yao; S. Hao; J.S. Wilkinson,. Indium Tin Oxide Films by Sequential Evaporation. *Thin Solid Films* **1990**, *189*, 221–233.

32. H. Kobayashi; Y. Kogetsu; T. Ishida; Y. Nakato,. Increase in photovoltage of "indium tin oxide/Silicon oxide/ mat-textured n–silicon" junction solar cells by silicon peroxidation and annealing processes. *J. Appl. Phys.* **1993**, *74*, 4756–4761.

33. J. Lee; S. Lee; G. Li; M.A. Petruska; D.C. Paine; S. Sun,. A Facile Solution-Phase Approach to Transparent and Conducting ITO Nanocrystal Assemblies. *J. Am. Chem. Soc.* **2012**, *134*, 13410–13414.

34. Z. Chen; W. Li; R. Li; Y. Zhang; G. Xu; H. Cheng,. Fabrication of Highly Transparent and Conductive Indium-Tin Oxide Thin films with a high figure of merit via solution processing. *Langmuir* **2013**, *29*, 13836–13842.

35. D. Wan; P. Chen; J. Liang; S. Li; F. Huang,. (211)-Orientation Preference of Transparent Conducting In$_2$O$_3$:Sn Films and Its Formation Mechanism. *ACS. Appl. Mater. Interfaces* **2011**, *3*, 4751–4755.

36. A. Vora; J. Gwamuri; J.M. Pearce; P.L. Bergstrom; D.O. Guney,. Multi-resonant silver nano-disk patterned thin film hydrogenated amorphous silicon solar cells for Staebler-Wronski effect compensation. *J. Appl. Phys.* **2014**, *116*, 093103.

37. J. Gwamuri; A. Vora; R.R. Khanal; A.B. Phillips; M.J. Heben; D.O. Guney; P. Bergstrom; A. Kulkarni; J.M. Pearce,. Limitations of ultra-thin transparent conducting oxides for integration into plasmonic-enhanced thin-film solar photovoltaic devices. *Mater. Renew. Sustain. Energy* **2015**, *4*, 1–12.

38. J. Gwamuri; A. Vora; J. Mayandi; D.O. Guney; P. Bergstrom; J.M. Pearce. A New Method of Preparing Highly Conductive Ultra-Thin Indium Tin Oxide for Plasmonic-Enhanced Thin Film Solar Photovoltaic Devices. *Solar Energy Materials and Solar Cells* 149, 250-257

39. C.J. Hang; Y.K. Su; S.L. Wu. The effect of solvent on the etching of ITO electrode. *Mater. Chem. Phys.* **2004**, *84*, 146–150.

40. M. Marikkannan; M. Subramanian; J. Mayandi; M. Tanemura; V. Vishnukanthan; J.M. Pearce. Effect of ambient combinations of argon, oxygen, and hydrogen on the properties of DC magnetron sputtered indium tin oxide films. *AIP Adv.* **2015**, *5*, 017128–017138.

41. S. Luo; S. Kohiki; K. Okada; F. Shoji; T. Shishido. Hydrogen effects on crystallinity, photoluminescence, and magnetization of indium tin oxide thin films sputter-deposited on glass substrate without heat treatment. *Phys. Status Solidi A* **2010**, *207*, 386–390.

42. K. Kato; H. Omoto; T. Tomioka; A. Takamatsu. Changes in electrical and structural properties of indium oxide thin films through post-deposition annealing. *Thin Solid Films* **2011**, *520*, 110–116.

43. D. Liu; W.W. Lei; B. Zou,. High pressure X-ray diffraction and Raman spectra study of indium oxide. *J. Appl. Phys.* **2008**, *104*, 083506–083511.

44. O.M. Berengue; A.D. Rodrigues; C.J. Dalmaschio; A.J.C. Lanfredi; E.R. Leite; A.J. Chiquito,. Structural characterization of indium oxide nanostructures: A Raman analysis. *J. Phys. D Appl. Phys.* **2010**, *43*, 045401–045404.

45. R. Chandrasekhar; K.L. Choy. Innovative and cost-effective synthesis of indium tin oxide films. *Thin Solid Films* **2001**, *398–399*, 59–64.

46. S.N. Luo; A. Kono; N. Nouchi; F. Shoji. Effective creation of oxygen vacancies as an electron carrier source in tin-doped indium oxide films by plasma sputtering. *J. Appl. Phys.* **2006**, *100*, 113701–113709.

47. K. Okada; S. Kohiki; S. Luo; D. Sekiba; S. Ishii; M. Mitome; A. Kohno; T. Tajiri; F. Shoji,. Correlation between resistivity and oxygen vacancy of hydrogen-doped indium tin oxide thin films. *Thin Solid Films* **2011**, *519*, 3557–3561.

48. T. Ashida; A. Miyamuru; N. Oka; Y. Sato; T. Yagi; N. Taketoshi; T. Baba; Y. Shigesato,. Thermal transport properties of polycrystalline tin-doped indium oxide films. *J. Appl. Phys.* **2009**, *105*, 073709–073712.

49. J.E.A.M. Van den Meerakker; P.C. Baarslag; W. Walrave; T.J. Vink; J.L.C. Daams. On the homogeneity of sputter-deposited ITO films Part II. Etching behavior. *Thin Solid Films* **1995**, *266*, 152–156.

6. Ambient-dependent Agglomeration and Surface-Enhanced Raman Spectroscopy Response of Self-Assemble Silver Nano-particles for Plasmonic Photovoltaic Devices[5]

6.1. Introduction

As-deposited thin metallic films are generally metastable or unstable and readily de-wet from a solid substrate when heated even well below their melting temperature [1,2]. The process of agglomeration / de-wetting proceeds in two ways: nucleation and growth of holes, and Spinodal dewetting [1,3-5]. This process is a relatively economical means of obtaining both simple and complex nano-structures from thin metal films [5-10] compared to traditional methods such as e-beam lithography. Whilst dewetting during film processing have been reported to have undesirable effects on micro- and nano-systems, agglomeration has become the method of choice for catalyzed growth of nanotubes / nanowires and electronic and photonic devices [3]. Dewetting of thin metallic films (both liquid and solid) to obtain mono/multi-disperse nanoparticles has been demonstrated with a range of metals including: gold (Au), silver (Ag), nickel (Ni), copper (Cu) and Alumina (Al), among others [1, 3-4, 10-11]. However, Ag films dewetting has been mostly investigated as candidate for plasmonic sensing [12 -18] and plasmonic-enhanced solar photovoltaics (PV) devices [19-31] applications. This is because Ag is generally considered to have the most suitable optical properties for solar cell applications. Silver nanoparticles exhibit highly intense and localized surface plasmon resonances (LSPR) and low absorption in the visible and near infrared [13, 32], which is also the spectral region of interest for PV devices. The LSPR of Ag nanoparticles results in electromagnetic-field enhancement that is responsible for the observed surface-enhanced Raman scattering (SERS) [12- 13]. In this work we focus on further exploiting the agglomeration/dewetting process of thin Ag films on indium tin oxide (ITO) RF sputtered on glass substrates to obtain self-assemble nanoparticles (SANPs) optimized for plasmonics based thin film hydrogenated amorphous silicon (a-Si:H) PV devices. This work further investigate the effect of annealing ambient on; Ag NPs average size, circularity, substrate area coverage/particle distribution, optical properties and SERS responses. In addition, XRD results will be used to discuss the research findings in order to provide guidance for the integration of Ag SANPs with a-Si:H PV devices.

---

[5] The material contained in this chapter is to be submitted to a journal.

6.2. Experimental Details

Experimental Details

Thin films (average thickness of 18.8 nm) of Ag were deposited using e-beam (KH Frederick EB12) onto ITO/glass substrates previously prepared according to the recipe described in refs [33-37]. Samples were divided into three batches according to annealing temperature S1 (210 ^{0}C), S2 (180 ^{0}C) and S3 (150 ^{0}C). The samples were further based on processing ambient. The ambient was varied during annealing of the films to influence both the average nanoparticle size and surface coverage/distribution. The ambient conditions included: argon (Ar), nitrogen (N$_2$) and vacuum (Vac). The annealing period was kept constant for all samples (1 hr) except for those processed under vacuum conditions, which were processed for 2 hrs (as this time was needed to reach the set temperature of 180 ^{0}C under vacuum). Samples processed at 180 ^{0}C are analysed in depth for two reasons: i) processing temperature is ideal for AgNPs – PV integration compared to 210 ^{0}C, which is greater than most p-a-Si:H layer processing temperature and, ii) there are challenges when trying to obtain uniformly distributed AgNPs from thin films processed at lower temperatures (150 ^{0}C and below).

Surface morphology was characterized with a Hitachi S4700 FE-SEM and images were processed using ImageJ (imagei.nih.gov) to determine particle size and distribution. Atomic force microscopy (AFM) was performed using a Veeco Dimension 3000 equipment with cantilever tips (Tap300Al-G) on a 1:1 acquisition aspect ratio and roughness analysis was performed on a defect-free region. The absorbance spectra were measured using a Shimadzu UV–Vis spectrophotometer (UV2450), and the structural analysis was carried out using a powder PANalytical X-ray diffractometer with CuKa radiation (k = 1.54 A°). Raman-scattering SERS measurements were performed in 180^0 backscattering geometry using a LabRamHR800 Spectrometer from Horiba Jobin–Yvon equipped with a CCD detector. The samples were excited by 633 nm emission from a He–Ne laser and the resolution of the spectrometer used was about 0.3 cm^{-1}.

6.3. Particle Size Analysis

6.3.1. SEM Analysis

SEM analysis was performed to determine ambient dependant agglomeration and the results are shown in Figure 6.1. a) – c) and as-deposited Figure 6.1. d). is included for comparison purposes. The dependence of the SANPs shape, surface coverage and size with processing ambient is evident from Figure 6.1. The SEM

analysis further reveals the presence of silver nanoparticle as small finite clusters in all samples, however, there is a vast contrast when it comes to the size and distribution of these clusters. In case of vacuum annealed films, the particles are more spherical in shape and uniformly distributed. There are two predominant sizes of particles present; one with small size around 50 nm and larger particles around 140 nm but the large particles are more dominant. For nitrogen annealed films, the particle are of finite clusters with uniform distribution and irregular shape and the average calculated particle size is around 77 nm. Argon annealed samples have a nearly spherical shape with distinguishable particle and some aggregated clusters and the average particle size is around 55 nm.
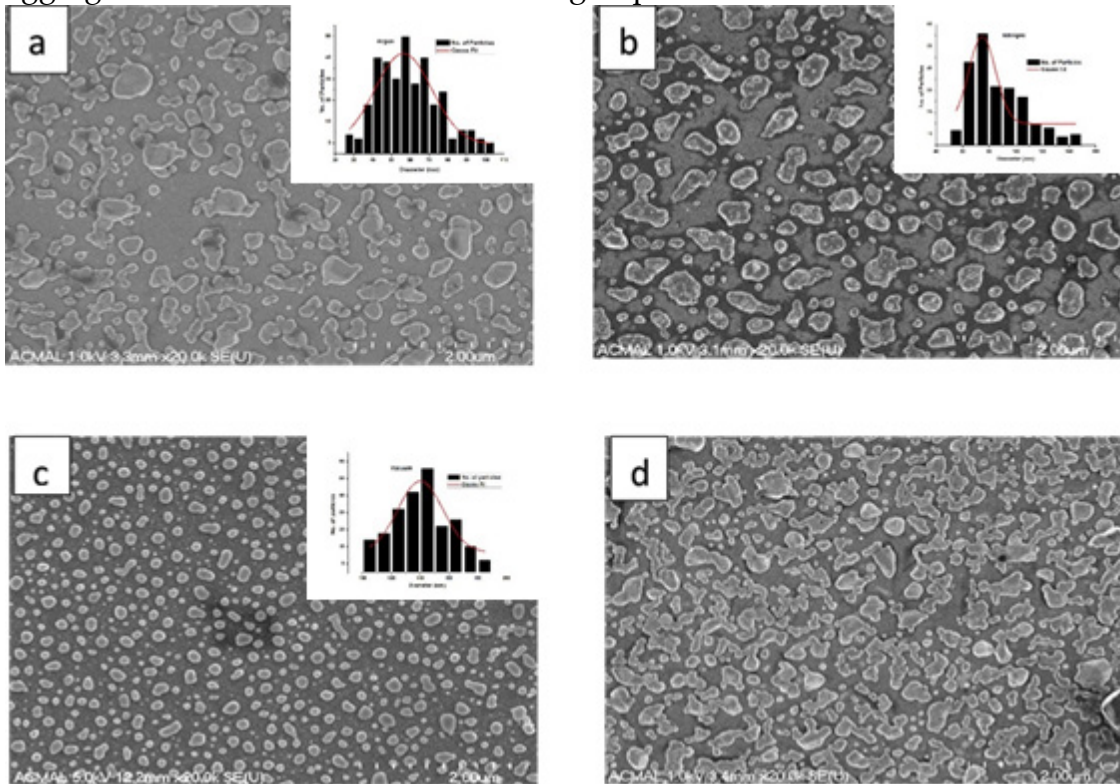
Figure 6.1: SEM images showing particle distribution for Ag/ITO/glass samples annealed at 180°C in; (a) Argon (b) Nitrogen (c) Vacuum and (d) as-deposited.

To facilitate the statistical analysis of the nanostructure size, the Ag nanoparticles were approximated to be a spherical whole. The size histogram of the samples shows that the size variation ranges from around 35 - 105 nm for Ar processed nanostructures, 50 – 150 nm for N_2 processed nanostructures and 100 – 190 nm for vacuum processed nanoparticles. Results show that Ag nanostructures processed under Ar ambient conditions had the largest size variation and hence the most multi-disperse nanoparticles. There is less size variance for the NPs processed

91

under N_2 and vacuum ambient. The SEM analysis results, together with the XRD, UV-Vis average transmittances and Tauc plot results are summarized in Table 6.1.

Table 6.1. Summary of SEM, XRD, UV-Vis and Tauc plot analysis showing average; particle and grain size, transmittance and electronic band gap for samples processed in varied ambience.

Processing/ Ambient	SEM		XRD		UV-Vis	
	Particle size (nm)	Standard Deviation (nm)	2θ (degree)	Grain size (nm)	Average Transmittance (400-800 nm)%	Band gap (ev)
Argon	56.36	15.12	38.244	19.772	52.28	3.746
Nitrogen	74.74	13.42	38.184	19.726	77.05	3.661
Vacuum	140.12	15.61	38.114	19.428	44.48	3.585

6.3.2 AFM Analysis

The AFM results were used to complement the SEM analysis and sample results are shown in Fig. 6.2. Surface roughness analysis showed that the height of the particles varied from 12 nm to around 130 nm with a root mean roughness (RMS) of 24 nm. This means the NPs can be approximated to be hemispherical in shape since their diameters range from 60 nm to 200 nm.
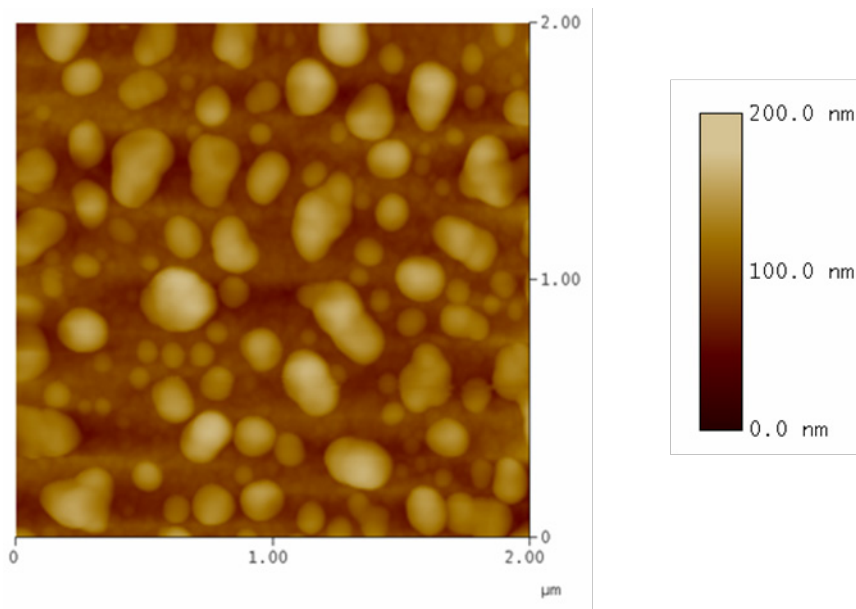
Figure 6.2. AFM images showing vacuum annealed AgNPs on ITO/glass substrate at 150 ^{0}C. Image scale is 200 nm.

6.4. Optical Properties

6.4.1. UV-Vis Spectroscopy

Fig. 6.3 below shows the variation of AgNPs optical and electronic properties with processing ambient. Fig. 6.3. a) and b) in particular show how both the UV-Vis transmittance and reflectance are influenced by AgNPs processing ambient, while Fig. 6.3. c) and d) show the corresponding UV-Vis absorption spectra and the Tauc plot respectively for the same samples. Generally, the N_2 processed NPs exhibit the greatest transmittance while the least transmittance is observed for the vacuum annealed AgNPs. The low transmittance in the vacuum processed NPs can be attributed to the presence of vacancies whilst these vacancies are filled by N_2 atoms for the N_2 processed AgNPs, hence the high transmittance is observed for N_2 annealed samples. The presence of large NPs with a high surface coverage for vacuum processed samples may result in the AgNPs having a shading effect resulting in low transmittance values. There is a general correlation between the transmittance and reflectance spectra as seen in both Fig. 6.3. a) and b).
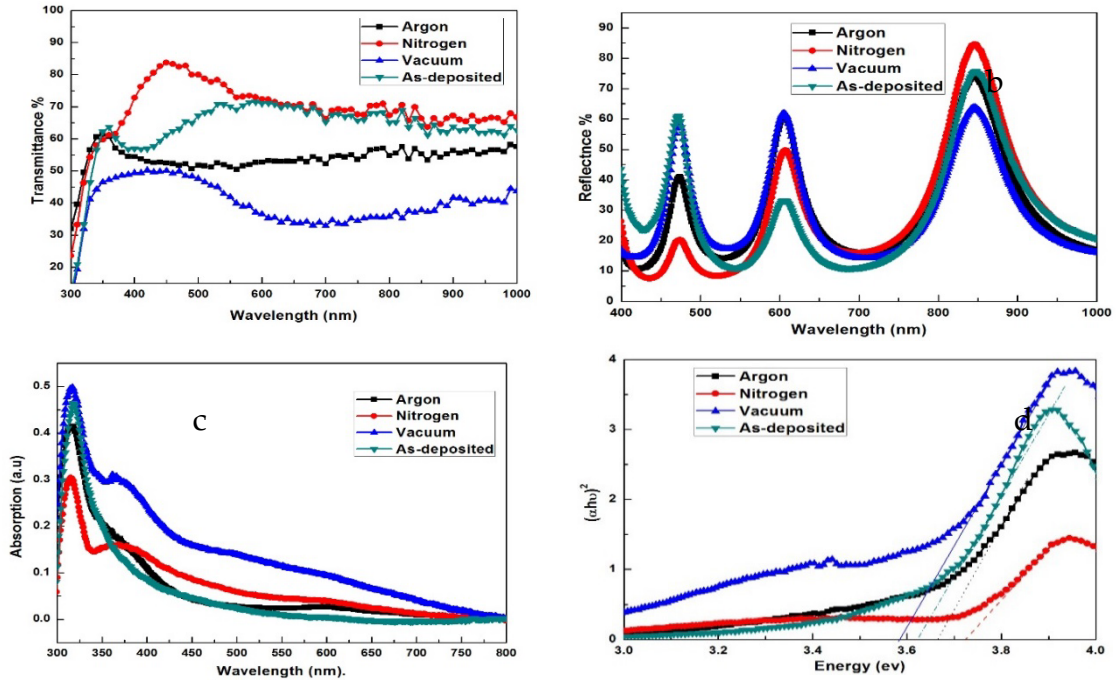
Figure 6.3. Ambient dependence of optical and electronic properties for AgNPs; a) transmittance, b) reflectance, c) UV-Vis absorption spectra, and d) Tauc plot for argon, nitrogen, vacuum and as-deposited samples.

The UV-Vis spectra (Fig.6.3. c) shows the silver on ITO peak around 315 nm, which exists in all samples. This is unusual for Ag since generally this peak is expected to be around 350 nm and can red-shift further depending on the substrate. There is a visible small peak near 370 nm for vacuum and nitrogen annealed indicating the absorption peak due to the presence of different sized particles. There is generally no marked difference in the NPs absorption spectra despite that the vacuum processed AgNPs show the greatest absorbance in the 300 nm – 700 nm. The absorption peak position of Ag/ITO/glass film is close to the position of the ITO film absorption peak which occurs around 340 nm, however, there is a slight blue shift and peak 'flattening' for all Ag NPs except for the Ar processed NPs which has a broad peak around 600 nm. The band gap is estimated from the absorption spectra using Tauc plot shown in Fig. 6.3. d). The optical band gap is observed to be around 3.6 eV for all samples and shows a strong dependence on the carrier concentration of the film. The presence of the broad absorption peak around the 500 - 700 nm region for Ar processed AgNPs indicates great light harvesting potential in those regions to assist PV response.

94

6.4. SERS Analysis

Methylene blue (MB) was used as analyte to study the Raman activities of the prepared as-deposited and Ag/ITO annealed under different ambient conditions (argon, nitrogen and vacuum) using a 633 nm laser as the excitation signal. Fig. 6.4 shows the SERS spectra response for MB adsorbed on as-deposited Ag/ITO/glass and AgNPs processed at 180 ^{0}C. The main absorption peaks of the MB solution are located at around 610 and 293 nm (not shown) indicating that all peaks are away from the excitation wavelength, thus the resonant Raman Effect is normally expected to be too weak [38] to be observed due to its low concentration and are buried by the Raman scattering arising from the solvent. The SERS results show the presence of a broad peak at 420 cm^{-1} for only the vacuum annealed AgNPs sample indicating the predominant presence of large particle size (140 nm on average) in this sample. AgNPs processed under argon ambient shows the greatest SERS response around 1348 and 1575 cm^{-1} which is almost twice the response for nitrogen and vacuum annealed nanoparticles. The presence of the broad UV-Vis absorption peak (Fig. 6.3. c) observed only for this sample, can be attributed to be responsible for the corresponding observed intensity enhancement for Ar processed AgNPs. The results further show that there is no enhancement for the as-deposited samples. This may be attributed to the absence of finite shape and distance between two nanoparticles/ clusters, which is one of the requirement for the SERS enhancement.
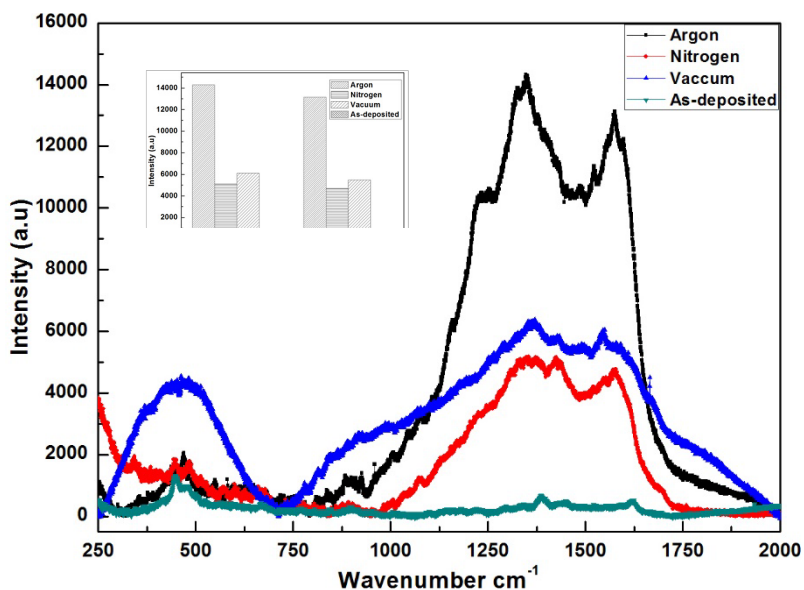
Figure 6.4. SERS of Ag/ITO/glass samples (argon, nitrogen, vacuum annealed and as-deposited) and their intensity variation. Insert: peak intensity variation.

6.5. Structural Analysis

6.5.1. XRD Analysis
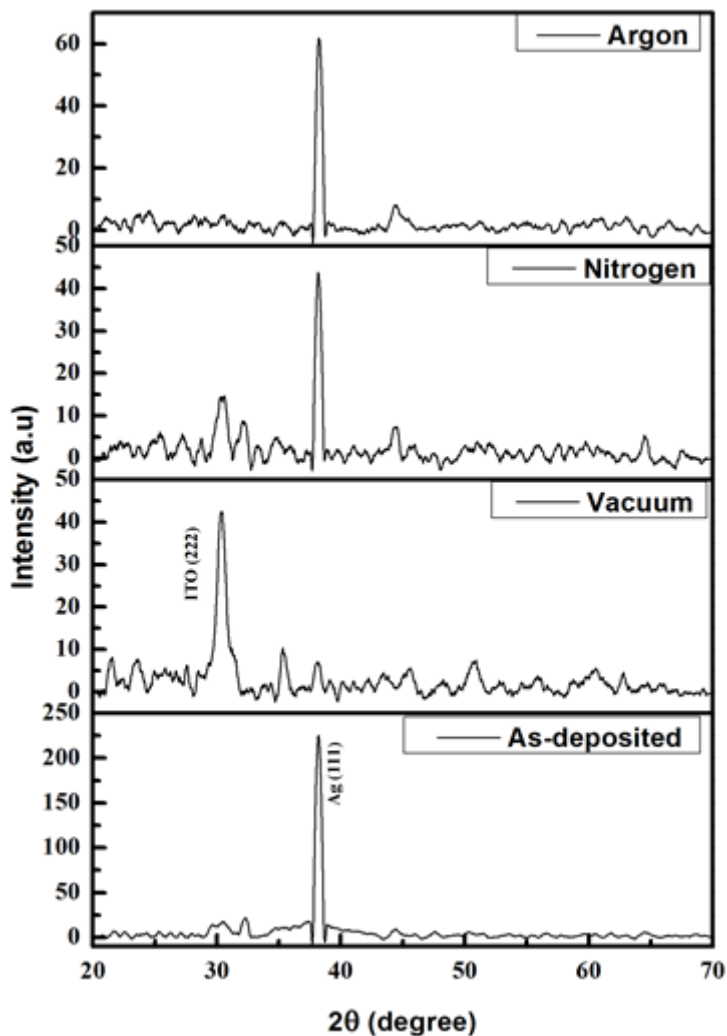
Figure 6.5. XRD analysis for argon, nitrogen, and vacuum annealed (180⁰C) and as-deposited samples of AgNPs on glass substrate.

The crystalline structure was confirmed by the XRD diffraction measurements as can be seen in Fig 6.5. The XRD analysis results for both as-deposited and processed AgNPs/ ITO/glass show a clear crystalline structure for all samples. The dominant peak at 38.2° is for Ag (111) and is present in all study samples. For the case of vacuum processed NPs, the intensity of the 38.2° peak is low and the high intensity peak at 30.3° corresponds to ITO (222). The same ITO peak can be seen for the nitrogen processed samples although its intensity is much less compared to peak intensity observed for the vacuum annealed samples. This could be

attributed to the separation distance between the two nanoparticles/clusters and the finite shape both of which are absent for the Ar processed and as-deposited samples. There are also some submissive peaks for Ag visible at 44.4° (200) and 64.6° (220) in all samples and other submissive peaks at 21.5°, 35.4° and 55.8° visible in nitrogen and vacuum processed samples corresponding to ITO (211), (400) and (611) planes respectively. The average grain size for all samples summarized in Table 1 were determined from the Debye-Scherrer formula for Ag particle to be around 19.7 nm.

6.6. Modeling and theoretical analysis

In order to study the details of optical response of the structure and predict the behavior of the NPs in different situations a numerical study has been performed. First, absorption spectra for mono-disperse nanoparticles with different particle sizes were modeled with a commercial full wave simulator a fully-vectorial finite element based software package COMSOL Multiphysics RF module v5.0 in frequency domain. The geometry consists of a thick glass substrate which has been coated with 70nm thick ITO film. The mono-disperse nano-particles was modeled by a periodic array of metallic hemispheres on top the ITO film, see Fig. 6.6. a). The absorbed power in the metallic hemispheres was found for the case of normal incident plane wave ranging from 300nm to 730nm.
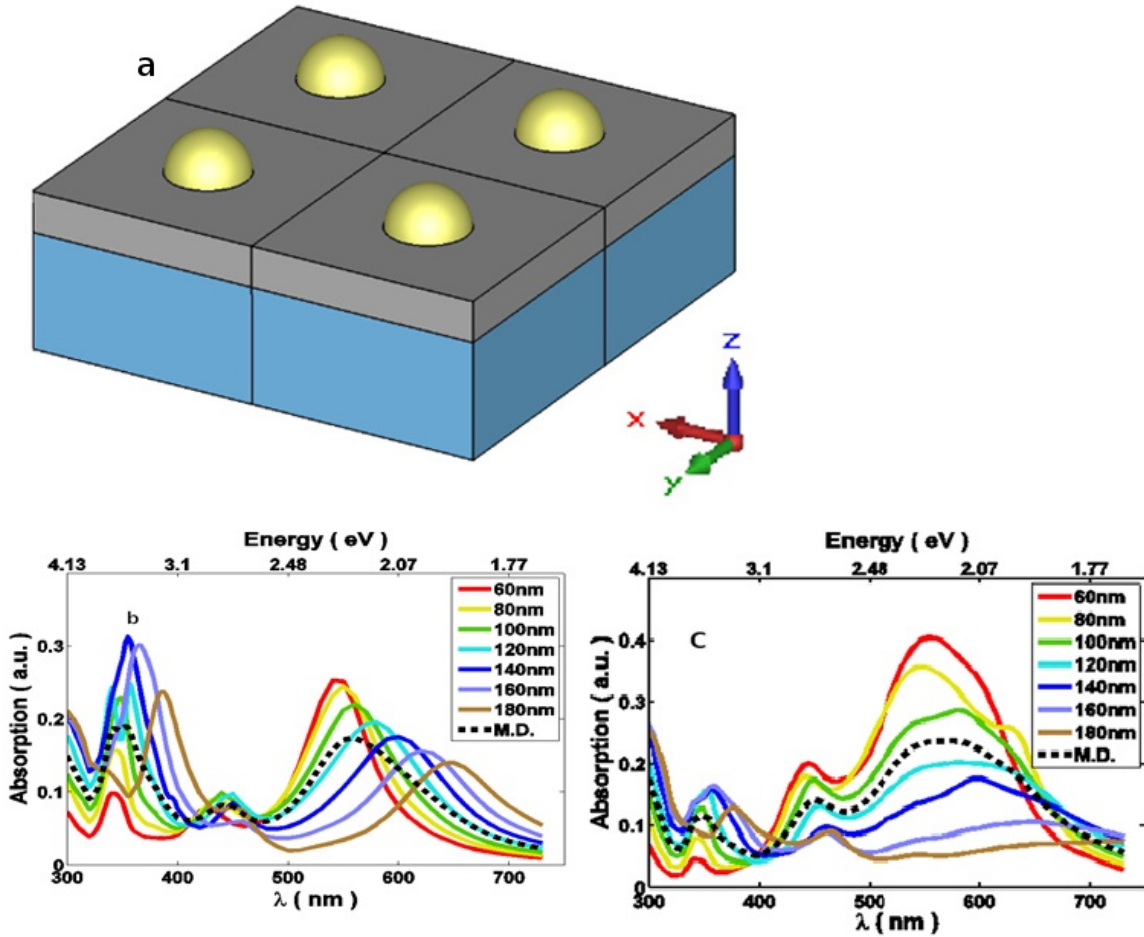
Figure 6.6. a) The geometry used to model the mono-disperse AgNPs. Blue shows the glass substrate, ITO is illustrated by the gray layer, and the gold hemispheres represent the NPs and b) Absorption spectra for mono-disperse and multi-disperse nanoparticles on glass substrate. Particle size range from 60 nm to 180 nm. c). Absorption spectra for mono-disperse and multi-disperse nanoparticles on a-Si:H substrate. Particle size range from 60 nm to 180 nm.

The absorption spectrum for multi-disperse NPs was calculated by summing over the absorption spectra of the mono disperse AgNPs with different particle size, each one weighted with the corresponding relative population in the ensemble. Fig. 6.6. b) and c) show the absorption spectra of mono and multi-disperse AgNPs corresponding to a 18.5 nm thick Ag film annealed in vacuum. The simulation results (Fig. 6.6. b) and c) are in agreement with the UV – Vis absorption spectrum experimental data shown in Fig. 6.3 (c).

It is well known that the efficiency of a-Si:H thin film solar cell drops drastically at high wave length (600 nm and greater), because of low absorption of the active intrinsic a-Si:H layer. Several approaches have been proposed to enhance the efficiency of a-Si:H at high wavelengths by incorporating NPs within the cell.

Although the improvement in overall device performance is due to contributions from different phenomena such as; diffraction, EM field enhancement, and light trapping mechanisms, for effective absorption in the higher wavelength region, the NPs must resonate at one or more frequencies within this region. It is therefore, crucial that the multi-disperse nanoparticles prepared by the method described in this paper exhibit resonances within the region of interest when incorporated in a-Si:H thin film solar cell.

To investigate the effect of the substrate on the NPs resonances, the model file was updated to a-Si:H as the substrate and the same procedure described earlier was repeated to obtain the absorption spectra of multi-disperse different size AgNPs on a-Si:H substrate. Fig. 6.6. (c) shows the absorption spectra of mono and multi-disperse NPs on a-Si:H substrate with 70 nm ITO spacer layer. Red-shift of NPs resonance frequency in response to increase in refractive index of the substrate has been studied extensively [42-45]. In the case of multi-disperse NPs, as shown by the simulation results (Fig. 6.6. (c), the resonance frequency of AgNPs shifts from 350 nm to around 600 nm and at the same time the resonance became broader which is very appealing for plasmonic solar cell application [46; 19-23].

6.7. Conclusion

In this study, AgNPs of different sizes and surface coverage were synthesized using ambient dependent agglomeration of e-beam evaporated silver thin-films (18.5 – 25 nm). The influence of different processing ambient conditions were observed on both NPs morphology and optical properties. Results here show conditions to obtain the greatest SERS intensity enhancement of up to 14 times is possible for 18.5 nm Ag films samples processed in argon ambient relative to vacuum processed films. Further results from simulations on NPs optical response consolidate the observed experimental data. A strong correlation is observed between processing conditions, particle sizes, shapes and their optical response (both UV-vis absorption and SERS). From the results it can be inferred the separation distance between NPs is more crucial for enhancement than the NPs are comprised of only spherical shapes. The high plasmonic enhancement in SERS occurs when the separation distance between the two particles is minimum (less than 20nm).

There is a clear observed relationship between particle size and resonance frequency indicated by the red-shifting of resonances with increasing particle size. XRD analysis reveals both the presents of polycrystalline bcc ITO and fcc Ag. No Ag-Sn phases are observed in the results showing that there was no alloying between the Ag and Sn (from ITO) during the annealing process. The ability to

mass-fabricate NPs economically, and the ability to deliberately tailor their optical response through the use of different ambient conditions presents greater opportunities for targeted application areas such as thin film PV devices, plasmonic photo-thermal therapy (PPTT) and plasmonic sensing.

Acknowledgements

References

1. J. Bischof, D. Scherer, S. Herminghaus, P. Leiderer. Dewetting modes of thin metallic films: nucleation of holes and spinodal dewetting.*Physical review letters*, *77*(8), p.1536 (1996).
2. D.J Srolovitz, M.G. Goldiner. The thermodynamics and kinetics of film agglomeration. *JOM*, *47*(3), pp.31-36(1995).
3. C.V. Thompson. Solid-state dewetting of thin films. *Annual Review of Materials Research*, *42*, pp.399-434(2012).
4. H. Krishna, R. Sachan, J. Strader, C. Favazza, M. Khenner, R. Kalyanaraman. Thickness-dependent spontaneous dewetting morphology of ultrathin Ag films. *Nanotechnology*, *21*(15), p.155601(2010).
5. S. Herminghaus, K. Jacobs, K. Mecke, J. Bischof, A. Fery, M. Ibn-Elhaj, S. Schlagowski. Spinodal dewetting in liquid crystal and liquid metal films. *Science*, *282*(5390), pp.916-919 (1998).
6. A., Atena, M. Khenner. Thermocapillary effects in driven dewetting and self assembly of pulsed-laser-irradiated metallic films. *Physical Review B*, *80*(7), p.075402 (2009).
7. C., Favazza, R. Kalyanaraman, R. Sureshkumar. Robust nanopatterning by laser-induced dewetting of metal nanofilms.*Nanotechnology*, *17*(16), p.4229 (2006).
8. J. Trice, C. Favazza, D. Thomas, H. Garcia, R. Kalyanaraman, R. Sureshkumar. Novel self-organization mechanism in ultrathin liquid films: theory and experiment. *Physical review letters*, *101*(1), p.017802(2008).
9. Y.F. Guan, R.C. Pearce, A.V. Melechko, D.K. Hensley, M.L. Simpson, P.D. Rack. Pulsed laser dewetting of nickel catalyst for carbon nanofiber growth. *Nanotechnology*, *19*(23), p.235604 (2008).

10. J. Boneberg, A. Habenicht, D. Benner, P. Leiderer, M. Trautvetter, C. Pfahler, A. Plettl, P. Ziemann,. Jumping nanodroplets: A new route towards metallic nano-particles. *Applied Physics A*, *93*(2), pp.415-419(2008).

11. R., Liu, F., Zhang, C., Con, B. Cui, B., Sun. Lithography-free fabrication of silicon nanowire and nanohole arrays by metal-assisted chemical etching. *Nanoscale research letters*, *8*(1), pp.1-8 (2013).

12. M., Quinten, A., Leitner, J.R. Krenn, F.R., Aussenegg. Electromagnetic energy transport via linear chains of silver nanoparticles.*Optics letters*, *23*(17), pp.1331-1333 (1998).

13. K.A. Willets, and R.P. Van Duyne. Localized surface plasmon resonance spectroscopy and sensing. *Annu. Rev. Phys. Chem.*, *58*, pp.267-297 (2007).

14. D.L. Jeanmaire, and R.P., Van Duyne. Surface Raman spectroelectrochemistry: Part I. Heterocyclic, aromatic, and aliphatic amines adsorbed on the anodized silver electrode. *Journal of Electroanalytical Chemistry and Interfacial Electrochemistry*, *84*(1), pp.1-20 (1977).

15. C.L., Haynes, C.R., Yonzon, X. Zhang, R.P., Van Duyne. Surface-enhanced Raman sensors: Early history and the development of sensors for quantitative biowarfare agent and glucose detection. *Journal of Raman Spectroscopy*, *36*(6-7), pp.471-484 (2005).

16. G.C., Schatz, M.A, Young, R.P. Van Duyne, K. Kneipp, M. Moskovits, H. Kneipp. Berlin: SpringerVerlag 19 46 (2006).

17. C.R., Yonzon, C.L., Haynes, X., Zhang, J.T. Walsh, and R.P., Van Duyne. A glucose biosensor based on surface-enhanced Raman scattering: Improved partition layer, temporal stability, reversibility, and resistance to serum protein interference. *Analytical Chemistry*, *76*(1), pp.78-85 (2004).

18. E.J. Zeman, and G.C., Schatz. An accurate electromagnetic theory study of surface enhancement factors for silver, gold, copper, lithium, sodium, aluminum, gallium, indium, zinc, and cadmium. *Journal of Physical Chemistry*, *91*(3), pp.634-643 (1987).

19. H.A., Atwater and A., Polman. Plasmonics for improved photovoltaic devices. *Nature materials*, *9*(3), pp.205-213 (2010).

20. S., Pillai, K.R., Catchpole, T. Trupke, and M.A., Green. Surface plasmon enhanced silicon solar cells. *Journal of applied physics*, *101*(9), p.093105 (2007).

21. K.R., Catchpole, and A., Polman. Design principles for particle plasmon enhanced solar cells. *Applied Physics Letters*, *93*(19), p.191113 (2008).

22. F.J., Beck, A., Polman, and K.R., Catchpole. Tunable light trapping for solar cells using localized surface plasmons. *Journal of Applied Physics*,*105*(11), p.114310 (2009).

23. J., Gwamuri, D.Ö., Güney, and J.M., Pearce. Advances in Plasmonic Light Trapping in Thin-Film Solar Photovoltaic Devices. *Solar cell nanotechnology*, pp.241-269 (2013).

24. A., Vora, J., Gwamuri, N., Pala, A., Kulkarni, J.M. Pearce, and D.Ö., Güney. Exchanging ohmic losses in metamaterial absorbers with useful optical absorption for photovoltaics. *Scientific reports*, *4 (*2014).

25. A., Vora, J., Gwamuri, J.M., Pearce, P.L., Bergstrom, and D.Ö., Güney. Multi-resonant silver nano-disk patterned thin film hydrogenated amorphous silicon solar cells for Staebler-Wronski effect compensation.*Journal of Applied Physics*, *116*(9), p.093103 (2014).

26. F.J., Tsai, J.Y., Wang, J.J., Huang, Y.W., Kiang, and C.C., Yang. Absorption enhancement of an amorphous Si solar cell through surface plasmon-induced scattering with metal nanoparticles. *Optics express*,*18*(102), pp.A207-A220 (2010).

27. R., Santbergen, T.L., Temple, R., Liang, A.H.M., Smets, R.A.C.M.M. Van Swaaij, and M., Zeman. Application of plasmonic silver island films in thin-film silicon solar cells. *Journal of Optics*, *14*(2), p.024010 (2012).

28. R., Santbergen, R., Liang and M., Zeman. A-Si: H solar cells with embedded silver nanoparticles. In *Photovoltaic Specialists Conference (PVSC), 2010 35th IEEE* (pp. 000748-000753) (2010).

29. A., Lin, S.M., Fu, Y.K., Chung, S.Y., Lai and C.W., Tseng. An optimized surface plasmon photovoltaic structure using energy transfer between discrete nano-particles. *Optics express*, *21*(101), pp.A131-A145 (2013).

30. F.J., Beck, S., Mokkapati, A., Polman and K.R., Catchpole. Asymmetry in photocurrent enhancement by plasmonic nanoparticle arrays located on the front or on the rear of solar cells. *Applied Physics Letters*,*96*(3), p.033113 (2010).

31. X., Chen, B., Jia, J.K., Saha, B., Cai, N., Stokes, Q., Qiao, Y., Wang, Z., Shi, and M., Gu. Broadband enhancement in thin-film amorphous silicon solar cells enabled by nucleated silver nanoparticles. *Nano letters*, *12*(5), pp.2187-2192 (2012).

32. C., Langhammer, B., Kasemo, and I., Zorić. Absorption and scattering of light by Pt, Pd, Ag, and Au nanodisks: Absolute cross sections and branching ratios. *The Journal of chemical physics*, *126*(19), p.194702 (2007).

33. S.A. Knickerbocker, Ph.D. Dissertation, Michigan Technological University, (1995).

34. T.S. Lim, M.S. Thesis, Michigan Technological University, (1997).

35. J., Gwamuri, A., Vora, R.R., Khanal, A.B., Phillips, M.J., Heben, D.O., Guney, P., Bergstrom, A., Kulkarni and J.M., Pearce. Limitations of ultra-thin transparent conducting oxides for integration into plasmonic-enhanced thin-film solar photovoltaic devices. *Materials for Renewable and Sustainable Energy*, *4*(3), pp.1-11 (2015).

36. J., Gwamuri, M., Marikkannan, J., Mayandi, P.K. Bowen and J.M., Pearce. Influence of Oxygen Concentration on the Performance of Ultra-Thin RF Magnetron Sputter Deposited Indium Tin Oxide Films as a Top Electrode for Photovoltaic Devices. *Materials*, *9*(1), p.63 (2016).

37. J., Gwamuri, A., Vora, J., Mayandi, D.Ö., Güney, P.L., Bergstrom and J.M., Pearce. A new method of preparing highly conductive ultra-thin indium tin oxide for plasmonic-enhanced thin film solar photovoltaic devices.*Solar Energy Materials and Solar Cells*, *149*, pp.250-257 (2016).

38. G.N. Xiao and S.Q., Man. Surface-enhanced Raman scattering of methylene blue adsorbed on cap-shaped silver nanoparticles. *Chemical Physics Letters*, *447*(4), pp.305-309 (2007).

39. Zhang JZ. Optical properties of metal nanomaterial. In: Optical properties and spectroscopy of nanomaterials. World Scientific Publishing Company, Inc. pp. 205-235 (2009).

40. I., Hotovy, J., Pezoldt, M., Kadlecikova, T., Kups, L., Spiess, J., Breza, E., Sakalauskas, R., Goldhahn and V., Rehacek. Structural characterization of sputtered indium oxide films deposited at room temperature. *Thin Solid Films*, *518*(16), pp.4508-4511.41 (2010).

41. J., Yun, W., Wang, T.S., Bae, Y.H., Park, Y.C., Kang, D.H., Kim, S., Lee, G.H., Lee, M., Song and J.W., Kang. Preparation of flexible organic solar cells with highly conductive and transparent metal-oxide multilayer electrodes based on silver oxide. *ACS applied materials & interfaces*, *5*(20), pp.9933-9941 (2013).

42. L. J. Sherry, S.-H. Chang, G. C. Schatz, R. P. Van Duyne, B. J. Wiley, and Y. Xia, "Localized surface plasmon resonance spectroscopy of single silver nanocubes," Nano Letters, vol. 5, no. 10, pp. 2034–2038, 2005

43. L. J. Sherry, R. Jin, C. A. Mirkin, G. C. Schatz, and R. P. Van Duyne, "Localized surface plasmon resonance spectroscopy of single silver triangular nanoprisms," Nano Letters, vol. 6, no. 9, pp. 2060–2065, 2006

44. K. L. Kelly, E. Coronado, L. L. Zhao, and G. C. Schatz, "The optical properties of metal nanoparticles: the influence of size, shape, and dielectric environment," Journal of Physical Chemistry B, vol. 107, no. 3, pp. 668–677, 2003.

45. O. Kvítek, J. Siegel, V. Hnatowicz, and V. Švorčík, "Noble Metal Nanostructures Influence of Structure and Environment on Their Optical Properties", Journal of Nanomaterials, Volume 2013 (2013), Article ID 743684.

46. P., Spinelli, V.E., Ferry, J., Van de Groep M., Van Lare, M.A., Verschuuren, R.E.I., Schropp, H.A., Atwater, and A., Polman. Plasmonic light trapping in thin-film Si solar cells. *Journal of Optics*, *14*(2), p.024002 (2012).

7. Plasmonic enhanced Hydrogenated Amorphous Silicon Photovoltaic Device Using Multi-disperse Self-Assemble Silver Nanoparticles [6].

7.1 Introduction

Solar photovoltaic (PV) energy conversion is a technically viable and sustainable solution to society's energy needs [1], but the levelized cost of electricity (LCOE) must continue to decline in order to reach mass deployment at the terrawatt scale [2]. Hydrogenated amorphous silicon (a-Si:H) is an inexpensive and readily available earth abundant [3] solar cell material, which has the capability for generating clean sustainable energy at the necessary scale [4-5]. PV cells made with a-Si:H have the fastest energy payback time of any Si-based PV device [6] and therefore combats the energy cannibalism effect that plagues any renewable energy industry that is in the rapid growth of production needed to supplant polluting fossil fuels [7]. Unfortunately, only one year after Carlson and Wronski invented the first a-Si:H based solar cell (1976) [8], Staebler and Wronski discovered significant light induced degradation of the electronic properties of a-Si:H [9]. When a-Si:H based solar cells are exposed to light, there is a decrease in their efficiency until a saturation value is reached (degraded steady state or DSS) due to an increase in the density of multiple types of defect states [10-15]. The ecological and economic promise of a-Si:H solar cells is thus incomplete because this Staebler-Wronski Effect (SWE) limits both the thickness of cells able to reach a DSS and the deposition rate for high-quality materials (and thus machine throughput and overall economics). The a-Si-H PV industry has engineered around SWE and obtained large area (>1m^2) modules that reach a DSS. This is done by growing thinner i-layers made up of protocrystalline materials [16-18] than would be used to garner the optimal conversion efficiency to limit SWE. Thinning the i-layer is also made possible without destroying the cells ability to capture most of the light by improved optical enhancement by combining two classical methods of (i) scattering from a top roughened anti-reflection coating and (ii) using a detached back reflector [19-20].

However, recent advances in optics provide a new method to improve the optical enhancement in a-Si:H PV devices and further reduce the negative effects of SWE. Resonant plasmonic nanostructures have been shown to allow for control of fundamental optical processes such as absorption, emission and refraction [21-27]. In addition, preliminary work on plasmonic nanostructures have been shown to

---

[6] The material contained in this chapter is to be submitted to the journal.

enhance the performance of PV devices by increasing light absorption [28-44] and theoretical work has indicated that the performance can be increased significantly [45-50].

To establish a more comprehensive understanding of resonant plasmonic nanostructures useful for creating a nanostructured 'black' perfect absorbers that can be integrated into the manufacture of a-Si:H PV devices, a plasmonic enhanced PV device was proposed, designed and investigated. First, experimental real-time spectroscopic ellipsometry (RTSE) data on the optical properties of the cells were used to perform theoretical simulations of cells with and without plasmonic nanostructures. Then the cells were characterized to determine their current-voltage (I –V) characteristics and quantum efficiency (QE). Next, as a way to keep the device fabrication process cost low, multi-disperse self-assemble silver nanoparticles were integrated on top of a superstrate configuration n-i-p a-Si:H commercial grade solar cell without altering the device semiconductor layer parameters. The cells were characterized again with I-V and QE and the results are discussed.

7.2 Experimental Details

Cell samples were deposited using a load-locked RF (13.56 MHz) PECVD cluster tool reactor (MVSystems.Inc) onto 6″ × 6″ borosilicate glass substrates. The glass substrates were pre-cleaned in an ultrasonic bath and air dried in nitrogen gas before being sputter coated with a back reflector (BR). The BR and subsequent device layer were deposited following a recipe described in ref [51] to obtain a device structure shown in Fig 7.1. The device fabrication was done using the same equipment and the processing parameters detailed in the same ref above.
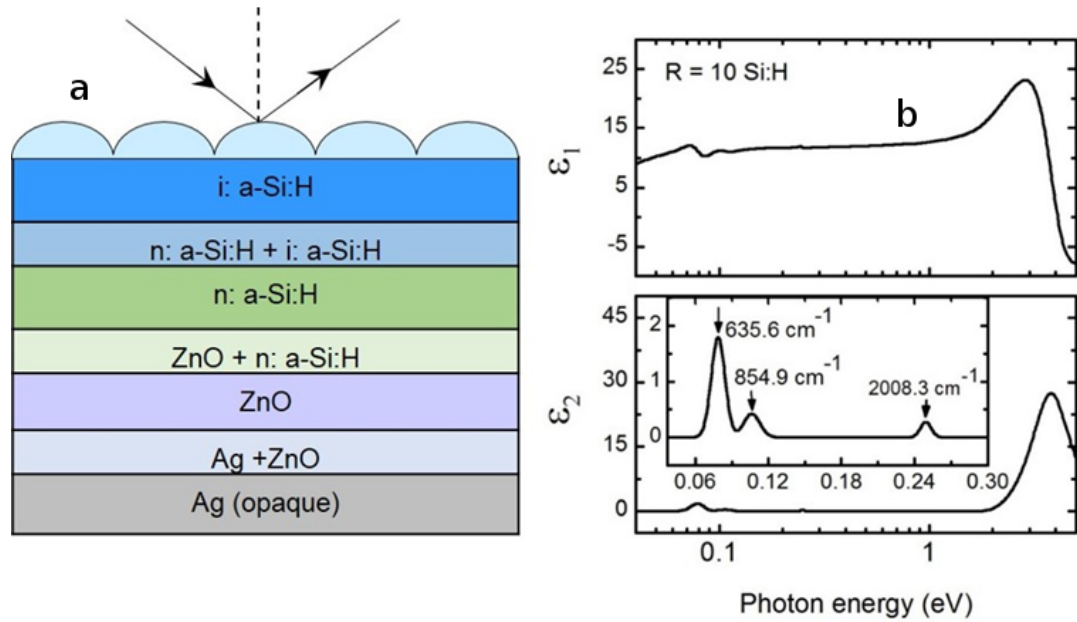
Figure 7.1. (a). A substrate n-i-p a-Si:H based PV device structure, and (b). Spectra in ε (top panel, real part ε_1; bottom panel, imaginary part ε_2) extracted over a spectral range from 0.04 to 5 eV for 3621 ± 2 Å, R = 10 a-Si:H films on BR over-coated with a R = 50 n-layer. The inset shows lower energy features in ε_2 as a function of photon energy representing Si-Hn vibrational modes as modeled by Gaussian oscillators. [51] (*CC BY licence*).

The devices were mapped, and characterized for I – V and QE before the beginning of the NPs integration process. The AgNPs integration process involved depositing thin layers of Ag film on top of the n-i-p a-Si:H device using e-beam evaporation technique (Federick system EB 12) and the dep-rate was kept constant at 0.8 A^0/s. Samples were then annealed in vacuum for at least two hours at 150 ^{0}C together control sample cells. The details on SANPs are outlined in ref [52]. The n-i-p a-Si:H device with AgNPs is shown in Fig. 7.2.(a) and (b), the improved predicted absorbance in the i-layer of the NDPSC [50] compared to the absorbance in the reference cell. QE measurements were performed using a QE system (PV Measurements model QEX10) without using bias light and I – V characterization was done using a small area solar simulator (PV Measurements model SASS, class - BBA). A calibrated photovoltaic reference cell (model #RCSiG2) was used to calibrate the solar simulator prior to performing I- V measurements. Data acquisition was done using a Keithley 4200 semiconductor characterization system integrated with micro manipulator probes. Device characterization was done twice: before the integration of the NPs and after the AgNPs were integrated onto the cells. In both cases only the test device was exposed to light and the rest were shielded. Exposure times of the test devices were further minimized by shuttering

the light as soon as the testing is completed to avoid SWE. All measurements were performed in triplicate.
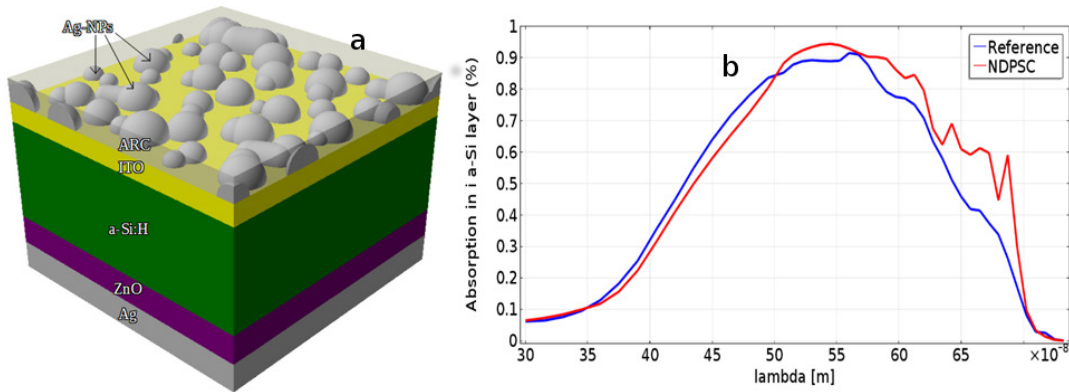

Figure 7.2.   (a). Plasmonic solar cell structure with multi-disperse AgNPs and, (b). Absorbance for the NDPSC i-a-Si:H layer versus the absorbance for the reference cell without NPs.

7.3. Results and Discussion

Quantum efficiency measurements for the reference device, the test device (with NPs) and the control device are shown in Fig. 7.3 below. Fig. 7.3.(a) represent the control cell used to monitor the effect of annealing on device performance. It is evident from the control Cell (CC) that there is negligible degradation of the device due to annealing which is a process used to achieve self-assemble NPs. The results reported here are for samples annealed at 150 ^{0}C for 2 hours in a vacuum. The greatest variation in QE before and after annealing was observed to be 0.19% which occurs at the wavelength of 520 nm for the control cell otherwise generally the devices were observed to be quite stable under the processing conditions used.

Fig. 7.3. (b). shows the how the QE of the cell varied after the integration of the NPs. Evidently, the maximum QE was observed to decrease from an initial value of about 40% for the reference cell to about 20% after AgNPs added to the device. The decrease was attributed to the both the size and surface coverage of the NPs. The NPs produce by agglomeration of 18 nm thick film of silver in a vacuum for 2 hours at 150 ^{0}C were observed to have a size range from 80 nm to 180 nm. The bigger NPs and their high surface coverage density had the shading effect on the cells resulting in reduced QE values. The Jsc were also observed to drop in the same manner as the QE. The effect of NPs on both Jsc and Voc can be seen by comparing the ref cell to the test device. After the addition of the NPs, the Jsc value fell from 0.68 mA to 0.4 mA whilst the Voc changed from 0.8 V to 0.74 V.
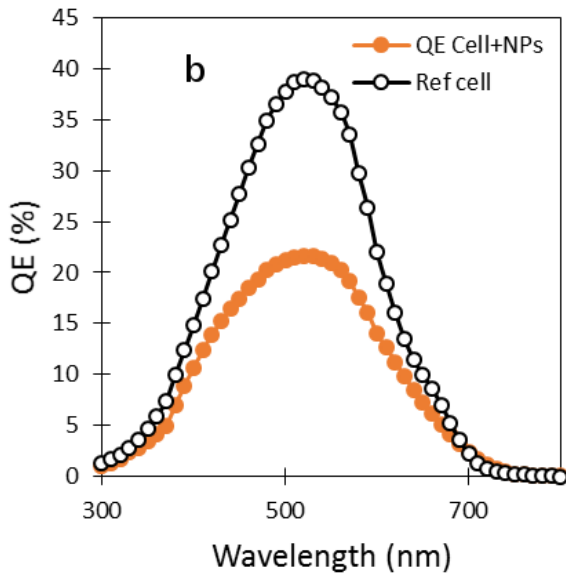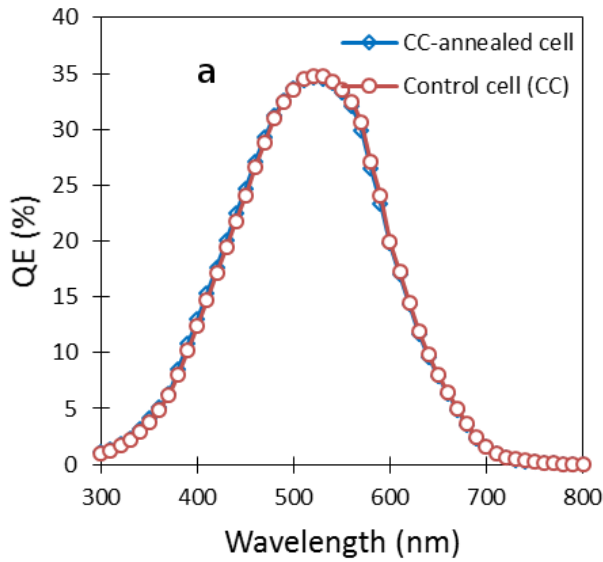
Figure 7.3. Variation of QE with wavelength for; (a). Control cell before and after annealing at 150 0C for 2 hours and (b), reference cell, and the test cell (ref with NPs after annealing at 150 0C for 2 hours).

To try and control particle sizes, thinner (from 10 nm down to 3 nm) films of Ag were deposited and annealed under vacuum conditions and the cells were characterized. A trend was observed in which the QE increased with decreasing Ag starting film thickness. Fig. 7.4. (c) represent sample best case results from cells with a starting Ag film of 10 nm annealed at 150 0C for 2 hrs in vacuum. The maximum QE for the test cell (D02_1+NPs) was observed to be 20.2% from 520 – 540 nm compared to 19.9 % for the reference (D02_1) at 530 nm wavelength. After integration the area under the ref cell QE vs wavelength curve (4287.4 +- 96.33 a.u) with a FWHM of 196.23 was great than the test device curve area (4049.45 +- 74.66 a.u) with a FWHM of 182.51. The results from

multiple samples processed were all observed to be less than the measured performance for the reference cell and the best results (Fig. 7.4. (d)) are seen to approach the ref cell.
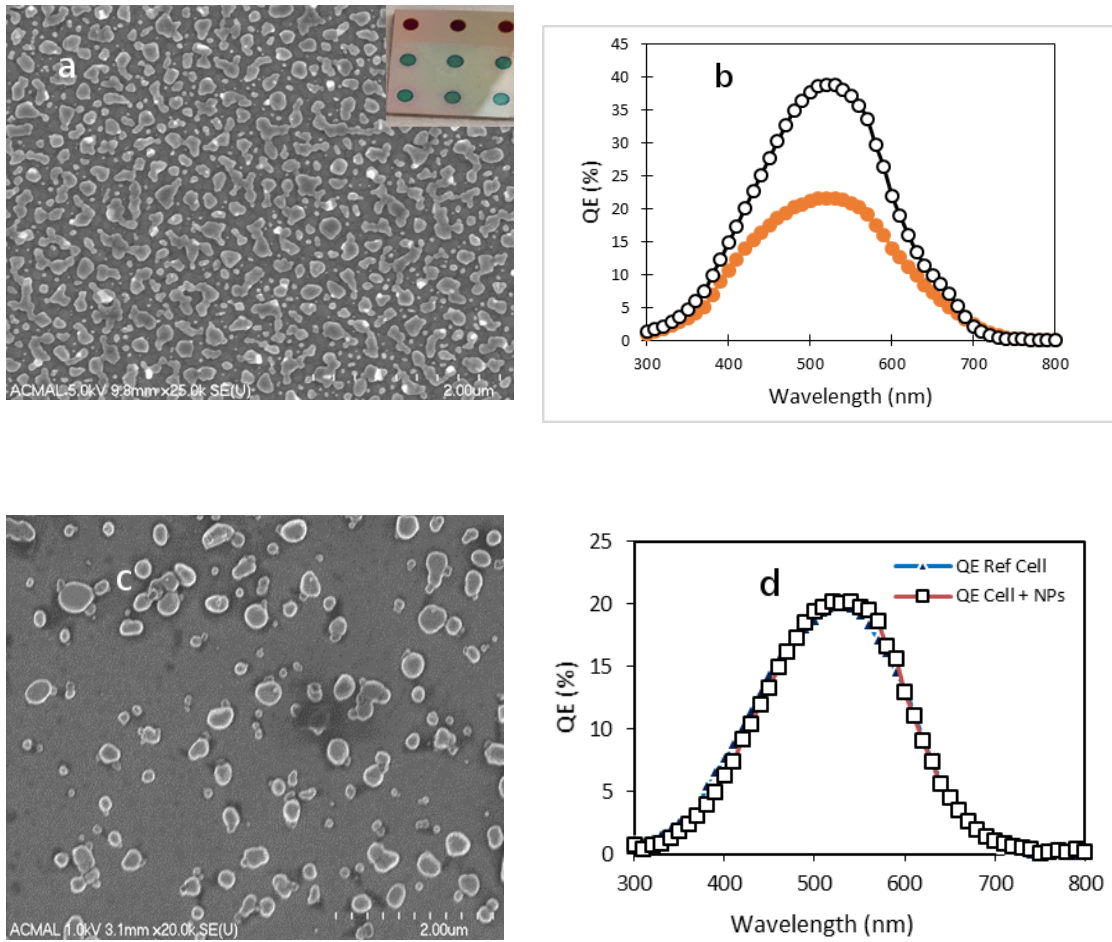
Figure 7.4 Effect of NPs surface coverage on the QE of a-Si:H devices. (a) SEM image showing Ag NPs on test device (solar cell). The high NPs surface density and large size have a shielding effect on the cell; (b) Corresponding QE vs wavelength for the test device compared to the ref device, (c) Test device with low NPs surface coverage density and (d). QE vs wavelength for the device shown in (c). Insert: Image of actual devices showing test devices (greenish) and control devices (brown).

To further probe the effect of varying NPs surface density of QE, test devices are etched in successive steps of 10 seconds up to 80 seconds using an ice cooled etchant solution (NH$_4$OH:H$_2$O$_2$) in a 9:1 ratio. Fig 7.5 shows the variation of QE with etching time for 10 s – 80 s etch. The ref and the as-processed test device (NPs only) are include for comparison purposes. Sample results presented here are for a single test device and indicate an improvement in the overall device QE with etch time up to 40 s. Fig. 7.5. (a) shows how the QE of as-processed device improves with etching time throughout the 300 – 800 nm wavelength range. Evidently the peak QE achieved through etching self-assemble AgNPs corresponds to the ref cell maximum QE. With further etching beyond 40 s, the QE of the etched device approaches that of the ref cell and plateaus thereafter as can be seen in Fig 7.5. (b).
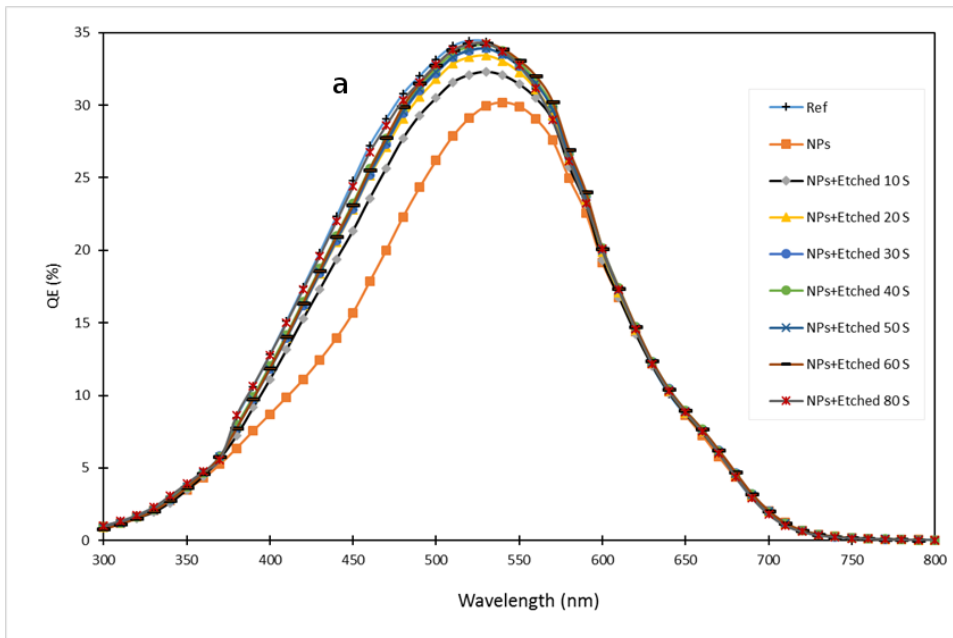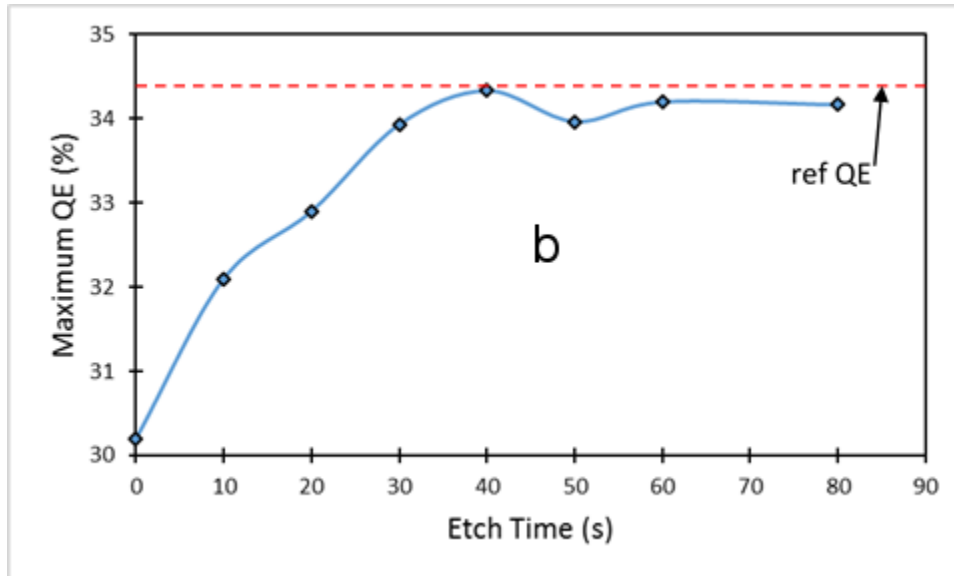
Figure 7.5. Effects of etching on QE for the test a-Si:H cell. (a). Variation of QE with wavelength in the 300 – 800 nm and, (b). Variation of maximum value of QE with etching time.

From these preliminary results it does not appear that agglomerated NPs provide the boost in QE expected from earlier simulations on well-organized uniform size and shape and spacing arrays of NPs. There are two primary challenges to the use of agglomerated NPs for this application. First there is an inherent difficulty in controlling NP size and surface distribution, both of which are critical for the successful realization of the plasmonic solar cell. In addition, as this method demands careful temperature control and monitoring to avoid permanent damage to the devices during processing of NPs optimal processing conditions are difficult to obtain. Based on the result of this preliminary work, further simulations were run.

Optical responses of the reference cell and multi-disperse AgNPs solar cell were obtained through a fully vectorial finite element based commercial software package COMSOL Multiphysics RF module v5.0b in frequency domain. For normal incidence response, both reference and multi-disperse solar cells were simulated using periodic boundary conditions for the vertical boundaries as described in ref [50]. The absorbance in individual layers was calculated from the power loss density function in COMSOL, and this absorbance in i-a-Si:H layer of solar cells was used to calculate theoretical absorbed power density in multi-disperse and reference structure, for incident AM 1.5 reference solar spectrum using the absorbed power density equation;

112

$$P_{i-a-Si:H}=\int A(\lambda)E_{AM1.5}(\lambda)d\lambda \tag{1}$$

where $P_{i-a-Si:H}$ is the absorbed power density (W/m^2) in the i-a-Si:H layer, $A(\lambda)$ is the absorbance in i-a-Si:H layer as a function of wavelength, and $E_{AM1.5}(\lambda)$ is the spectral irradiance as a function of wavelength (obtained from NREL [53].)

Figure. 7.6. shows the predicted absorbance in the device's i-layer when AgNPs size is varied from 80 – 160 nm in the visible range of the EM spectrum. The results from simulations predict less absorbance in the device active layer compared to the reference cell, when NPs are integrated to the device. These results are qualitatively in agreement with the measured experimental data as show by QE sample results in Fig. 7.5. This is in contrast with previous simulations which predicted an increased absorbance in i- layer of the a-Si:H solar cell due to the red-shifting of resonances in response to increase in refractive index of the substrate [Gwamuri et al, 2016]. The NPs resonances were also observed to be broader when the substrate is changed from ITO/glass to a-Si:H substrate which should result in broadband absorption in the PV device. It is therefore recommended that future work based on Ar annealing of Ag films in a controlled environment be pursued to achieve viable NPs for integration into thin-film solar cells. Also more work involving thinner films Ag starting films (less than 3 nm) is required.
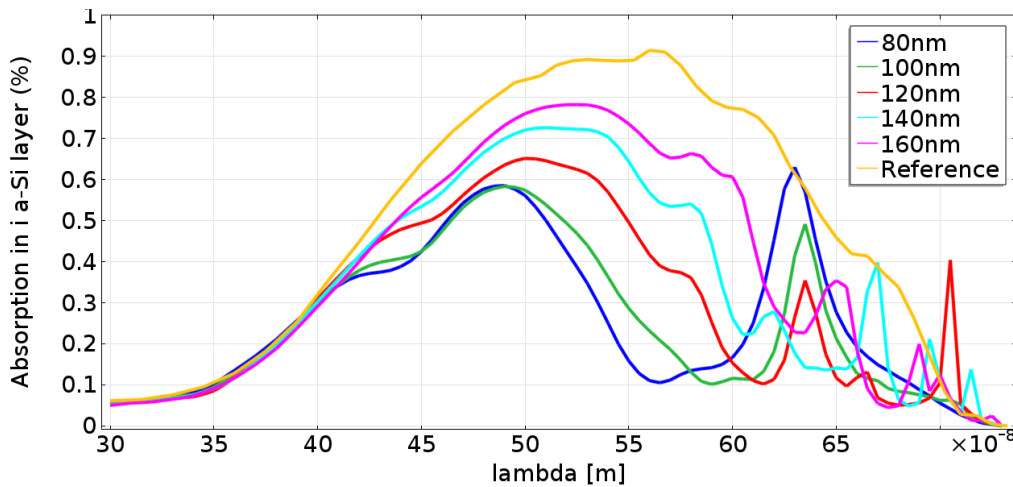
Figure 7.6. Predicted absorbance in i-a-Si:H layer for AgNPs with sizes range from 80 nm – 160 nm in the 300 – 750 nm wavelength range.

7.4. Conclusions

In this study, we have chosen a n-i-p a-Si:H cell commercial design with the intention to demonstrate the concept of achieving higher optical absorption (and subsequently higher OE), resulting in higher efficiency and SWE compensation. However devices used in this experiment were of inferior quality due to challenges

encountered during the fabrication process. Solar cell samples were characterized for both optical and electrical performance prior to the addition of NPs. For the purpose of this study, AgNPs were successfully integrated on PV devises via a well-established method of agglomeration of Ag ultra-thin films under vacuum conditions. Both I – V and QE characterization were performed on the fabricated devices. Current results does not show any improvement in solar cell samples performance after incorporating multi-disperse AgNPs, instead results indicate that the test devices are inferior to the reference device. NPs present a problem of shading on the test cells resulting in their decreased performance as evidenced by the effects of etching on QE of test devices. This in is agreement with the prediction from the simulations.

Acknowledgements

References

1. J. Pearce, Photovoltaics - A Path to Sustainable Futures. Futures 34(7), 663-674 (2002).
2. K. Branker, M. J.M. Pathak, J. M. Pearce, "A Review of Solar Photovoltaic Levelized Cost of Electricity", Renewable & Sustainable Energy Reviews 15, pp.4470-4482 (2011).
3. N.S. Lewis,. Research opportunities to advance solar energy utilization. Science, 351(6271), pp. 1920 (2016).
4. Wronski, C. R., J. M. Pearce, R. J. Koval, A. S. Ferlauto, and R. W. Collins. "Progress in amorphous silicon based solar cell technology." RIO 2 (2002): 6-11
5. Shah, Arvind, P. Torres, Reto Tscharner, N. Wyrsch, and H. Keppner. "Photovoltaic technology: the case for thin-film solar cells." science 285, no. 5428 (1999): 692-698.
6. J. Pearce, and A. Lau, "Net Energy Analysis For Sustainable Energy Production From Silicon Based Solar Cells", Proceedings of American Society of Mechanical Engineers Solar 2002: Sunrise on the Reliable Energy Economy, editor R. Cambell-Howe, 2002.

7. R. Kenny, Law, C. Pearce, J.M. "Towards Real Energy Economics: Energy Policy Driven by Life-Cycle Carbon Emission", Energy Policy 38, pp. 1969–1978, 2010.

8. D.E. Carlson, Wronski, C.R. Amorphous silicon solar cell. Appl. Phys. Lett., 28, p. 671 (1976).

9. D.L. Staebler, Wronski, C.R., Reversible conductivity changes in discharge-produced amorphous Si. Appl. Phys. Lett. 31, p. 292 (1977).

10. L. Yang, and Chen, L., "Fast" and "Slow" Metastable Defects in Hydrogenated Amorphous Silicon. Appl. Phys. Lett. 63, p. 400 (1993).

11. H. Fritzche, Development in Understanding and Controlling the Staebler-Wronski Effect in a-Si:H, Annu. Rev. Mater. Res. 31, pp. 47-79 (2001).

12. J.M. Pearce, Koval RJ, Collins RW, Wronski CR, Al-Jassim MM, Jones KM. Correlation of light-induced changes in a-Si:H films with characteristics of corresponding solar cells. In: Conference Record of the Twenty-Ninth IEEE Photovoltaic Specialists Conference, 2002. IEEE; 2002 p. 1098- 1101.

13. C.R. Wronski, Pearce, J.M., Koval, R.J., Niu, X., Ferlauto, A.S., Koh, J., Collins, R.W. Light Induced Defect Creation Kinetics in Thin Film Protocrystalline Silicon Materials and Their Solar Cells. Mat. Res. Soc. Proc. 715, p. A13.4 (2002).

14. J.M. Pearce, Deng J, Collins RW, Wronski CR. Light-induced defect states in hydrogenated amorphous silicon centered around 1.0 and 1.2 eV from the conduction band edge. Applied Physics Letters 2003;83(18):3725-3727.

15. J.M. Pearce, Deng J, Albert ML, Wronski CR, Collins RW. Room temperature annealing of fast state from 1 sun illumination in protocrystalline Si:H materials and solar cells. In: Conference Record of the Thirty-first IEEE Photovoltaic Specialists Conference, 2005. IEEE; 2005 p. 1536- 1539.

16. R.W. Collins, Ferlauto, A.S., Ferreira, G.M., Chen, C., Koh, J., Koval, R.J., Lee, Y., Pearce, J.M., and Wronski, C. R., Evolution of microstructure and phase in amorphous, protocrystalline, and microcrystalline silicon studied by real time spectroscopic ellipsometry. Solar Energy Materials and Solar Cells, 78(1-4), pp. 143-180 (2003).

17. S. Y. Myong, K. S. Lim, J. M. Pearce. Double amorphous silicon-carbide p-layer structures producing highly stabilized pin-type protocrystalline

silicon multilayer solar cells. App. Phys. Lett. 87(19), 193509 (2005); 87, 259901(2005).

18. J.M. Pearce, Podraza N, Collins RW, Al-Jassim MM, Jones KM, Deng J, Wronski CR. Optimization of open circuit voltage in amorphous silicon solar cells with mixed-phase (amorphous+nanocrystalline) p-type contacts of low nanocrystalline content. Journal of Applied Physics 2007;101(11):114301-114301-7.

19. H. W. Deckman, Wronski, C. R.; Witzke, H.; Yablonovitch, E.; , "Optically enhanced amorphous silicon solar cells," Applied Physics Letters , vol.42, no.11, pp.968-970, Jun 1983

20. F. Zhu, Jennings, P.J., Cornish, J.C.L., Hefter, G. and Lund, C.P. (1997) Optical enhancement of amorphous silicon solar cells. In: 35th Annual Conference of the Australian and New Zealand Solar Energy Society, December, Canberra.

21. M. I. Aslam and D. O. Guney, Surface plasmon driven scalable low-loss negative-index metamaterial in the visible spectrum, Phys. Rev. B 84, 195465 (2011).

22. D. O. Guney, Th. Koschny, and C. M. Soukoulis, Surface plasmon driven electric and magnetic resonators for metamaterials, Phys. Rev. B 83, 045107 (2011).

23. Aydin, V. E. Ferry, R. M. Briggs, and H. A. Atwater, Broadband polarization-independent resonant light absorption using ultrathin plasmonic super absorbers, Nature Communications 2, 517 (2011).

24. C. Garcia-Meca, R. Ortuno, F. J. Rodriguez-Fortuno, J. Marti, and A. Martinez, Double-negative polarization-independent fishnet metamaterial in the visible spectrum, Opt. Lett. 34, 1603 (2009).

25. R. Ortuno, C. Garcia-Meca, F. J. Rodriguez-Fortuno, J. Marti, and A. Martinez, Role of surface plasmon polaritons on optical transmission through double layer metallic hole arrays, Phys. Rev. B 79, 075425 (2009).

26. L. Lin, R. J. Reeves, and R. J. Blaikie, Surface-plasmon-enhanced light transmission through planar metallic films, Phys. Rev. B 74, 155407 (2006).

27. N. Papanikolaou, Optical properties of metallic nanoparticle arrays on a thin metallic film, Phys. Rev. B 75, 235426 (2007).

28. B. P. Rand, P. Peumans, and S. R. Forrest, Long-range absorption enhancement in organic tandem thin-film solar cells containing silver nanoclusters, J. Appl. Phys. 96, 7519 (2004).

29. D. M. Schaadt, B. Feng, and E. T. Yu, Enhanced semiconductor optical absorption via surface plasmon excitation in metal nanoparticles, Appl. Phys. Lett. 86, 063106 (2005).

30. D. Derkacs, S. H. Lim, P. Matheu, W. Mar, and E. T. Yu, Improved performance of amorphous silicon solar cells via scattering from surface plasmon polaritons in nearby metallic nanoparticles, Appl. Phys. Lett. 89, 093103 (2006).

31. E. Kintisch, Light-splitting trick squeezes more electricity out of Sun's rays, Science 317, 583 (2007).

32. S. Pillai, K. R. Catchpole, T. Trupke, and M. A. Green, Surface plasmon enhanced silicon solar cells, J. Appl. Phys. 101, 093105 (2007).

33. A. J. Morfa, K. L. Rowlen, T. H. Reilly III, M. J. Romero, and J. van de Lagemaat, Plasmon-enhanced solar energy conversion in organic bulk heterojunction photovoltaics, Appl. Phys. Lett. 92, 013504 (2008).

34. K.R. Catchpole and A, Polman, Design principles for particle plasmon enhanced solar cells, Appl. Phys. Lett.93, 191113 (2008).

35. C. Hägglund, M. Zäch, G. Petersson, and B. Kasemo, Electromagnetic coupling of light into a silicon solar cell by nanodisk plasmons, Appl. Phys. Lett.92, 053110 (2008).

36. C. Rockstuhl, S. Fahr, and F. Lederer, Absorption enhancement in solar cells by localized plasmon polaritons, J. Appl. Phys. 104, 123102 (2008).

37. P. Matheu, S. H. Lim, D. Derkacs, C. McPheeters, and E. T. Yu, Metal and dielectric nanoparticle scattering for improved optical absorption in photovoltaic devices, Appl. Phys. Lett. 93, 113108 (2008).

38. S. Fahr, C. Rockstuhl, and Falk Lederer, Engineering the randomness for enhanced absorption in solar cells, Appl. Phys. Lett. 92, 171114 (2008).

39. F. J. Beck, A. Polman, and K. R. Catchpole, Tunable light trapping for solar cells using localized surface plasmons, J. Appl. Phys. 105, 114310 (2009).

40. R. A. Pala, J. White, E. Barnard, J. Liu, M. L. Brongersma, Design of plasmonic thin-film solar cells with broadband absorption enhancements, Advanced Materials 21, 3504 (2009).

41. H. A. Atwatwer and A. Polman, Plasmonics for improved photovoltaic devices, Nature Material, 9, 205, 2010.

42. V. V. Varadan and J. Liming, Optical metastructures for trapping light in thin silicon solar cells, 2010 35th IEEE Photovoltaic Specialists Conference (PVSC), Honolulu, HI, June 2010.

43. L. Qiao, D. Wang, L. Zuo, Y. Ye, J. Qian, H. Chen, and S. He, Localized surface plasmon resonance enhanced organic solar cell with gold nanospheres, Applied Energy 88, 848 (2011).

44. T. Li, L. Dai, and C. Jiang, Design of efficient plasmonic thin-film solar cells based on mode splitting, J. Opt. Soc. Am. B, 28, 1793 (2011).

45. B. P. Rand, P. Peumans, and S. R. Forrest, Long-range absorption enhancement in organic tandem thin-film solar cells containing silver nanoclusters, J. Appl. Phys. 96, 7519 (2004).

46. D. M. Schaadt, B. Feng, and E. T. Yu, Enhanced semiconductor optical absorption via surface plasmon excitation in metal nanoparticles, Appl. Phys. Lett. 86, 063106 (2005).

47. D. Derkacs, S. H. Lim, P. Matheu, W. Mar, and E. T. Yu, Improved performance of amorphous silicon solar cells via scattering from surface plasmon polaritons in nearby metallic nanoparticles, Appl. Phys. Lett. 89, 093103 (2006).

48. J. Gwamuri, D. O. Guney, J. M. Pearce, John Wiley & Sons, Inc., Hoboken, NJ, USA.(2013).

49. Vora, Ankit, Jephias Gwamuri, Nezih Pala, Anand Kulkarni, Joshua M. Pearce, and Durdu Ö. Güney. Scientific reports4 (2014).

50. Vora, Ankit, Jephias Gwamuri, Joshua M. Pearce, Paul L. Bergstrom, and Durdu Ö. Güney. J. Applied Physics 9 116, 093103 (2014).

51. Karki Gautam, L.; Junda, M.M.; Haneef, H.F.; Collins, R.W.; Podraza, N.J. Spectroscopic Ellipsometry Studies of n-i-p Hydrogenated Amorphous Silicon Based Photovoltaic Devices. Materials 2016, 9, 128.

52. J. Gwamuri , R. Venkatesan , J. Mayandi, M. Sadatdol, D. Guney, J. M. Pearce. Ambient-dependent Agglomeration and Surface-Enhanced Raman Spectroscopy Response of Self-Assemble Silver Nano-particles for Plasmonic Photovoltaic Devices. Paper to be submitted

53. NREL http://rredc.nrel.gov/solar/spectra/am1.5/.

8. Conclusions and Recommendations/ Future Work

8.1. Overview

This study confirms the potential of plasmonic meta-perfect absorbers nanostructures to enhance absorption and efficiency of thin film PV devices. In this project, commercial grade thin film a-Si:H material is used with a hydrogen dilution of R = 10. This will ensure the cell reaches DSS within 100 hours with a high FF. Highly consistent data from optical characterization of the device layers was used to model the nanostructures. The optimized model shows absorption enhancement which is in agreement with published results from similar work. The synthesis process of the TCO and its subsequent optimization was carried out. Fabrication of metamaterial nanostructures and their integration to the final device was also performed. The synthesized device performance was then tested for both optical and electrical properties and test results will be used to guide future work.

8.2. Conclusions summary

Based on the studies undertaken in this project, the following conclusions are drawn:

8.2.1 Advances in Plasmonic Light Trapping in Thin-Film Solar Photovoltaic Devices:

- Theoretical work on the use of plasmonic nanostructures on PV devices has indicated that absorption enhancement of up to 100% is possible for thin-film PV devices using nanostructured metamaterials.

- As fabrication techniques evolve, it will be possible to fabricate less expensive and higher efficiency thin-film solar cells based on plasmonic quantum dots, optical nano-antenna and other novel technologies.

8.2.2 Limitations of ultra-thin transparent conducting oxides for integration into plasmonic-enhanced thin-film solar photovoltaic devices;

- Ultra-thin TCOs and in particular ITO present a number of challenges for use as thin top contacts on plasmonic-enhanced PV devices.

- Both ultra-thin TCO optical and electrical parameters differ greatly from those of thicker (bulk) films deposited under the same conditions.

- Ultra-thin TCOs are delicate due to their thickness, requiring very long annealing times to prevent film cracking.

- The reactive gases (usually oxygen or hydrogen) require careful monitoring

to avoid over-oxidizing or over-reducing the film as it impacts their stoichiometry.

- There is a trade-off between conductivity and transparency of the deposited films.

- The sub 50 nm thick TCO films investigated exhibited desirable optical properties (transmittance greater than 80 %), which makes them viable for plasmonic PV devices applications.

- All films evaluated using conventional fabrication techniques had resistivity values too high to be considered as materials for the top contact of conventional PV devices.

8.2.3 A new method of preparing highly conductive ultra-thin indium tin oxide for plasmonic-enhanced thin film solar photovoltaic devices:

- Cyclic wet chemical etching performed at room temperature was used to thin ITO films from 81 nm down to 36 nm.

- The films were characterized at the end of each cycle for electrical and optical properties.

- The sheet resistance of the thinnest film (36 nm) was observed to be on the same order as much thicker commercial ITO films currently utilized as transparent electrodes in PV and other opto-electronic devices.

- Optical properties of the shaved films were used in an optimized model to predict the optical enhancement of nano-disc plasmonic a-Si:H solar cells.

- Simulations indicate that optical enhancement greater than 21% are possible in the 300–730 nm wavelength range when compared to the reference cell.

- Using the novel chemical shaving method described here, high-quality ultra-thin ITO films capable of improving the efficiency of thin film a-Si:H solar cells have been demonstrated.

- The methods employed in the optimization process are well established and economically viable, which provide the technical potential for commercialization of plasmonic based solar cells.

8.2.4 Influence of Oxygen Concentration on the Performance of Ultra-Thin RF Magnetron Sputter Deposited Indium Tin Oxide Films as a Top Electrode for Photovoltaic Devices:

- Using this method, ultra-thin ITO films with record low resistivity values (as low as 5.83×10^{-4} $\Omega\cdot$cm) were obtained and the optical transmission is generally high in the 300–1000 nm wavelength region for all films.

- The etching rate strongly depends on the oxygen concentrations of RF sputtered ITO films as well as on the post process annealing.

- This processing has an effect on the oxygen vacancies densities even for the 0 sccm O_2 films.

- Surface roughness increased as the concentration of oxygen increased as expected. The etching reactions are simple redox reaction, hence the rates should increase with increases in O_2 concentration especially for non-stoichiometric films with distorted ITO matrix.

- The etch rate, preferred crystal lattice growth plane, d-spacing and lattice distortion were also observed to be highly dependent on the nature of growth environment for RF sputter deposited ITO films.

8.2.5 Ambient-dependent Agglomeration and Surface-Enhanced Raman Spectroscopy Response of Self-Assemble Silver Nano-particles for Plasmonic Photovoltaic Devices.

- In this study, AgNPs of different sizes and surface coverage were synthesized using ambient dependent agglomeration of e-beam evaporated silver thin-films (18.5 – 25 nm).

- The influence of different processing ambient conditions were observed on both NPs morphology and optical properties.

- Results here show conditions to obtain the greatest SERS intensity enhancement of up to 14 times is possible for 18.5 nm Ag films samples processed in argon ambient relative to vacuum processed films.

- A strong correlation is observed between processing conditions, particle sizes, shapes and their optical response (both UV-vis absorption and SERS).

- There is a clear observed relationship between particle size and resonance frequency indicated by the red-shifting of resonances with increasing particle size.

- XRD analysis reveal both the presents of polycrystalline bcc ITO and fcc

Ag. No Ag-Sn phases are observed in the results showing that there was no alloying between the Ag and Sn (from ITO) during the annealing process.

8.2.6 Plasmonic enhanced a-Si:H PV using Multi-disperse Self-Assemble Silver Nanoparticles.

- Solar cell samples were characterized for both optical and electrical performance prior to the addition of NPs.

- For the purpose of this study, AgNPs were successfully integrated on PV devises via a well-established method of agglomeration of Ag ultra-thin films under vacuum conditions.

- Both I – V and QE characterization were performed on the fabricated devices.

- Results indicate that the test devices are inferior to the reference device.

- NPs present a problem of shading on the test cells resulting in their decreased performance. This in is agreement with the prediction from the simulations.

8.3. Future work

There is need to lower the LCOE of solar PV power further until grid parity is achieved. So far, the focus has been on reducing solar panel costs. However, current trends show that about 62% of the total PV system costs are from cables, racking and installation labor (Trina Solar; Clean Technica 02/ 2014) and panels only constitute 20 % of the total costs.

This means that the only viable way towards the reduction of cost of solar PV electricity is through the use of more efficient solar panels. Highly efficient panels will mean large installation savings due to massive reductions in cables, racking and installation labor. Furthermore, high efficiency solar cells will result in saving on panel manufacturing and shipping costs.

This project have demonstrated that the plasmonics – based thin-film PV solar cell have to potential to achieve solar cell efficiencies necessary to further drive down the total cost of solar PV electricity. Additionally, these devices are capable of further reduction in the cost of solar panels through reduced device material layers thickness, easy of fabrication and abundance of the major material. However, to fully realize the potential of plasmonic enhancement based solar cells and achieve commercially viable devices,

further studies are recommended in the following areas:

8.3.1. Development and Optimization of future TCOs

Despite recent demonstration on novel methods to achieve highly conductive ultra-thin ITO (Gwamuri et al, 2016), further work is required to achieve alternative TCOs based on earth abundant materials such as zinc oxide (ZnO), aluminum-doped zinc oxide (AZO), fluorine-doped tin oxide (FTO) , as well as those based on novel materials such as carbon nanotubes and graphene. New devices architectures which employ a silver mesh on top of a 10 nm thick ITO have been recently proposed. To realize these devices, efforts should be put towards the fabrication of ultra-thin, smooth continuous, low loss TCOs films. This may require the use of alternative fabrication methods such as DC magnetron sputter and controlling the substrate temperature.

There is need to explore other growth techniques such as epitaxial growth processes using real-time in-situ monitoring to obtain information about optical and dielectric properties as well as growth mechanisms during the TCO film growth evolution. One common observed problem of ultra-thin film is delamination caused by stresses [Auciello and Krauss, 2001]. It is therefore critical to be able to measure and control stresses during the film growth process. This can be achieved using real-time curvature-based techniques for stress measurements such as; point deflection, laser reflectometry, height analysis, and lattice-bending [Floro & Chason, 2001]. Monitoring and controlling stresses is critical to achieving reliable and high performance thin TCOs since stresses are generally responsible for films failure through film cracking, surface roughening, mass transport or delamination [Floro & Chason, 2001; Auciello and Krauss, 2001]. All these are undesirable in plasmonics solar cell based TCOs film where continuous, uniform and stable TCOs are a prerequisite.

8.3.2. Optimization of Plasmonics Nanostructures

There is need to further explore methods for producing periodic metallic nanostructures for both top and back contact – based plasmonic solar cells. Self-assemble NPs presents a relatively economical means of obtaining both simple and complex nano-structures from thin metal films [Herminghaus et al, 1998; Atena & Khenner, 2009; Favazza et al, 2006; Trice et al, 2008;Guan et al, 2008; Boneberg et al, 2008] compared to traditional methods such as e-beam lithography. The challenge, however is obtaining NPs with desirable

sizes and surface coverage.

Future work must focus on in-situ real-time monitoring and analysis of NPs growth phenomena in vacuum and in the presence of ambient gases. Process conditions can be varied until the desired NP shape, size and surface coverage is observed and optimum process conditions noted. However, there is a requirement that the instrumentation be compact and easy to use to permit use as a dedicated tool for plasmonic NPs and TCOs processing. Real-time in-situ monitoring of Ag film agglomeration during annealing to obtain SANPs could be done using a scanning electron microscopy (SEM) both in vacuum and ambient gases. Substrate temperature and rotation speed could be varied until the NPs with required size range are achieved. Novel tools such as the ATC Multi- Technique or Hybrid systems from AJA Int. Inc do have these capabilities [AJA International INC]. Monitoring the initial film growth process can be done using either real-time spectroscopic ellipsometry (RTSE), reflection high-energy electron diffraction (RHEED), optical interference spectroscope, or a combination of these. Being able to deposit the TCO and Ag film, and then annealing to obtain NPs without breaking the vacuum will enable high efficiency and defect-free devices to be produced resulting in the ultimate realization of the "super- black cell", the plasmonics solar cell.

References

1. G. Parkinson, "PV Solar's Path To 2 Cents Per KWh" *Clean Technica*, Feb, 2014, Available from: http://cleantechnica.com/2014/02/01/pv-solars-path-2-cents-per-kwh/. Accessed on 5/30/2016.

2. J. Gwamuri, A. Vora, J. Mayandi, D. Ö. Güney, P. L. Bergstrom, and J. M. Pearce. "A new method of preparing highly conductive ultra-thin indium tin oxide for plasmonic-enhanced thin film solar photovoltaic devices." *Solar Energy Materials and Solar Cells,* 149 , 250-257, May 2016.

3. Herminghaus S, Jacobs K, Mecke K, Bischof J, Fery A, Ibn-Elhaj M and Schlagowski S Science 282, 916 919 (1998).

4. Atena A and Khenner M.Phys. Rev. B 80, 075402 (2009).

5. Favazza C, Kalyanaraman R and Sureshkumar R. Nanotechnology 17, 4229 4234 (2006).

6. Trice J, Favazza C, Thomas D, Garcia H, Kalyanaraman R and Sureshkumar R. Phys. Rev. Lett. 101, 017802 (2008).

7. Guan Y F, Pearce R C, Melechko A V, Hensley D K, Simpson M L and Rack P D,. Nanotechnology 19, 235604 (2008).

8. Boneberg J, Habenicht A, Benner D, Leiderer M, Trautvetter M, Pfahler C, Plettl A and Ziemann P. Appl. Phys. A 93, 415 419 (2008).

9. Auciello, O. and Krauss, A.R., 2001. In situ real-time characterization of thin films. John Wiley & Sons.

10. Floro, J.A. and Chason, E., 2001. Curvature based techniques for realtime stress measurements during thin film growth. In-Situ Characterization of Thin Film Growth Processes, p.191.

11. AJA International Inc. http://www.ajaint.com/multi-technique-systems.html. Accessed 31st June 2016.